SSRMP Annual Scientific Meeting 2010

Federal Office of Metrology METAS 11th and 12th November 2010

Proceedings

ISBN 3 908 125 52 9

Schweizerische Gesellschaft für Strahlenbiologie und Medizinische Physik
Société Suisse de Radiobiologie et de Physique Médicale
Società Svizzera di Radiobiologia e di Fisica Medica
Swiss Society of Radiobiology and Medical Physics

SGSMP
SSRPM
SSRFM

Preface

Dear colleagues and friends

The Annual Scientific Meeting 2010 of the Swiss Society of Radiobiology and Medical Physics took place at METAS in Wabern-Bern on the 11th and 12th of November 2010. It was a great pleasure to welcome so many colleagues and friends from Switzerland and abroad visiting our congress and the Industrial Exhibition.

The scientific program of the annual meeting was structured into six sessions with four invited speakers who addressed topics of fundamental dosimetry and the results of a survey of radiodiagnostic exposure of the Swiss population. The many oral and poster contributions of our community reflect the current high standards of research in our field, which is the basis of our daily clinical work guaranteeing a high standard of quality.

We want to thank all the people that contributed to the success of this meeting, in particular the Industrial exhibitors and Sponsors for their support and our colleagues for their scientific contributions.

On behalf of the local organizing committee

Damian Twerenbold

Table of Content

Water calorimetry as an absorbed dose to water primary standard

S. Vörös[1], B. Boillat[1], C. Meyer[1], A. Steiner[1], A. Tschudin[1], D. Twerenbold[1]
[1] Swiss Federal Office of Metrology (METAS)
mail: sandor.voros@metas.ch

Introduction

The Swiss Federal Office of Metrology (METAS) maintains primary standards for absorbed dose to water and provides calibration services for reference dosimetry systems used in the radiotherapy centres. For ^{60}Co γ radiation and high-energy photon beams between $TPR_{20,10}$ = 0.639 and $TPR_{20,10}$ = 0.802, this service is based since 2001 on a primary standard sealed water calorimeter. For high-energy electron beams between R_{50} = 1.75 g/cm^2 and R_{50} = 8.54 g/cm^2, a primary standard chemical dosimeter is used since 2002 [1][2][3][4]. A 22 MeV microtron accelerator with a conventional treatment head is used as radiation source for both the high-energy photon and electron beams.

In this contribution, the characteristics and challenges of water calorimetry are presented and compared to graphite calorimetry, which is another primary standard widely used in the metrology of ionizing radiation. Only a couple of important aspects of these different approaches will be presented here, but literature is available for an in-depth coverage of the topic ([5] and references therein). Various types of water calorimeters have been designed, in particular stirred water calorimeters [6] and sealed water calorimeters [7]. The METAS calorimeter is of the second type, and hence it is the one that will be discussed here.

Water calorimetry

Absorbed dose calorimetry is based on the assumption that energy imparted by ionizing radiation ultimately appears as a temperature rise. Water calorimetry in stagnant water is possible due to the very low thermal diffusivity of water which ensures that the temperature distribution remains for a sufficiently long time in place, thus enabling accurate measurements at a point. Absorbed dose to water is given by

$$D_w = c_w \cdot \Delta T_w \cdot \frac{1}{1-k_{HD}} \cdot \prod k \qquad (1)$$

(units: Gy = J/kg), where c_w (J/kg/K) is the specific heat capacity of water (≈ 4204.8 J/kg/K at 4°C), ΔT_w (K) the measured temperature rise (typically 100-500 μK in 1 minute), k_{HD} and $\prod k$ are correction factors that will be discussed now.

The heat defect

In general, full conversion of energy deposition into temperature rise is not fulfilled, and the term describing this non thermal energy deposition is the heat defect

$$k_{HD} = \frac{E_a - E_h}{E_a}$$

where E_a is the total absorbed energy and E_h the energy appearing as heat. Heat defect appears as a result of different kind of chemical reactions in water (so-called radiolysis), which can be endothermic ($k_{HD} > 0$) or exothermic ($k_{HD} < 0$).

The purity of the water used as absorber medium is crucial, since organic impurities can influence the value of k_{HD} in some uncontrolled way. Some gas dissolved in the water can have an influence as well. By saturating the water with some specific gases like H_2, N_2, Ar or even some H_2-O_2 mixture, a well-

defined value can be imparted to the heat defect. For example, it has been calculated that for H_2, N_2 or Ar the heat defect should be very small, and hence $k_{HD} = 0$ with a standard uncertainty of 0.3% [8].

The other correction factors

The last correction term $\prod k$ in equation (1) is a product of several correction factors accounting for different effects:

$$\prod k = k_c \cdot k_v \cdot k_p \cdot k_{dd} \cdot k_\rho \cdot k_t \tag{2}$$

The conductive heat transfer correction k_c accounts for the presence of non-water materials around the measurement point, such as the thermistor itself and the glass vessel (see below), as well as non-uniformity of the absorbed dose distribution. Those materials have a heat capacity lower than and radiation absorption characteristics different from water. This factor is obtained by performing a numerical calculation of heat transfer, solving the heat transport equation

$$\rho \cdot c \cdot \frac{\partial T}{\partial t} = \nabla \cdot \left(\tilde{k} \cdot \nabla T\right) + \rho \cdot \frac{dD}{dt} \tag{3}$$

using a finite element method, for which an accurate simulation of the calorimeter geometry is required. Here ρ is the mass density and c the specific heat capacity of the medium, T is the temperature, t is the time, $\tilde{k}$ is the thermal conductivity and dD/dt is the apparent local absorbed dose rate. The calculation yields $k_c = 0.998$ with a standard uncertainty of 0.15%.

The convective heat flow k_v should be negligible if the calorimeter is operated at 4°C, where the water has its maximum density (see below), and hence $k_v = 1$.

The absorption and scattering of radiation due to the presence of non-water materials around the measurement point (in particular the glass vessel) is accounted for by the perturbation correction factor k_p. It can be measured by irradiating a small dosimeter (e.g. a diode) located at the reference measurement depth in a water phantom, alternatively with and without the glass vessel around it. Its value is $k_c = 1.003$ with a standard uncertainty of 0.05%.

The lateral dose profile at the reference depth in the phantom may not be perfectly flat, and hence a factor k_{dd} is needed that corrects the measured dose to the dose at the reference point. The beam profile can be measured by performing a scan over the transverse plane with a diode for example. Then, the measured signal is integrated over a small surface around the reference point (on the beam axis) as well as over a surface corresponding to the thermistor's effective location, and the ratio of those values typically yields $k_{dd} \approx 0.997\text{-}1.003$.

The calorimeter is operated at 4°C (see below), but the transfer standards (ionization chambers) are calibrated at 20°C, which implies the use of a density correction factor k_ρ to account for the difference in density of the water. This correction becomes negligibly small if the reference depth for the measurement point in the water phantom is expressed in g/cm^2, and hence varies with water density when expressed in cm.

Finally, a correction for the transient thermistor response k_t corrects for the increased thermistor response at the beginning or just after the end of an irradiation. It has been hypothesized that this might be due to electron-hole pairs created in the thermistor [5]. This effect becomes negligible if the first 20 seconds of the post-irradiation drift curve is ignored for the analysis of the data [8], hence $k_t = 1$.

Typical uncertainties on the determination of absorbed dose to water with a water calorimeter are of the order of 0.40% - 0.43%, but smaller uncertainties (0.20%) involving a large number of automated measurements performed on a ^{60}Co source have also been reported by PTB [9].

The design of the METAS sealed water calorimeter

The heart of the water calorimeter consists of two very sensitive negative temperature coefficient (NTC) thermistor beads enclosed in thin glass tubes located on the symmetry axis of a cylindrical glass vessel (see Figure 1). This vessel must be cleaned very carefully and filled with high-purity water before being gassed in order to saturate the water and get a well-known heat defect value, as mentioned above.

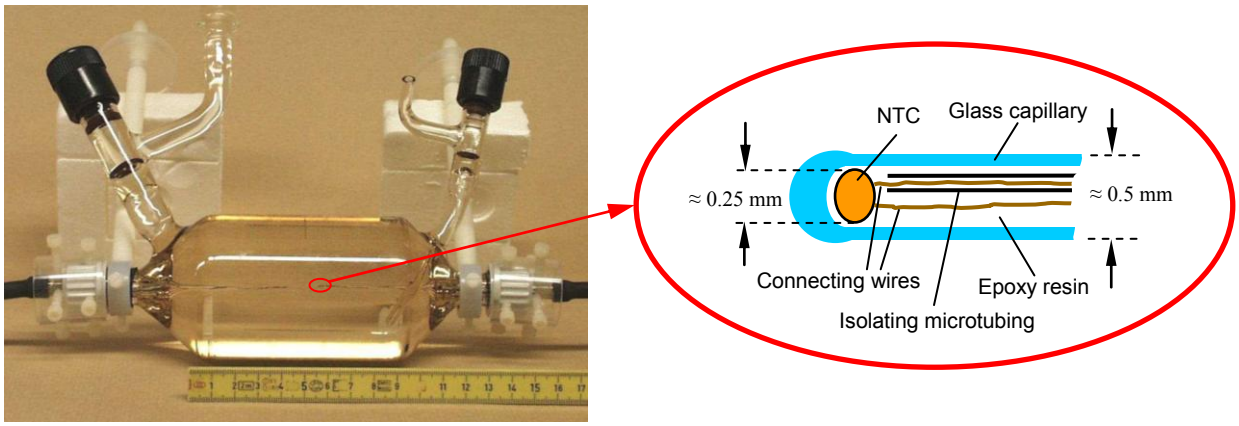

Figure 1 The METAS glass vessel which constitutes the heart of the water calorimeter system. A drawing of the tip of one thermistor mounted inside the vessel is shown on the right-hand side.

The vessel is then positioned inside a 30 x 30 x 30 cm^3 PMMA phantom filled with deionised water and isolated with 5 cm expanded polystyrene. The phantom itself is enclosed in a larger wooden box isolated with another 5 cm expanded polystyrene, and the temperature of the air layer between the phantom and the box is actively regulated in such a way that the water temperature inside the phantom remains in the interval 4°C ± 0.02°C (see Figure 2). The operating temperature of the calorimeter corresponds to the temperature of highest density of water, in order to minimize convection effects during irradiation. Indeed, in a limited interval around the maximum, the dependence of water density on temperature is very small (the tangent to the $\rho(T)$ graph is horizontal at that point).

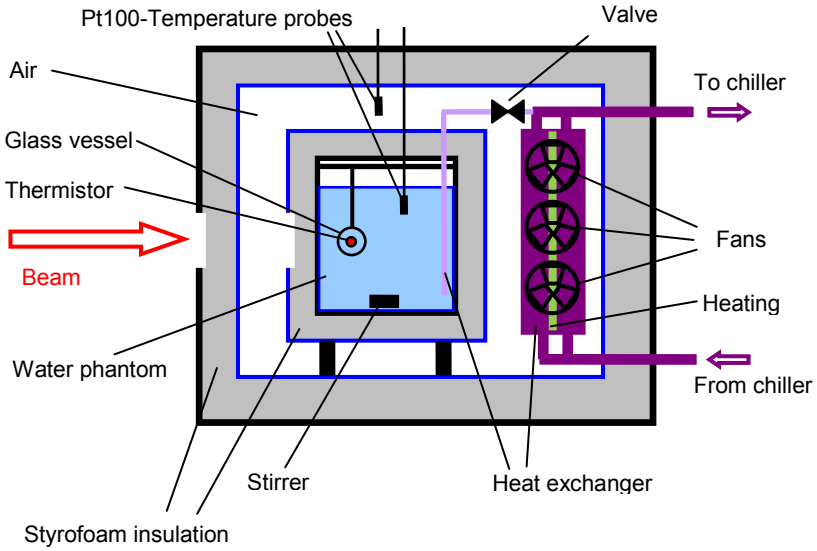

Figure 2 Drawing of the METAS sealed water calorimeter.

The (temperature dependent) electrical resistance of each thermistor is measured using an AC bridge, assuming the following relationship between temperature and resistance:

$$R(T) = R_0 \cdot e^{\beta \cdot \left(\frac{1}{T} - \frac{1}{T_0}\right)} \tag{4}$$

where R_0 is the resistance at temperature T_0 and β may be taken constant within a small temperature interval. At 4°C, the resistance of a thermistor is typically between 9 kΩ and 10 kΩ. The value of β must be determined for each thermistor by calibrating them beforehand over a much larger temperature span as the one used in the calorimeter.

The thermistor is connected to one arm of the AC Wheatstone bridge, and a variable resistance decade in another arm serves to equilibrate the bridge (see Figure 3). A lock-in amplifier continuously measures the voltage in the centre of the bridge, and the thermistor's resistance change can be inferred from this measured voltage variation. For that purpose, the bridge sensitivity must first be determined, using calibrated electrical resistors that can be switched in the bridge arm where the thermistor is connected during so-called "OhmCal" measurements.

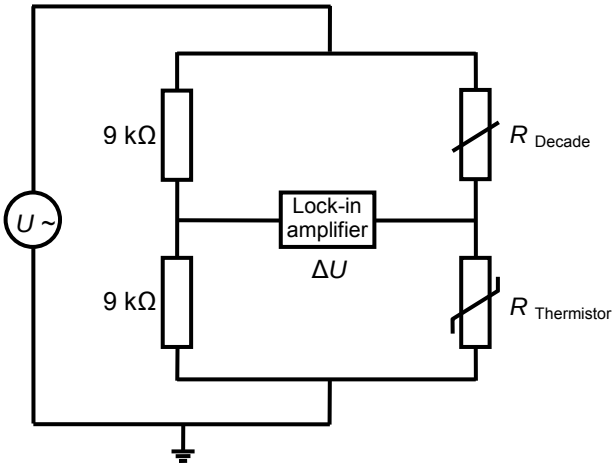

Figure 3 Simplified drawing of the Wheatstone bridge used for measurement of the thermistor's resistance value.

Calibration of working standards

The calibration coefficient $N_{w,Q}$ of an ionization chamber is determined as follows: the ionizing current is measured for the ionization chamber placed with its reference point at the same depth as the thermistors. For the beam quality Q the calibration coefficient is:

$$N_{w,Q} = \frac{D_w}{M_Q} \cdot \frac{M_Q^{mM}}{M_Q^{mD}} \tag{5}$$

where D_w/M_Q^{mD} is the (fully corrected) absorbed dose to water determined by the calorimeter measurement, divided by the reading of a monitor chamber taken during the same calorimeter irradiation period, and M_Q/M_Q^{mM} is the (fully corrected for air density, incomplete saturation, beam profile and high voltage polarity) reading of the ionization chamber, divided by the reading of the same monitor chamber taken during the chamber irradiation period.

The monitor chamber readings are needed to correct for the accelerator beam fluctuations, which might result in different dose rates during calorimeter and ionization chamber measurements. For a beam produced by a radioactive ^{60}Co source, no monitor chamber is used, but the radioactive decay of the source must be taken into account to correct for the elapsed time between the calorimeter and ionization chamber irradiations.

At METAS, transfer standards of type NE 2571 readout by commercially available electrometers of type Keithley 6517 are calibrated directly against the water calorimeter. They are used for the calibration of the reference dosimetry systems used in the radiotherapy centres, since direct calibration of each dosimeter in the calorimeter would imply too much time and effort.

Results for the ^{60}Co γ radiation

The most recent water calorimeter measurement campaign at METAS took place in the Spring of 2009. The METAS ^{60}Co source of type Alcyon II was used for that purpose.

Figure 4 shows a typical OhmCal (bridge response calibration) measurement, where a resistance jump of known amplitude is applied in the same bridge arm as the one where the thermistor is connected. This measurement lasts for 210 s, recording the bridge voltage during 70 s before applying the resistance change, 70 s after the jump in resistance occurred, and 70 s after returning to the original resistance configuration. Figure 5 displays a typical calorimeter measurement, which lasts for 360 s. During the first 120 s, the bridge voltage is recorded without irradiation, the next 120 s are during ^{60}Co irradiation, and the last 120 s are after the end of the irradiation.

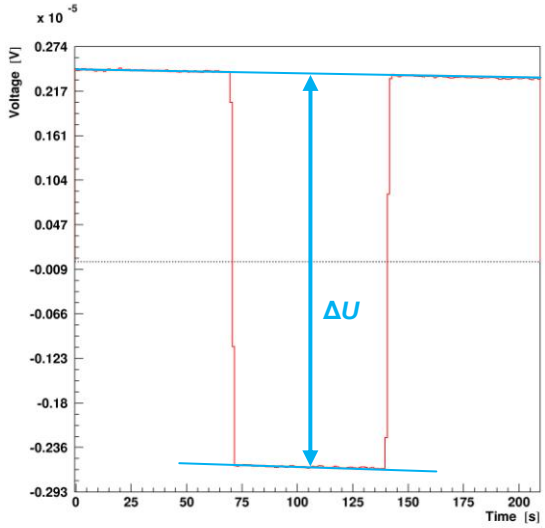

Figure 4 „OhmCal“ measurement. This is the voltage step seen by the lock-in amplifier as a known resistance jump of 0.2 Ω is imparted to the arm of the bridge containing the thermistor.

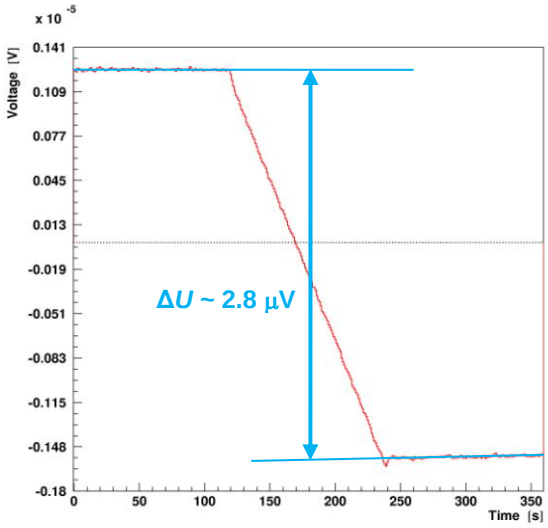

Figure 5 Irradiation measurement. This is the voltage slope seen by the lock-in amplifier as the calorimeter is irradiated for two minutes by the ^{60}Co source. A very rough estimate of the absorbed dose yields $\Delta U \sim 2.8\ \mu V \rightarrow \Delta R \sim 0.12\ \Omega$ (from “OhmCal” measurement) $\rightarrow \Delta T \sim 0.3$ mK (from thermistor calibration) $\rightarrow D \sim 1.3$ Gy (using the heat capacity of water).

Data analysis starts with fitting the flat parts of the measured signal and extrapolating the fits to mid-irradiation time in order to determine the voltage change.

The results for a couple of hundred such measurements taken in 2009 are shown in Figure 6. The quantity shown here is the dose rate of the ^{60}Co source on 1. January 2010 at 00:00:00.

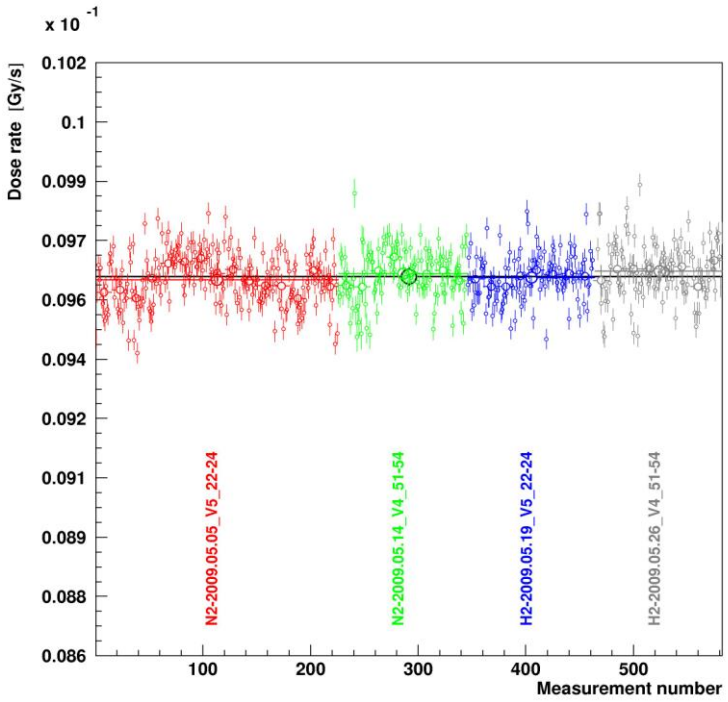

Figure 6 Final result of about five hundred eighty irradiation measurements of the calorimeter performed at the ^{60}Co source. The quantity shown here is the dose rate of the METAS Alcyon II ^{60}Co source on 1. January 2010 at 00:00:00. Two different glass vessels (serial numbers 4 and 5), each with different thermistor pairs (serial numbers 22-24 and 51-54 respectively) were used, each being saturated with two different gases, once using N_2 and once using H_2.

The mean value is 0.00963 ± 0.00004 Gy/s. The value obtained in the previous calorimeter measurement performed in January 2006 was 0.00964 ± 0.00004 Gy/s, which shows a very good agreement.

Graphite calorimetry

Graphite calorimetry is, together with water calorimetry, the most widely used primary standard method for absorbed dose to water. The absorbing medium, graphite, differs from water in three ways: its specific heat capacity is about six times smaller, its thermal diffusivity is nearly six hundred times larger and it is a solid rather than a liquid, and as such it does not have any radiation-induced chemistry to contribute to a heat defect [5].

The smaller specific heat capacity gives graphite calorimetry a six-fold advantage over water calorimetry in signal to noise ratio, i.e., the measured temperature rise in the absorber medium is six times higher for a given amount of absorbed energy. Furthermore, due to the high thermal diffusivity, the effectively measured absorbed dose is an average over the entire volume of the absorbing graphite core rather than a local measurement.

On the other hand, water calorimetry is a far more direct way of realizing the unit absorbed dose to water than graphite calorimetry, which realizes absorbed dose to graphite. In the latter case, a number of additional conversion measurements and calculation steps are needed, which worsens its overall uncertainty budget. Nevertheless, there is a great metrological interest in comparing the results of both water and graphite calorimetry, since they are quite independent methods.

Typical construction of a graphite calorimeter

While each graphite calorimeter has its own specific construction, the general design and the main parts are usually similar. As an example, the design of the BIPM graphite calorimeter [10] will be outlined here. It is one of the most recently designed graphite calorimeter, and it was constructed such to make it transportable.

The calorimeter consists principally of a graphite core enclosed by a graphite jacket, placed behind a graphite window. The thickness of this window is such that the requirement for a total mass thickness of 5 g/cm^2 or 10 g/cm^2, for ^{60}Co or high energy photon beams respectively, is fulfilled. To minimize heat losses, a vacuum container made of PMMA houses the calorimeter (see Figure 7). Three reflecting surfaces surround the jacket to reduce radiative heat transfer (not shown in the figure).

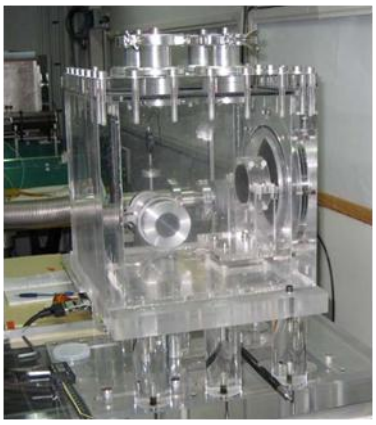

Figure 7 PMMA phantom of the BIPM calorimeter. The small graphite cylinder on the right is the jacket and the larger disc is the entrance window. Image courtesy BIPM [10].

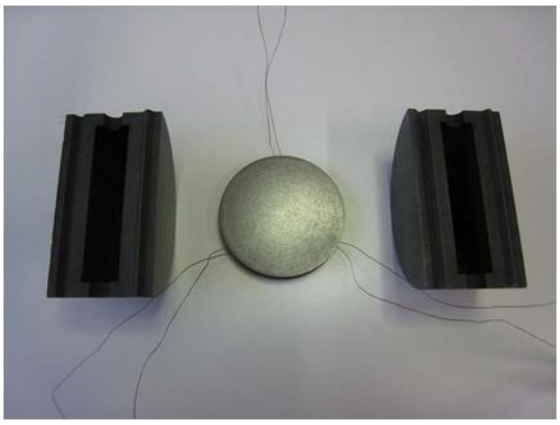

Figure 8 The graphite core with the thermistor wires, surrounded by the two halves of the graphite jacket hosting the core. Image courtesy BIPM [10].

Figure 8 shows the design of the graphite core and jacket, with the wires of the three thermistor pairs positioned on the curved face of the core. The core is a solid cylinder 6.7 mm long and 45 mm in diameter, whose mass and specific heat capacity must be precisely determined before the calorimeter is assembled. Four holes are drilled in the curved surfaces to accept the pins that support the core inside the jacket.

Each of the thermistor pair is mounted in a Wheatstone bridge powered by a DC power supply. Before being mounted inside the calorimeter, the core must be temperature calibrated with respect to a platinum resistance thermometer in a temperature-stabilized water tank.

The jacket forms a hollow cylinder, to house either the graphite core or the parallel-plate transfer ionization chamber. The BIPM jacket features top and bottom half-cylinders instead of the more traditional front and back components in order to get a more homogeneous temperature distribution, with no barrier to heat conduction from front to back. One thermistor pair is glued into holes drilled on the curved surface of each half-cylinder, in the same way as for the core.

The correction factors

The presence of several gaps in the calorimeter (e.g. between the graphite window and the jacket, between the jacket and the core, etc.) leads to a decrease in dose to the core [11]. This effect is accounted for by applying a gap correction derived from Monte Carlo calculation.

Convective heat transfer is essentially eliminated by evacuating the calorimeter. Conductive heat transfer obeys the heat transport equation (3) and is usually solved using a finite element method, for

which an accurate simulation of the calorimeter geometry is required, as in the case of the water calorimeter. Contributions from thermistor self-heating may be included in the calculation. Thermistor wires and core supporting pins should be as fine as possible in order not to contribute significantly to the conductive heat transfer. Finally, radiative heat transfer can be minimized by the use of reflecting surfaces located around the jacket.

Further correction factors are required for the differences in depth between the measuring and the reference depth, for the non-uniformity of the dose distribution over the core and for measurement bridge related electrical corrections.

The dose conversion

In photon beams two methods are usually used to convert absorbed dose measured in graphite to absorbed dose in water. The first method is based on the relation between collision kerma in graphite and water, usually derived using Monte Carlo methods (see [5] for further details). The conversion factor is slightly energy-dependent, but its value is typically around 14-15% [12].

The second approach, used by the BIPM, makes use of an ionization chamber as a transfer instrument to derive dose to water from dose to graphite. For that purpose, the chamber is calibrated in the graphite phantom of the calorimeter and then used for dose measurements in water using the equation [13]

$$D_w = D_g \cdot \frac{M_w}{M_g} \cdot \left(\frac{D_w}{D_g}\right)^{MC} \cdot \left(\frac{M_g}{M_w}\right)^{MC} \tag{6}$$

where D_w and D_g are the dose in water and graphite, respectively, and M_w and M_g represent the corrected ion chamber reading in water and graphite, respectively. The *MC* tag denotes values obtained in the Monte Carlo simulation of the corresponding experimental setup. Altogether, three different measurement arrangements must be realized at BIPM for a full absorbed dose to water determination:

1) The calorimeter is used in vacuum with the jacket containing the core. The absorbed dose rate to graphite, D_g, is both measured and calculated. The measured value is determined essentially using an equivalent relation to (1) with the correction factors specific to the graphite calorimeter discussed above.
2) The graphite core is replaced by the transfer ionization chamber and the assembly is at atmospheric pressure. The ionization current in graphite, M_g, is measured and a corresponding cavity dose rate calculated.
3) The same ionization chamber is placed inside an identical phantom filled with water. The ionization current, M_w, is measured and the corresponding cavity dose rate calculated.

Typical uncertainties assigned to the dose transfer procedures in high-energy photon beams lie between 0.19% and 0.35%, and the overall uncertainty on the determination of absorbed dose to water is typically between 0.41% and 0.46% [5].

Discussion and outlook

The design of the METAS sealed water calorimeter has been outlined, and as a comparison, the principle of the graphite calorimeter has been presented as well. The sealed water calorimeter, which is used by METAS, has the big advantage of being the most direct method to realize the absorbed dose to water unit “Gray”, thus avoiding the need for additional conversion steps. On the other hand, the graphite calorimeter benefits from a much lower heat capacity. As a result, it features a much more favorable signal to noise ratio, thus reducing the need for long measurement series.

Similar uncertainties (around 0.40% - 0.45%) for the determination of absorbed dose to water are typically achievable with both calorimeter types, but it appears that water calorimetry may have a

greater improvement potential. Comparing the results of both water and graphite calorimetry is very interesting from a metrological point of view, since they are quite independent methods. Together with other independent primary methods like chemical (Fricke) dosimetry or ionization chamber-based standards, they build a robust system for the realization of absorbed dose to water.

As the national metrology institute of Switzerland, METAS also contributes to the international effort for a reliable reference dosimetry system. In this context, METAS took part in the EURAMET project No. 1021, which is a direct comparison of primary standards of absorbed dose to water in ^{60}Co and high energy photon beams [14][15]. For the purpose of this comparison, the graphite calorimeter of the BEV travelled to METAS and was irradiated at the ^{60}Co source as well as at the M22 microtron accelerator. The final report for this project has not been published as yet (November 2010), but will be made available on the EURAMET website in due time. In the future, METAS plans to participate in the BIPM BIPM.RI(I)-K6 comparison [13], for which the BIPM graphite calorimeter will be transported to METAS as well.

References

[1] M. Sassowsky, H. Quintel, R. Schafer and G. Stucki, Primärdosimetrie hoch energetischer Photonenstrahlung, metINFO Vol. 11 No. 2 (2004), 4-9

[2] G. Stucki, W. Münch and H. Quintel, The METAS absorbed dose to water calibration service for high energy photon and electron beam radiotherapy, Published in "Standards and Codes of Practice in Medical Radiation Dosimetry" (Proc. Int. Symp. Vienna, 2002), IAEA Vienna (2003), Vol. I, IAEA-CN-96-8, 103-113

[3] W. Münch, G. Stucki, R. Moning and B. Vaucher, Eichung von Referenzdosimetersystemen für die Strahlentherapie in der Schweiz, Z. Med. Phys. 11 (2003), 269-278

[4] S. Vörös and G. Stucki, Simulation Monte Carlo pour la réalisation d'un étalon primaire de la dose absorbée dans l'eau pour des faisceaux d'électrons, Radioprotection 42 (2007), 565-575

[5] J. Seuntjens and S. Duane, Photon absorbed dose standards, Metrologia 46 (2009), S39-S58

[6] C. K. Ross, N. V. Klassen and G. D. Smith, The effects of various dissolved gases on the heat defect of water, Med. Phys. 11 (1984), 653-658

[7] S. R. Domen, A sealed water calorimeter for measuring absorbed dose, J. Res. Natl Inst. Stand. Technol. 99 (1994), 121-141

[8] C. K. Ross, J. P. Seuntjens, N. V. Klassen and K. R. Shortt, The NRC sealed Water Calorimeter: Correction Factors and Performance, Proc. of NPL Workshop on Recent Advances in Calorimetric Absorbed Dose Standards, ed. A. J. Williams and K. E. Rosser, Teddington, UK, (2000), 90-102

[9] A. Krauss, The PTB water calorimeter for absolute determination of absorbed dose to water in ^{60}Co radiation, Metrologia 43 (2006), 259-272

[10] S. Picard, D. T. Burns and P. Roger, Construction of an Absorbed-Dose Graphite Calorimeter, Rapport BIPM-2009/01 (2009), 1-12

[11] M. Boutillon, Gap correction for the calorimetric measurement of absorbed dose in graphite with a ^{60}Co beam, Phys. Med. Biol. 34 (1989), 1809-1821

[12] International Commission on Radiation Units and Measurements, Radiation dosimetry: x-rays and gamma rays with maximum energies between 0.6MeV and 50MeV, Rep. 14 (1969), (Washington, DC: ICRU)

[13] S. Picard et al., Comparison of the standards for absorbed dose to water of the NRC and the BIPM for accelerator photon beams, Metrologia 47 (2010) Tech. Suppl. 06025

[14] A. Steurer, A. Baumgartner, R.-P. Kapsch, G. Stucki and F.-J. Maringer, Results of the direct comparison of primary standards for absorbed dose to water in 60Co and high-energy photon beams (EURAMET TC-IR Project 1021), IDOS, Vienna, 9-12 November 2010 E2-CN-182. paper no. 253

[15] http://www.euramet.org/index.php?id=tc-ir-projects → 1021

Radiation Safety Aspects for the SwissFEL Project at Paul Scherrer Institute

W. Roser[1], A. Fuchs[2], R. Lüscher[2]
[1]Bereich Grossforschungsanlagen, Paul Scherrer Institut, 5232 Villigen PSI
[2]Abteilung Strahlenschutz und Sicherheit, Paul Scherrer Institut, 5232 Villigen PSI
mail: werner.roser@psi.ch

Introduction

The Paul Scherrer Institut (PSI) is the largest research center for natural and engineering sciences within Switzerland. It is part of the ETH domain and offers a variety of research opportunities. PSI's three main subject areas are the investigation of the structure of matter, energy and the environment, and the human health.

The research strategy of PSI requires every 10-20 years a so-called "future project". The next future project will be a Free Electron Laser (FEL). The main part of such a facility is a new accelerator for 6 GeV electrons, which is scheduled for commissioning in 2016.

In the following chapters, a short presentation of the facility, which will be called SwissFEL, and its purpose will be given and the radiation safety aspects of such a system will be discussed.

Principle and Layout

Figure 1 shows a principal layout of the SwissFEL facility. Its purpose is to provide a source of extremely bright and short X-ray pulses enabling scientific discoveries in a wide range of disciplines, from fundamental research to applied science [1].

The whole installation will be about 700 m long. Its basic principle is displayed on the bottom of figure 1, from the left to the right: stimulated by a Laser system, short electron pulses of 200 pC will be emitted by a metallic cathode of an electron gun. The electron bunches will then be accelerated by three linear accelerators to their nominal energy of about 6 GeV. The linac repetition rate will be 100 Hz, leading to an average beam current of 40 nA (taking 2 microbunches per Linac pulse into account)[1]. In a series of magnetic undulators the electrons will be forced to slaloms, resulting in the emission of extremely intense and narrow X-ray pulses (10 GW peak X-ray power with a pulse duration shorter than 20 fs; 1 fs = 10^{-15}s). Afterwards the electrons will be dumped and the X-rays can be lead to dedicated experimental stations.

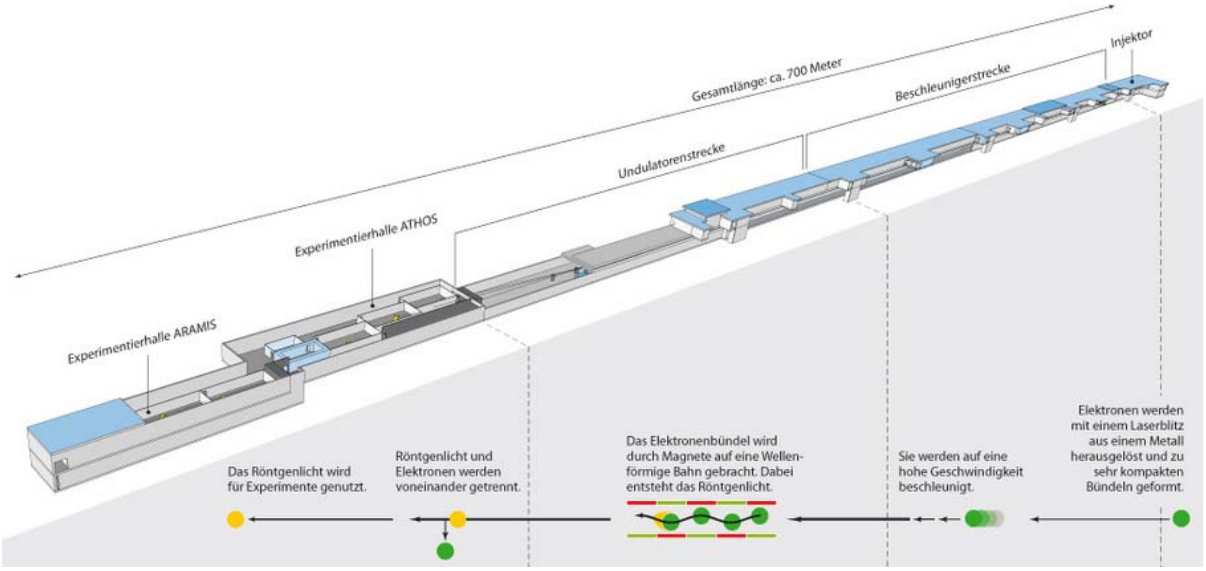

Figure 1: Layout and principle of the Swiss Free Electron Laser (SwissFEL).

[1] The resulting beam power of ca. 240 W is of the same order than the mean beam power of a conventional clinical linear accelerator.

Purpose of SwissFEL

The wave length of the X-ray pulses produced by SwissFEL will be in the range of 1 – 70 Å and therefore of the same order than the size of light molecules like water or proteins. Scientists expect a huge demand for research with coherent X-ray light sources (i.e., X-ray lasers), which function according to the FEL principle.

Using these X-rays interdisciplinary teams from biology, chemistry, physics, material sciences and other disciplines are gaining insights into both the interior structure of materials and the physical processes taking place. The filming of biomolecules at the fs time scale will be possible. Furthermore, the light intensity of SwissFEL will be ca. 10^{10} times higher than that of the SLS, the Swiss Light Source at PSI.

With SwissFEL it will be possible to obtain detailed information on various processes that are not accessible using currently available methods.

The potential relationship of SwissFEL with Medical Physics could be future applications of Bioimaging at nm resolution (figure 2).

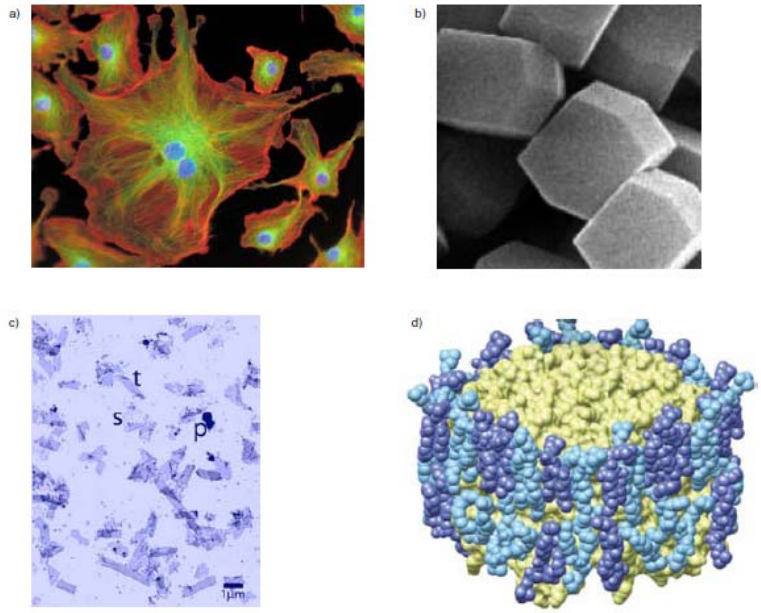

Figure 2: Bioimaging at nm resolution. Picture taken from the PSI-SwissFEL Science Case [1].

Worldwide, there are currently only three facilities with a similar purpose running (LCLS, U.S.A.) or under construction (Spring-8, Japan and DESY, Germany).

Location of SwissFEL

Due to its length, it is not possible to place SwissFEL on one of PSI's areas. Therefore several locations close to PSI have been investigated and evaluated. In 2009, this process ended by the selection of a location in the forest close to the PSI east area (figure 3).

Most of the buildings will be covered by soil. According to current plans only one side of the surface buildings will be visible. Two passages for wild animals over the installation will help reducing the impact of the facility on the wildlife. The existing forest road will be used to access SwissFEL from the PSI east area.

Currently the processes necessary to obtain the building license are ongoing; in this context several questions regarding conventional and especially radiation safety have to be dealt with.

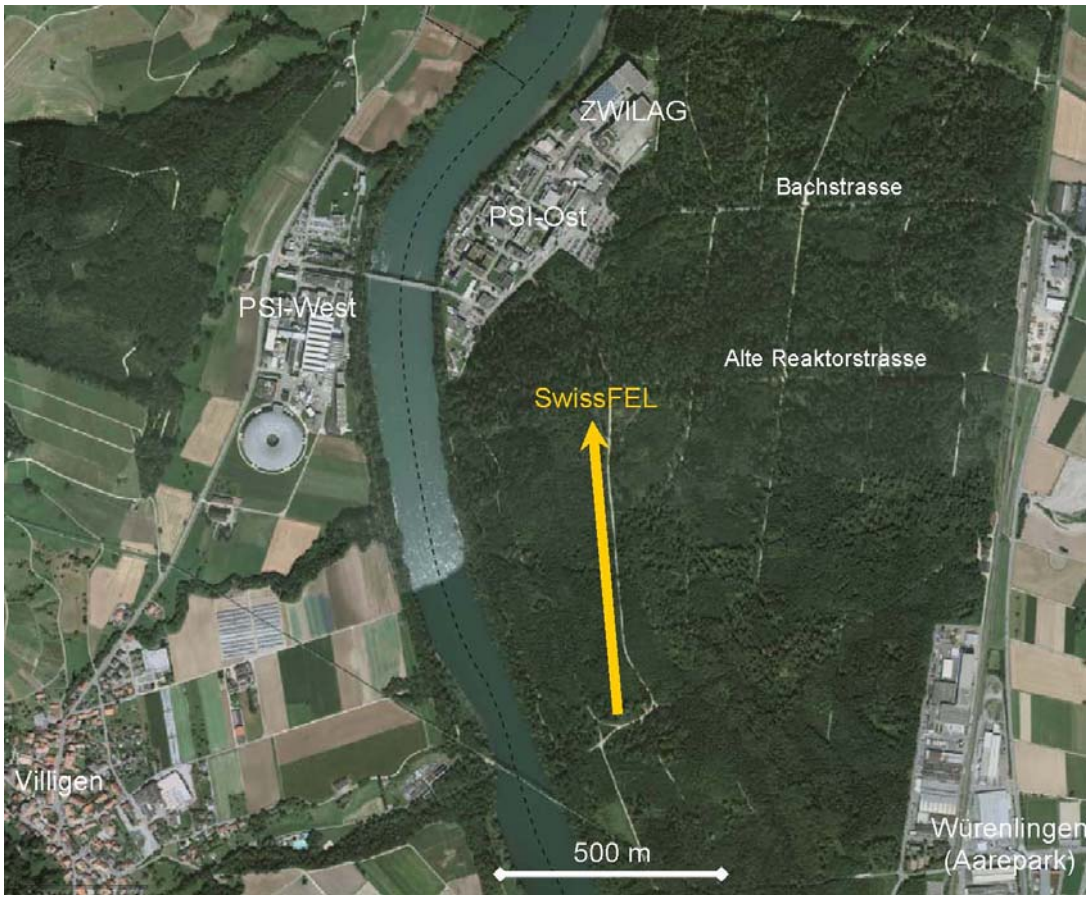

Figure 3: Position of SwissFEL according to the current building application. It will be located in the forest close to the PSI east area.

Figure 4: Model of the exterior view of the SwissFEL buildings. Most of it will be covered by soil.

Radiological Benchmarks for SwissFEL

The operation of the SwissFEL facility is subject to Swiss legislation, in particular to the radiation protection law and ordinance. Additional local guidelines by the Swiss Federal Office of Public Health (BAG), and the Swiss Federal Nuclear Safety Inspectorate (ENSI) have also to be taken into account.

Since SwissFEL will be located outside the fenced PSI area, dose and dose rate limits for the public have to be adhered to at the outside of its buildings (ambient equivalent dose: 0.1 mSv/w or 0.6 µSv/h; effective dose: 0.1 mSv/a).

Beam loss points of SwissFEL

For the purpose of planning the required radiation shielding, it is essential to have some knowledge about the predicted beam losses. According to the design of its accelerators, SwissFEL will have several defined beam loss points (figure 5). These are mainly those locations, where the electron beam will be magnetically deflected (bunch compressors, switch yard), collimated, or dumped.

Calculations of the required shielding in these critical areas have been started based on local beam loss assumptions using analytical codes (Shield11, iShield11) and will be refined using Monte Carlo methods (MCNPX, FLUKA).

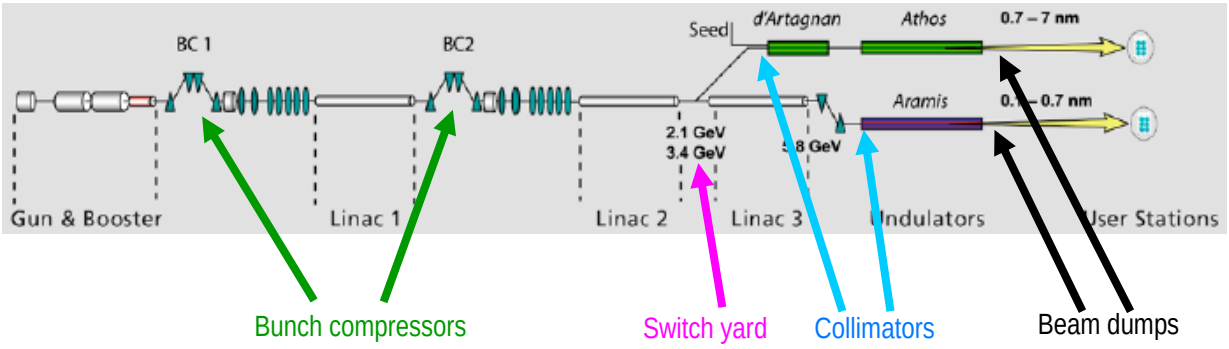

Figure 5: Layout of the SwissFEL beam lines with indication of the beam loss points. More details concerning the beam line can be found in reference [2].

Undefined beam loss

In addition to the defined beam loss mentioned above, the so-called “dark current” will lead to further beam losses, which will not be restricted to certain beam loss points. Dark current will be emitted by the electron gun and radio frequency structures along the whole beam line. The reason are the strong electrical fields required for the acceleration of electrons, which lead to a parasitic emission of electrons at various places.

Dark current is not in phase with desired beam and stopped at certain positions (e.g., at magnetic bending structures), therefore it comprises at broad spectrum of electrons. However, its energy is reduced compared with the primary electron beam.

Assumptions related to the shielding of dark current are difficult and must be verified later by dose rate measurements. Additional local shielding might then be necessary in order to fulfil the ALARA principle.

Shielding design

In Figure 6, the current shielding design based on shielding calculations is displayed. The soil coverage, which will be of the order of 1 m and form part of the shielding, is not shown.

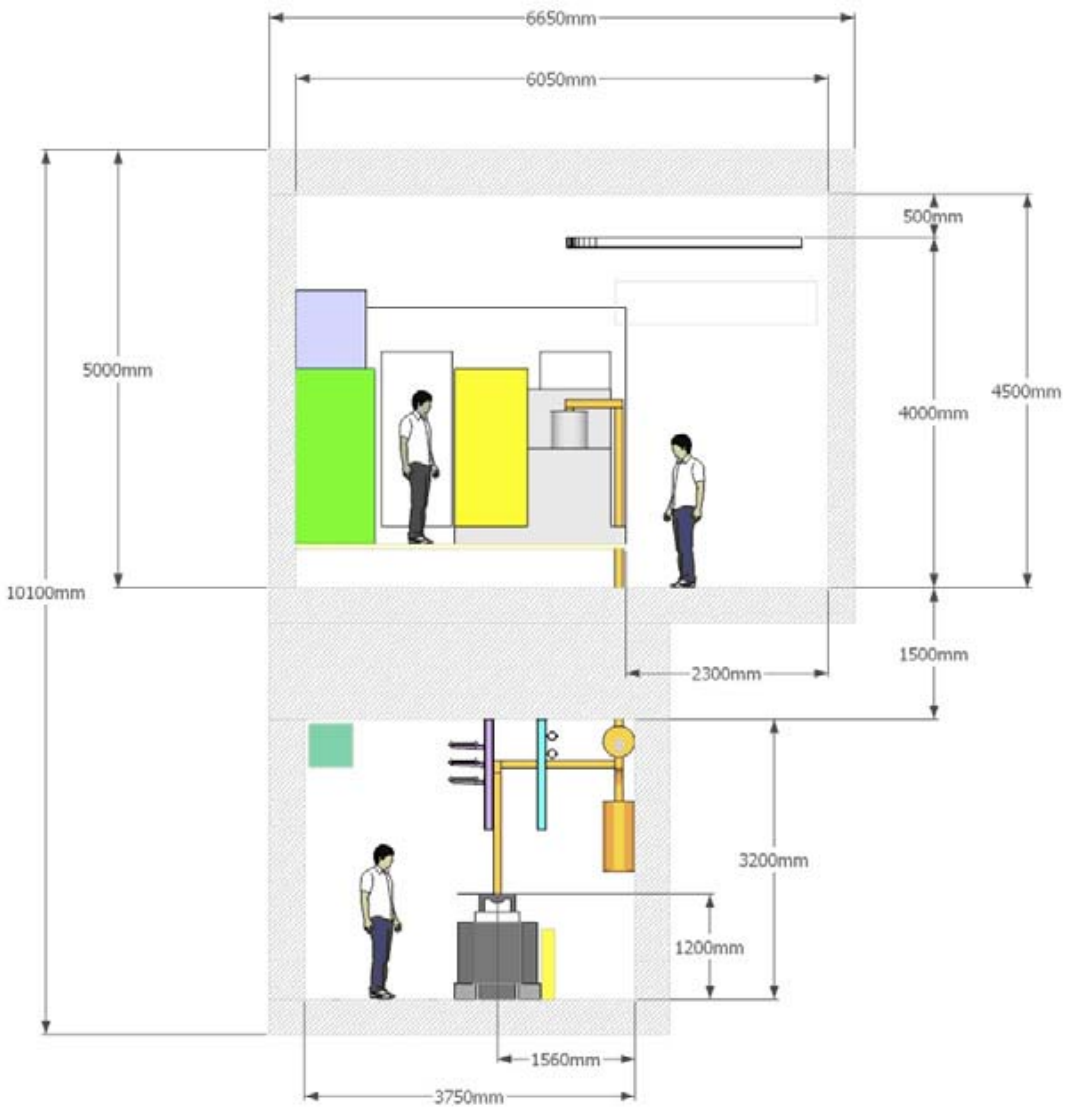

Figure 6: Current shielding design. The tunnel walls consist of 0.5 m of concrete, the thickness of the tunnel roof is 1.5 m; not shown is the soil coverage with variable shape and depth.

Further aspects of shielding calculations

For a project like SwissFEL, where only a very limited base of reference installations is available, there is a need of conservative assumptions for radiation shielding, since later reinforcement can be complicated and expensive. On the other hand, too much conservatism is also very expensive: 0.5 m of additional shielding around the beam tunnel requires about 5'000 m^3 of additional concrete with associated costs of approximately 3 MFr.

Special attention require the emergency exits along the beam tunnel and various cable and radio frequency feedthroughs, which weaken the shielding and may require the construction of suitable mazes. If possible, these structures should not be placed close to regions with higher beam losses.

The expected doses rates also depend on the estimated work load (≈ 5000 h/a) and the Linac repetition rate (up to 100 Hz).

Other aspects related to radiation safety

Beam tunnel and at least some of the experimental areas (depending on their future use) need to be defined as controlled zones and working areas and constructed as such.

Safety systems are required in order to prevent the access to the beam tunnel during presence of electron beam or to lock the experimental areas when X-rays are present. So-called personnel safety systems and local access control systems will be designed for this purpose.

In order to detect excessive beam losses within and around the facility, a beam loss and radiation surveillance system will be available.

Radioactive activation

Since the accelerated electrons have fulfilled their "job" after travelling in slaloms through the undulator areas and producing coherent X-rays therein, they will be simply stopped in dedicated beam dumps. Here, the highest radioactive activation is expected. However, activation and resulting dose rates will be moderate, as far as safety requirements during deconstruction are concerned.

On the other hand, (γ,n) reactions from bremsstrahlung, secondary neutrons, and other particles will lead to a level of air activation in the accelerator tunnel, which could require monitoring of the air exhaust. Here, further calculations based on the planned design of the ventilation system are necessary.

The activation of the cooling circuits and of the soil will be small, so that no corresponding measures have to be taken.

Shutdown of SwissFEL

It may sound strange at the moment, but the future shutdown and disassembly of SwissFEL, which might take place around the year 2040, has also to be discussed right now.

The experience with PSI's large research facilities shows that the buildings and part of the infrastructure will be reused in other projects and experiments. Only few components need disposal and a minority of it will have to be declared as radioactive waste. Here, an estimation of disposal costs will be necessary.

From the present point of view, the shutdown of SwissFEL will not lead to serious problems.

Conclusions

The SwissFEL project is on track. From the radiological point of view no serious problems are to be expected. PSI's expertise with its currently running three proton and three electron accelerators and the Swiss Light Source SLS facilitates the development and the validation of the necessary radiation safety measures for the new electron accelerator to be built for SwissFEL.

References

[1] Ultrafast Phenomena at the Nanoscale: Science opportunities at the SwissFEL X-ray Laser. PSI Report No. 09-10, edited by Bruce D. Patterson, September 2009. Available on www.swissfel.ch.

[2] SwissFEL Conceptual Design Report, edited by R. Ganter, July 2010. Available on www.swissfel.ch.

How do the X-ray unit settings influence patient dose in interventional radiology?

E.T. Samara[1], J-C. Stauffer[2], F.R. Verdun[1]
[1] Institute of Radiation Physics, University Hospital Centre and University of Lausanne, Lausanne, Switzerland
[2] Department of Cardiology, University Hospital Centre and University of Lausanne, Lausanne, Switzerland
mail: eleni-theano.samara@chuv.ch

Introduction

As the number of interventional procedures increases, more effort should be given to patient radiation protection. Although the technology of X-ray units has improved with the introduction of the flat-panel detectors (FPD) and their ability for dose reduction, there is no bibliographic evidence that FPDs really reduce radiation dose. The aim of our study was to examine the differences between installations with FPDs.

Material and Methods

Three radiological units (A, B1 and B2), all equipped with FPD were characterised with respect to entrance dose rate. Machines B1 and B2 were constructed by the same company. For policy reasons, the manufacturer names are not given. Four PMMA phantoms with different thicknesses (5 - 20 cm, with a step of 5 cm) were employed. Dose rate was measured by Radcal dosimeter connected to an 11 cm^3 ion chamber (Monrovia, USA). Source-to-skin distance and source-to-detector distance were set at 75 cm and 100 cm, respectively. The field size was 16 cm for unit A and 15 cm for units B1 and B2 at the level of the detector. Dose rate was measured for fluoroscopy mode (15 and 30 images/sec) and cine acquisition (15 images/sec). Additional measurements were performed for paediatric protocols, if available. Image quality was evaluated by the manufacturers and was acceptable for diagnostic purposes.

Results

Only a low-dose protocol was set up for unit A. For units B1 and B2, the medium-dose protocol was available. Additionally, for unit B2, which belonged to a university hospital, the high-dose protocol was also in place. As expected, the entrance dose rate depends on the phantom thickness (Figure 1). Differences of up to 12% were estimated for units B1 and B2. Entrance dose rate was found to differ four to five times between units of different manufacturers (Figure 2). Dose rate for "paediatric" mode was found slightly lower than that of "adult" for low and medium dose protocol (Figure 3). However, the high dose protocol for paediatric patients delivers a higher dose to the patient than that for adults.

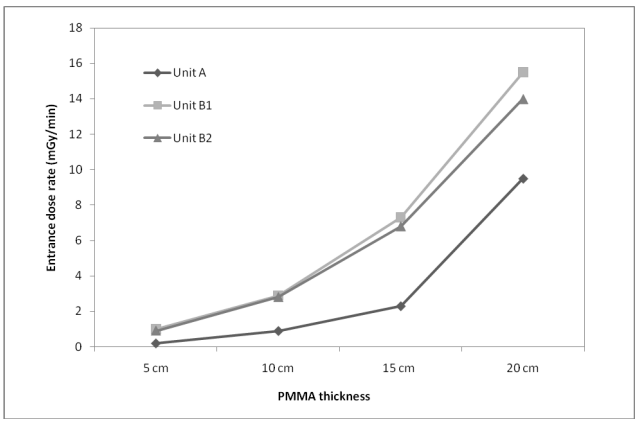

Figure 1: Entrance dose rate for four phantom thicknesses with low-dose protocols (fluoroscopy: 15 i/sec)

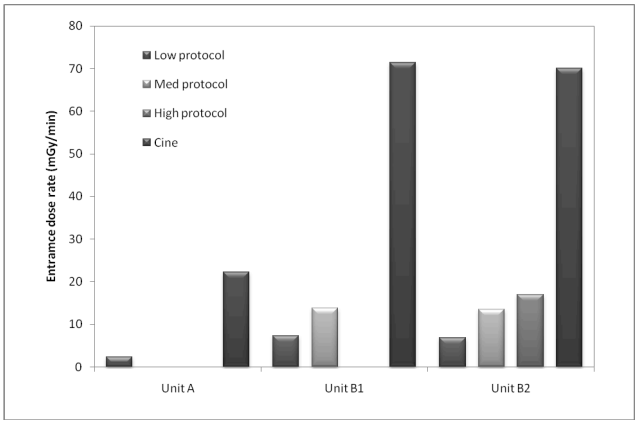

Figure 2: Comparison of entrance dose rate for dose protocols used (fluoroscopy: 15 i/sec, cine: 15 i/sec, phantom thickness: 15 cm PMMA)

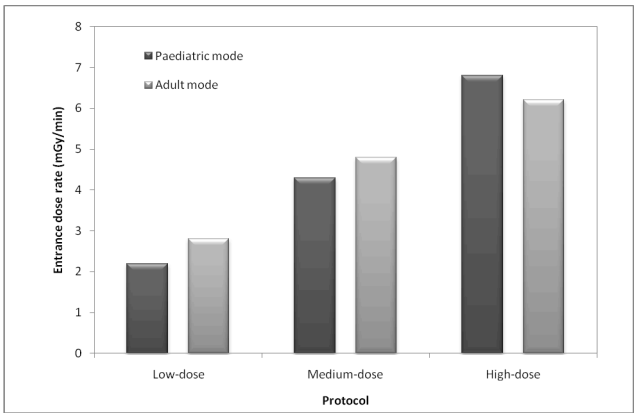

Figure 3: Comparison of entrance dose rate for three dose protocols used for paediatric and adult patients for unit B2 (fluoroscopy: 15 i/sec, phantom thickness: 10 cm PMMA)

Discussion

It is important to characterize the X-ray unit in terms of radiation dose as well as image quality. Differences between entrance dose rates may be attributed to different dose settings on image quality. Varying levels of image quality and dose are acceptable, as they allow physicians to better perform the procedures. However, wide differences for the same operation mode should be eliminated. Close collaboration between physicians, medical physicists and companies is required when setting up dose protocols. The first step for patient dose reduction is setting the low-dose protocol as default. Moreover, the use of cine acquisition should be done only when necessary. Further optimization is required for the "paediatric" mode as children are more radiation sensitive than adults. Medical physicists will play a critical role in patient and personnel radiation protection in the field of diagnostic radiology.

References

[1] Chida K.; Inaba Y.; Saito H.; Ishibashi T.; Takahashi S.; Kohzuki M.; Zuguchi M.: Radiation dose of interventional radiology system using a flat-panel detector. AJR Am J Roentgenol. 2009; 193(6):1680-1685.

[2] Trianni A.; Bernardi G.; Padovani R.: Are new technologies always reducing patient doses in cardiac procedures? Radiat Prot Dosimetry. 2005; 117(1-3):97-101.

[3] Vano E.; Sanchez R.; Fernandez JM.; Rosales F.; Garcia MA.; Sotil J.; Hernandez J.; Carrera F.; Ciudad J.; Soler MM.; Ballester T.: Importance of dose settings in the x-ray systems used for interventional radiology: a national survey. Cardiovasc Intervent Radiol. 2009; 32(1):121-126.

An advanced and efficient analysis tool for Linac QA

P. Favre-Bulle[1,2], C. Chatelain-Favre-Bulle[1,2], D. Vetterli[1,2]
[1]Radio-Onkologiezentrum Biel
[2]Abteilung für Medizinische Strahlenphysik, Inselspital Bern
Email: pascal.favre@radioonkologie.ch

Introduction

We report on 5 months of experience with the modular QUALimagiQ (QualiFormeD SARL, France) v4.1.3 software platform managing and analysing images acquired by electronic kV and MV portal imagers, for the purpose of Linac quality assurance (QA).
During this period, we acquired data once per week in order to quantify the amplitude and frequency of variability of the various parameters under test. We also used this opportunity to demonstrate that the acquisition of electronic images with existing equipment (kV and MV imagers) together with software-based analysis tools is very efficient in reducing the overall QA time and thus gives more time to the medical physicist to concentrate on the results of the analysis.

Material and Methods

In our centre in Biel, 4 different software modules are in use for the QA of the MLC, the MV imager (PV), the kV imager (OBI) and the determination and comparison of the light, the irradiated and prescribed field sizes.
The phantoms needed are the LAS VEGAS for the PV QA and the LEEDS TOR18FG for the OBI QA, plus a few dedicated centring tools available from QualiFormeD. For the measurement of the spatial resolution of the PV by means of the modulation transfer function, as it is done for the OBI, one can replace the LAS VEGAS by the EPID QC phantom from PTW (Physikalisch-Technische Werkstätten Dr. Pychlau GmbH).
For an efficient image acquisition in clinical mode we prepared dedicated prescriptions in ARIA's RT Chart (Varian Medical Systems) making the process fast and easy. The full set of data - including all MLC, imagers and collimated fields QA - is then taken within 2 hours. The DICOM images acquired (69 per Linac) are exported and then automatically sorted by QUALimagiQ using keywords from the DICOM header related to the tests programmed in the clinical prescriptions. The analysis is then carried out either in an automated way, in less than 15 sec for each of the 4 modules, or step by step when it is necessary to find out where and why a particular parameter was out of tolerance.

The java-based platform is both robust and flexible. Various types of DICOM images can be imported in the database without caring about the beam energy, date of acquisition, machine, etc. The images are automatically sorted and the acquisition parameters tested for consistency with the associated test before the analysis (Figure 1).

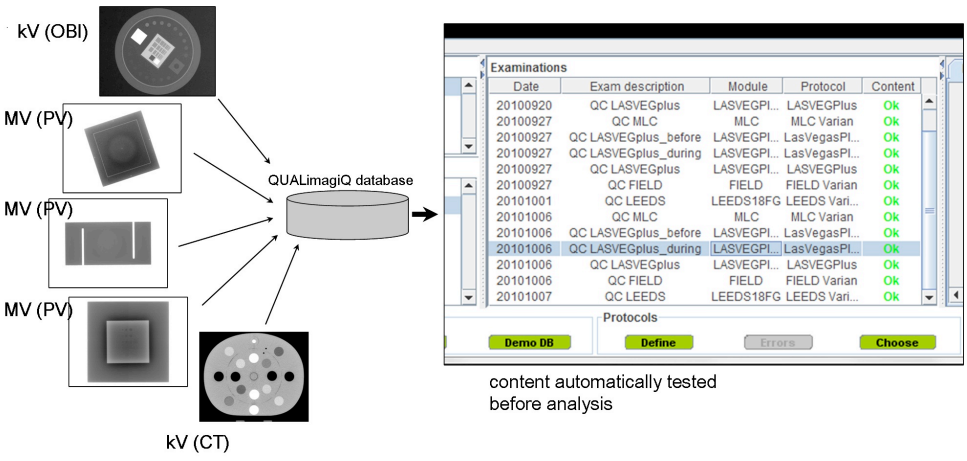

Figure 1. Data import in the QUALimagiQ database

QUALimagiQ is insensitive to phantom alignment, each analysis starts by an automatic detection of the phantom position. In addition, each parameter of the analysis can be adjusted by the user, this capability is appreciated but is also time consuming to configure.

After the analysis, all test results are validated by the user, they are stored in a database and a pdf report is automatically generated. For each parameter tested, a temporal evolution curve is produced together with the assigned tolerance levels. Since there is a vast amount of information (e.g. Figure 2), such plots and alert windows are valuable tools to select the more relevant parameters to be followed.

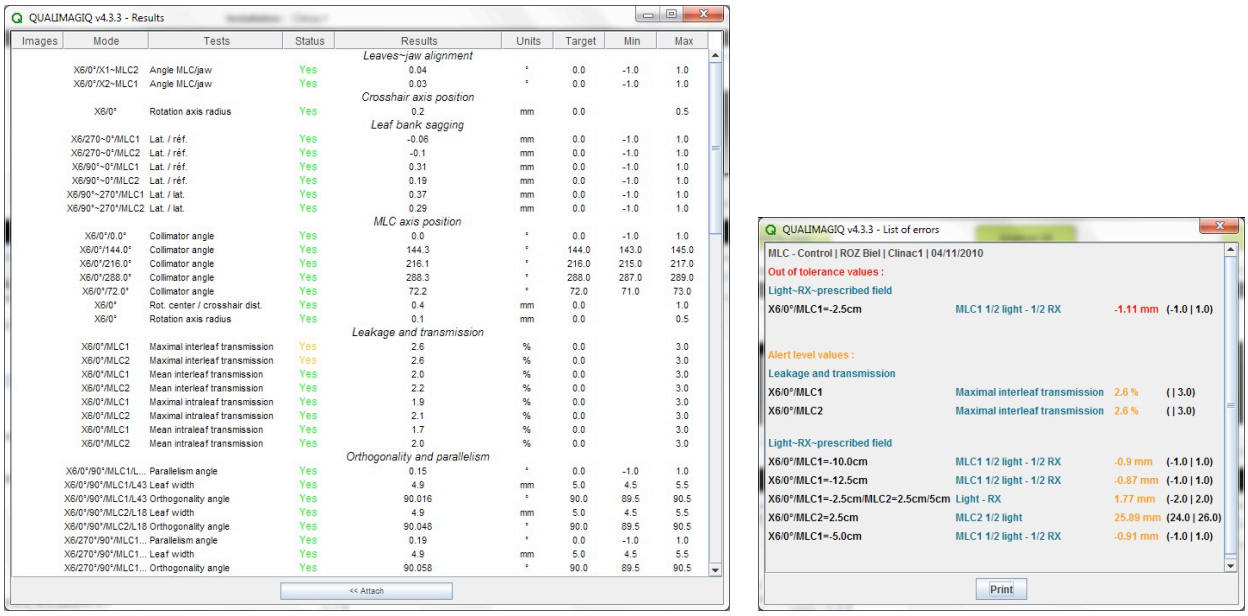

Figure 2. Analysis output window for the MLC module (left) and corresponding alert window (right)

Due to time/length constraints, we focus on the most interesting tests of the MLC and OBI QA modules.

Results: MLC QA module

MV images of static test patterns are analysed and mechanical as well as dosimetric quality controls are performed. They include testing a) leaf positions, b) collimator rotation axis, c) intra-/inter-leaf transmissions, d) sagging of leaf banks with gantry rotation, e) orthogonality/parallelism of the leaves.
Note: the RX field size in QUALimagiQ was calibrated by comparison to the RX field size measured in water in reference conditions.

a) Leaf positions

The test is made on 5 images representing 5 different field sizes defined by the MLC, i.e. with 5, 10, 15, 20 and 25 cm opening (see Figure 3 for 15 cm opening). The analysis displays for each leaf the deviations to the expected position on top of the image itself. Note that the tests were realized with a Millennium 120 MLC (Varian Medical Systems) composed of 10 mm wide leaves on the outer parts and 5 mm wide leaves in the inner part.

In order to determine the precision with which the leaf positions were found by the software, we produced a field with 10 misplaced leaves, from 2 mm down to 0.05 mm. We used the smallest field size of 5 cm as we noticed an increase of the leaf deviations with smaller field sizes. The measured positions were correct down to 0.1 mm which confirmed the sub-mm precision of the setup.
From the results described above, it is possible to study the evolution of the deviations of a particular leaf with time. In Figure 4, we show the evolution of the deviations for leaf 30 on banks 1 and 2 for the past 5 months. Three field openings are presented in each plot: 5 cm, 15 cm and 25 cm. On bank 1 we see that the deviations are larger for the 5 cm fields (squares) than for the 25 cm fields (dots).

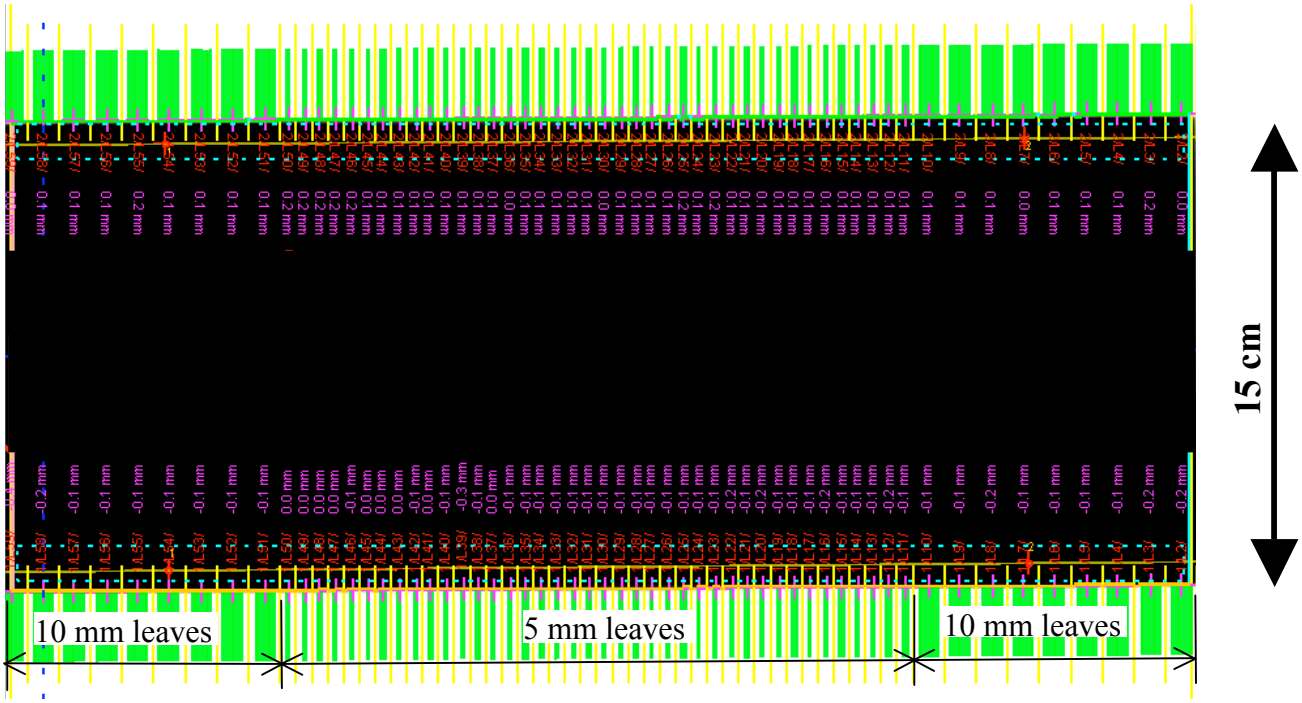

Figure 3. Image of a field of 15 cm opening defined by the MLC only. The results of the analysis are superimposed. Each leaf is labelled and the deviation to its expected position is given (in violet)

Leaf 30 on bank 1 has thus a systematic deviation of about 0.2 mm towards the centre i.e. the field would be too small if all the leaves follow this trend, especially for small field sizes. On bank 2 leaf 30 shows a different behaviour resulting in a field slightly too large, especially at large field sizes.
This test complies with recommendation 11, points 5.2 (tolerance 1mm) and 2.5.

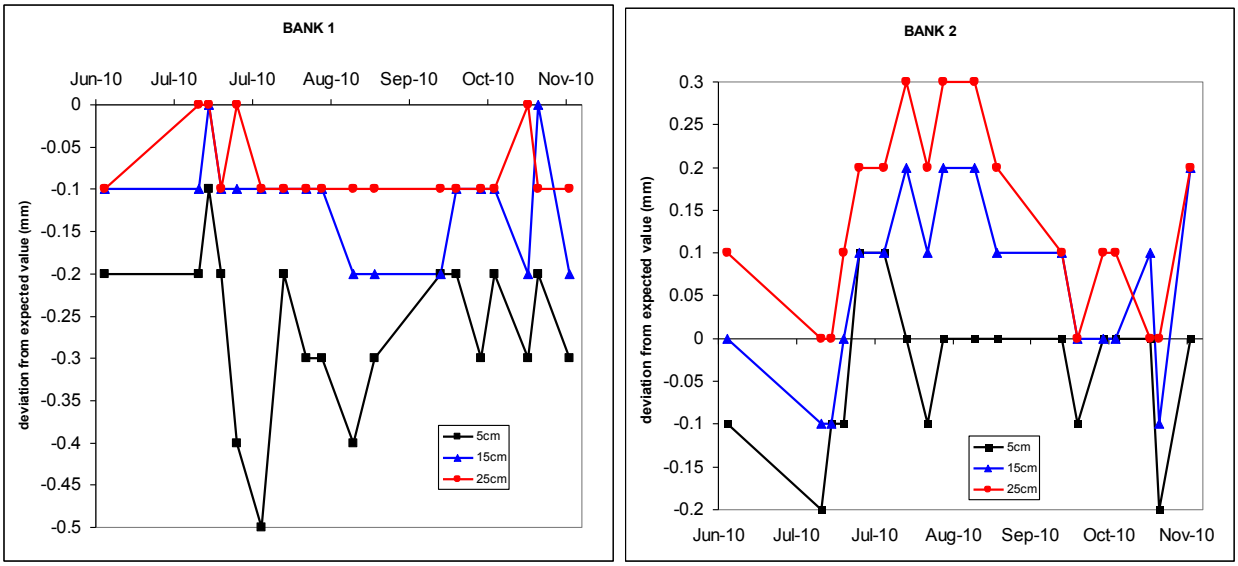

Figure 4. Deviations from the expected position for leaf 30 for bank 1 (left) and bank 2 (right). Evolution with time using various field openings

b) Collimator rotation axis

We test here the coincidence of the collimator rotation axis with

1. the crosshair
2. the centre of radiation of the MLC
3. the centre of radiation of the jaws

For each of these tests, a set of 5 images is required, one every 72° of collimator angle (Figure 5).

To determine the crosshair axis, a test object with a metallic ball in its centre (red circle in Figure 5) is imaged at the 5 different angles, whereby the ball is aligned anew for each angle on the crosshair. The images are superimposed (Figure 6) and the ball positions on the detector are determined by the software.

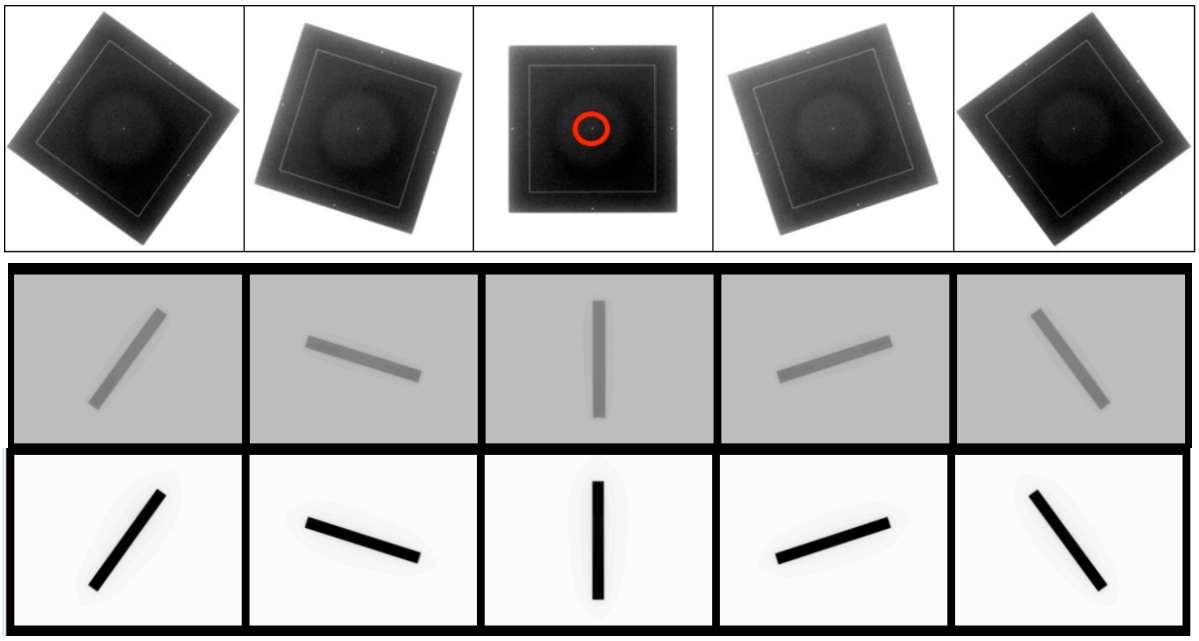

Figure 5. Five images taken every 72° of collimator rotation. Top panel: test-object aligned on crosshair, middle panel: MLC field, bottom panel: jaw field

The circle in the right panel of Figure 6 is the smallest circle including all the ball positions on the detector. Its centre represents the position of the collimator rotation axis and its radius the uncertainty to this position. This test complies with recommendation 11, point 2.6.1 (tolerance 2mm).

For the determination of the centre of radiation of the MLC, 5 rectangular MLC fields are taken at the various collimator angles. The superimposed image is shown in Figure 7, the smallest circle including all the intersections of the yellow lines - representing the MLC field centres - is drawn in blue. Its centre defines the position of the MLC radiation axis on the imager. The crosshair circle found in the previous test is added in violet in the figure to compare the relative positions of the two centres. Finally, the software calculates the distance between the two centres; it is 0.3 mm in this example.
Figure 8 (left panel) shows the evolution with time of the distance between crosshair and MLC axis, and the 2 circles radii. The distance parameter was very stable (0.4±0.1mm) over the period of observation. The crosshair circle radius has a higher uncertainty than the MLC circle radius due to the human factor in aligning the test object on the PV.

For the centre of radiation of the jaws, a similar procedure as for the MLC is used. The 5 rectangular fields (Figure 5, lower panel) are realized this time only with the jaws. As for the MLC, the software allows us to compare the position of the centre of radiation of the jaws on the PV with the axis of the crosshair. Figure 8 (right panel) shows the evolution with time of the distance between crosshair and jaw axis (very stable also: 0.3±0.1mm), and the 2 circles radii.
It is interesting to compare the two panels of Figure 8, i.e. MLC axis versus crosshair axis with jaw axis versus crosshair axis. While the accuracy in the determination of the MLC axis (the circle radius) is of the same order of magnitude (0.2±0.1mm) as for the crosshair, the accuracy in the definition of the jaws axis is worse (0.6±0.1mm). As a consequence, the distance between the jaw axis and the crosshair axis shows more fluctuations.

This test fulfills point 2.6.1 (“verify that crosshair is aligned with collimator rotation axis”, tolerance 2 mm) of recommendation 11.

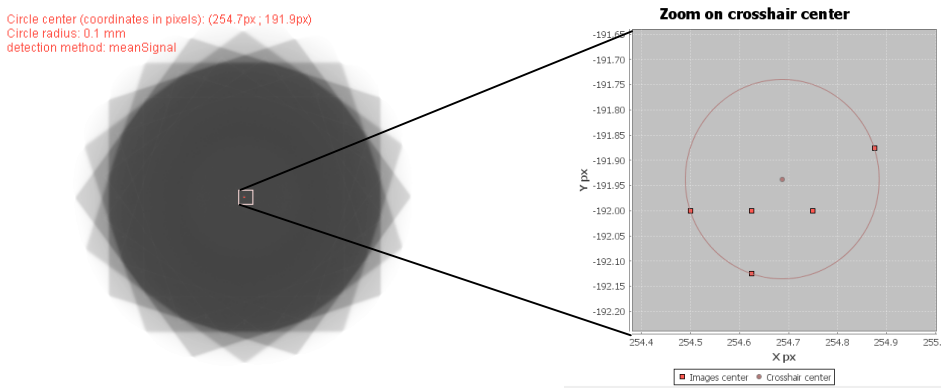

Figure 6. Superposition of the 5 crosshair images (left) and successive positions of the metallic ball on the detector (right). The circle centre defines the collimator rotation axis. Note: the pixel size is 0.784 mm

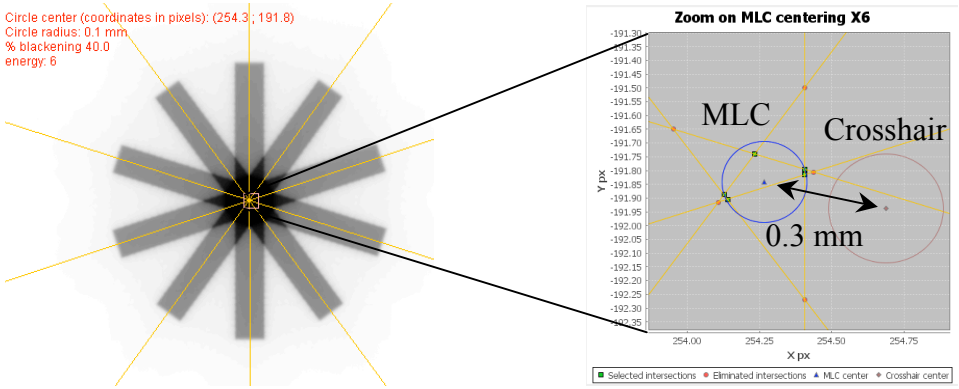

Figure 7. Superposition of the 5 MLC images (left). The centre of each MLC field is computed and shown as a yellow line. The smallest circle including all 5 internal intersections defines the position of the centre of radiation of the MLC on the detector. For comparison, the circle representing the crosshair centre (collimator rotation axis) is shown in violet

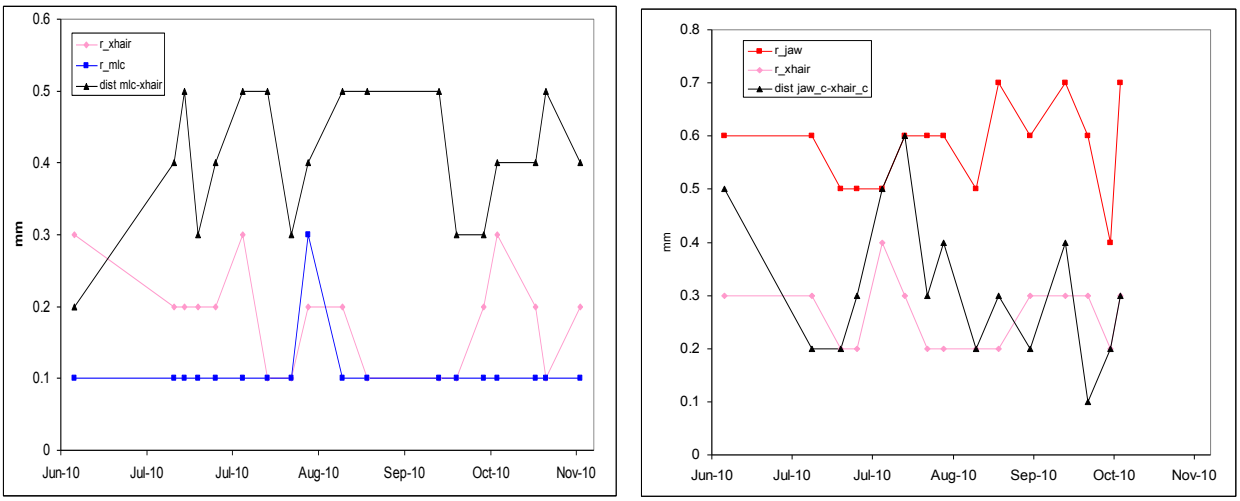

Figure 8. Comparison of the distance between the crosshair axis and the MLC centre of radiation (left) and with the centre of radiation of the jaws (right). The radius of the circles are also given in both plots, giving the accuracy with which each axis position is determined on the detector. Note: the MLC and jaw data are taken within two separate tests, this explain the presence of two crosshair curves

c) Leakage and transmission of the leaf bank, leaf/jaw alignment

The setup for this test consists of opening one MLC bank 1cm while closing the opposite jaw to 0 (Figure 9).

10 mm leaves 5 mm leaves 10 mm leaves

Jaw

1 cm

m

The analysis uses the MLC centre defined in b) as a starting point (green cross in Figure 9). The grey values of the pixels are drawn as an intensity profile across the MLC, at 3cm from the centre. This profile is displayed in pink in Figure 9 (the higher the dose, the lower the profile). It shows higher dose values in the central region of the MLC where the 0.5cm leaves are located and thus where the leakage is maximal.

MLC

The analysis for the determination of the transmission uses a segmentation based on the minima of the intensity profile. These minima are used to determine the true leaf positions. Based on this information the inter- and intra-leaf transmission can then be precisely calculated for each leaf and each inter-leaf gap.

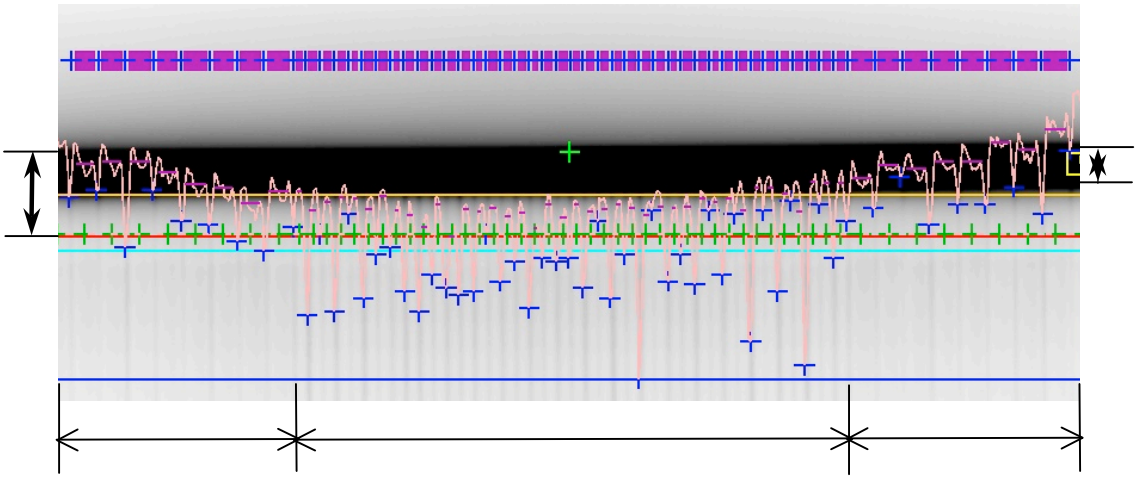

Figure 9. Measurement of inter- and intra-leaf transmission. The maximal inter-leaves leakage is found at the minima of the intensity profile and shown with blue crosses on the figure. The light and dark blue lines locate the position of the mean and maximum inter-leaf transmissions, respectively. Note: in order to show the dose leakage between the leaves, the window/level has been modified and thus the 1cm opening appears larger than it really is

During the observation period, the inter- and intra-leaf transmissions, for both banks were always below 3% (max intra-leaf transmission: 2.2%, max inter-leaf transmission: 2.7%). The average of the mean intra was 1.7% and 1.9% while the average of the mean inter was 1.9% and 2.1% for bank1 and bank 2 resp. This test complies with recommendation 11, point 5.5 (tolerance of 5%).
Note that the same images are also used to measure the leaf bank alignment with the opposite jaw.

d) Leaf bank sagging

To measure the effect of gravitation on the leaf banks three images are taken at gantry angles 270°, 0° and 90°, respectively (Figure 10). The field is 10cm wide and defined by the MLC. For reference, a metallic ball is aligned to the field centre (crosshair) and rigidly fixed to the collimator using the tray holder. The distance from the ball to the MLC bank 1 and bank 2 is measured at 90° and 270° and then compared to the distances measured at 0°.

Figure 11 shows the amplitude of movement of the banks with time. Bank 1 values are displayed as triangles. The red curves compare the positions at 90° with the positions at 0° while the green curves compare the position at 270° with the positions at 0°. The black curves compare positions at 270° to positions at 90°, i.e. they correspond to the sum of the two deviations.
The signs of the variations are not of importance as they only depend on conventions, all bank movements are in the direction of the gravitation! The maximum amplitude is 0.5 mm at 270° and 0.4 mm at 90°, however, not for the same bank.
This test complies with recommendation 11, point 5.1 (tolerance 1 mm).

e) Orthogonality and parallelism of the leaves

To study the effect of gravitation on individual leaves, a field with two leaves extended by 12 cm, one from each bank (Figure 12) is imaged at gantry angles 0°, 90° and 270° with the collimator at 90° to have gravitation acting on the leaves.

jaw

MLC

MLC

gravitation

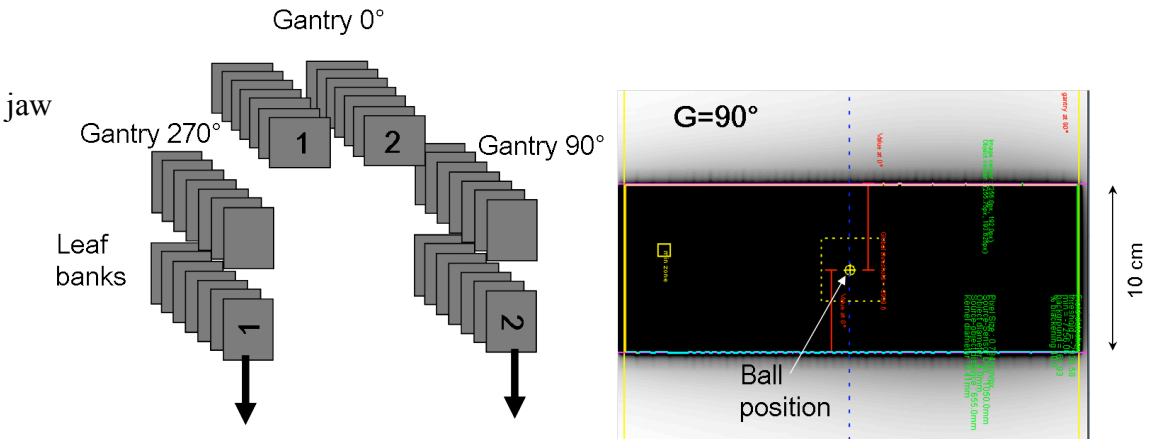

Figure 10. Effect of gravitation on the leaf banks. The distance from each leaf bank to the metallic ball at gantry 90° and 270° are compared to the reference distance measured at gantry 0°

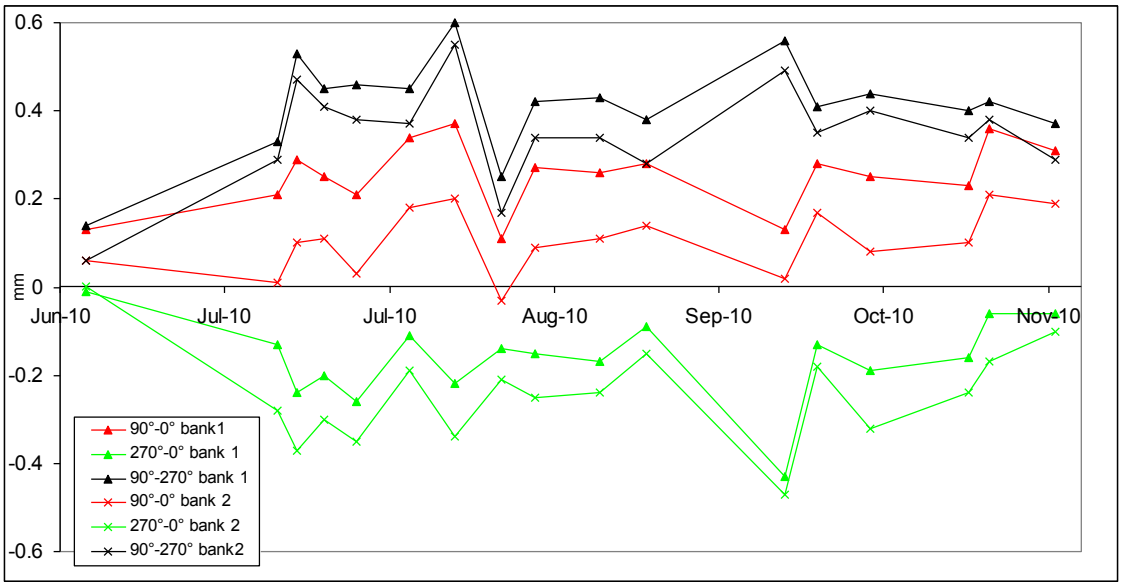

Figure 11. Leaf bank sagging curves as a function of time. Triangles show bank 1 data and crosses bank 2

Since the field is defined by the jaws on two sides, one has a rigid reference from which we can measure the distances to the two leaves. In addition, the distance between these leaves can be determined. Very little variations (of the order of 0.1° for the inter-leaves parallelism) are observed for the thin 5mm leaves. For the more rigid 10 mm leaves, the variations are even an order of magnitude smaller.

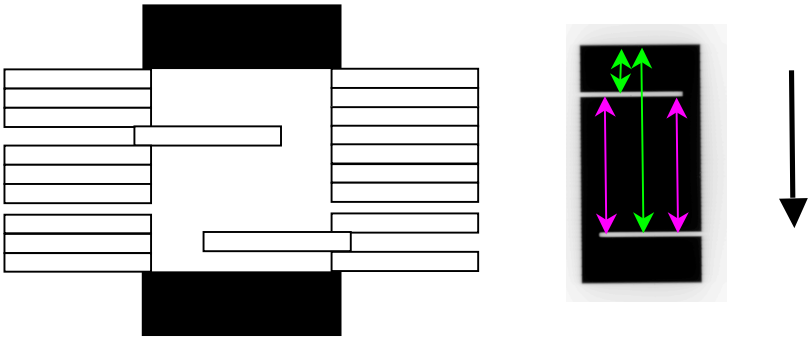

Figure 12. Illustration of the setup at gantry 90°, collimator 90° to have gravitation acting on the 2 extended leaves (left), the image is on the right. The distance between the jaws and the leaves are measured as well as the distance between the 2 leaves

Results: OBI QA module

All kV tests were made using 3 OBI images of the LEEDS TOR18FG phantom. The images were taken at 45kV, 70kV and 90kV with a 1mm Copper filter in front of the source (Figure 13).
Point 3.1 (collimation, tolerance 2 mm) of the recommendation 16 can already be checked on these images.

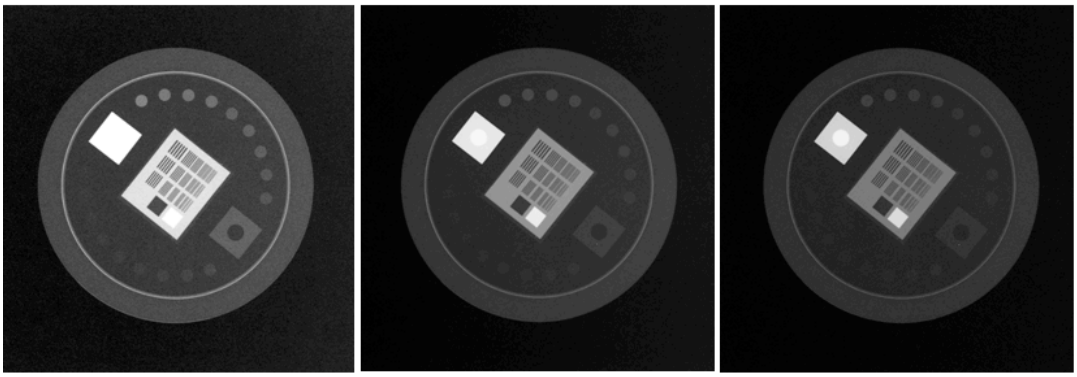

Figure 13. OBI images of the TOR18FG phantom used in the QA module

a) Spatial resolution

The spatial resolution is evaluated via the modulation transfer function (*MTF*). Here, an approximation of the *MTF* is computed using the method of Droege & Morin [1] and called MTF_p (for practical *MTF).* The central part of the TOR18FG phantom includes 21 bar patterns (Figure 14, left panel) representing 21 spatial frequencies ranging from 0.5 to 5 lp/mm. For each frequency *f*, it can be shown that the MTF_p is proportional to a ratio of modulations *M(f)* over M_0, where M_0 is related to the amplitude of the modulated signal. M_0 is measured here by subtracting the average background signal intensity from the average phantom signal intensity in the two ROIs shown in the bottom left of Figure 14.
Droege & Morin showed that the modulation *M(f)* can be expressed in terms of variances measured in ROIs centred on each of the 21 bar patterns (see e.g. the black square on the 0.5 lp/mm pattern in Figure 14, left panel).
This method has many advantages: there is neither a need for a line spread function, nor Fourier transformations, and it is insensitive to phantom alignment as well as to image noise.

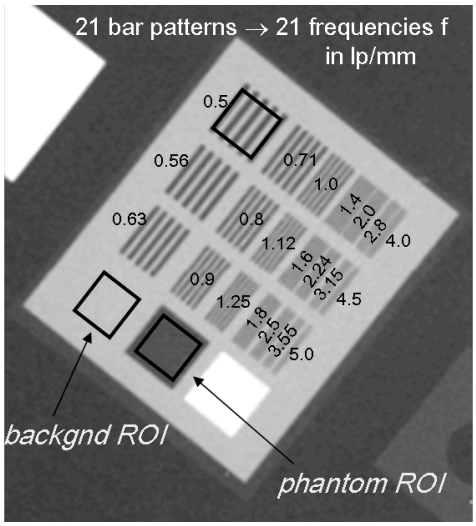

$$MTF_p(f) = \frac{\pi\sqrt{2}}{4}\frac{M(f)}{M_0}$$

where $M(f) = \sqrt{\sigma(f)^2 - \sigma_{noise}^2}$

$$\sigma_{noise} = \sqrt{(\sigma_{phantom}^{\ 2} + \sigma_{backgnd}^{\ 2})/2}$$

and $$M_0 = \frac{\left|\overline{I_{phantom}} - \overline{I_{backgnd}}\right|}{2}$$

Figure 14. For each of the 21 spatial frequency *f,* the MTF_p is computed by measuring standard deviations and average values of pixel intensities in predefined ROIs

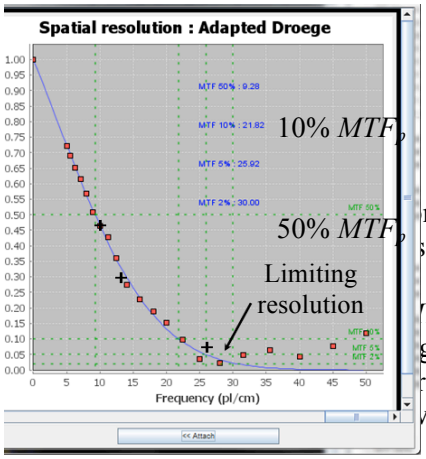

shown in Figure 15. It is normalized to 1 and the 21 points of the curves are fitted
n. We checked the curve calibration with data from the detector manufacturer
sses).

TF_p and the resolution is as follows. The resolution power of the system is given
guishable lp/mm, and it is usually assumed that a minimal modulation of 10 to
eliable detection, depending on the noise level (limiting resolution).
vel is low enough to follow in a reliable way the evolution of the 10% MTF_p with
16 (Point 4.1.2, see also [2], section II.D.1) does not specify a % MTF_p value.
However, the stated tolerance of 16 lp/cm indicates that it is corresponding to a MTF_p value between 10% and 20%, the limiting resolution obtained here is higher.

However, the MTF_p curve contains more information than just the system resolution since it provides information on the contrast resolution on the y-axis. In addition to the MTF_p 10%, we choose to follow with time the frequencies where the MTF_p is 50%, i.e. when the contrast dropped by half, sometimes called the perceived image sharpness.

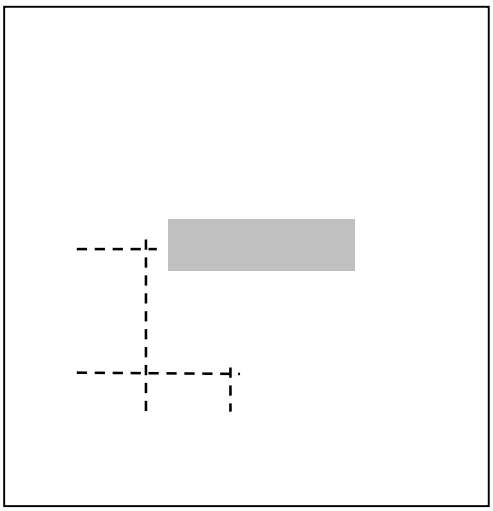

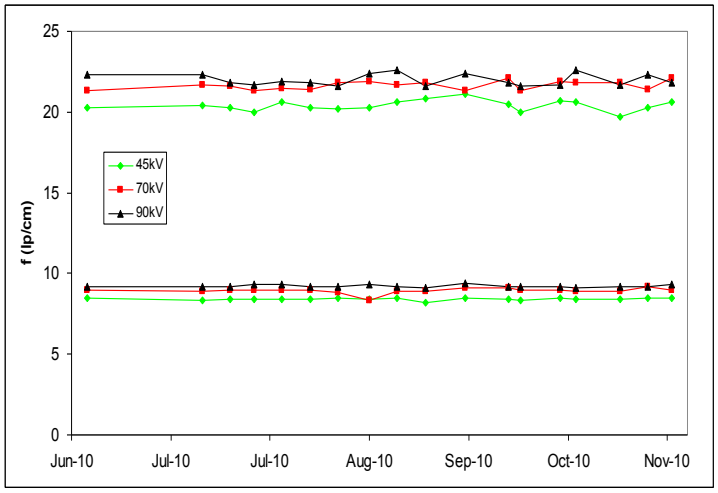

Figure 15. MTF_p (left), spatial resolution as a function of time for 50% MTF_p and 10% MTF_p (right)

We observed that the 10% MTF_p curve was always above the tolerance of the recommendation 16 and that values for both 50% and 10% MTF_p were stable with time (8.4±0.1, 8.9±0.2, 9.2±0.1 lp/cm, for 45, 70, 90kV resp. and 20.4±0.3, 21.7±0.3, 22±0.4 lp/cm for 45, 70, 90kV resp.), and that the resolution slightly increased with energy.

b) Contrast resolution

The resolution in contrast is traditionally (in diagnostic imaging) evaluated using the 18 disks of 8 mm diameter located on the rim of the TOR18FG phantom. The standard procedure is to identify in the image the least-visible disk (one has to see its full contour) and to determine the corresponding contrast value in a table given in the TOR18FG documentation e.g. if no13 is the last disc fully seen, the limiting contrast is 2.2%. This procedure, however, is rather subjective and the result depends on the observer, the noise, the contrast loss due to scatter and window level. For the energy range used here, it is common to see 11 or 12 discs, i.e. down to a contrast of about 3%.
Figure 16 (left panel) shows an image acquired with OBI at 45kV. 13 discs can be identified, corresponding to a contrast of 2.2%.

The recommendation 16, point 4.1.3, states a tolerance of 3% which corresponds in our case to 12 discs (11 discs→3.2%, 12 discs→2.7%).

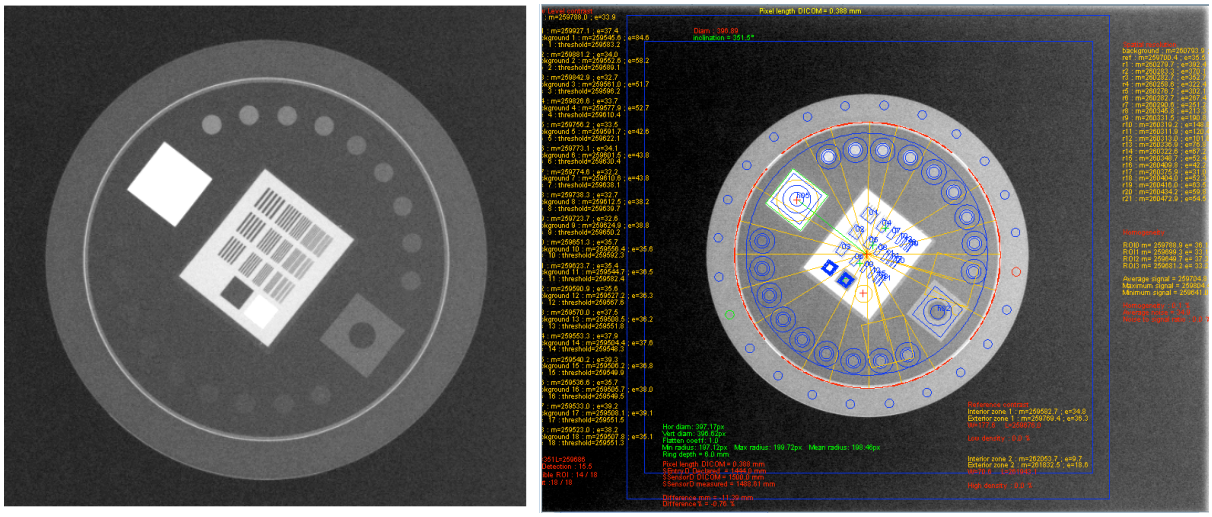

Figure 16. 45kV OBI image (left) and low level contrast analysis (right)

To reduce as much as possible the subjective side of the standard procedure, this procedure is automated in QUALimagiQ, but needs to be calibrated once to the eye of the observer. When calibrating the routine, the first step is to find the best window level that will be used in all the future measurements. The second step is to tell the software how many discs the observer has counted, which allows to associate a corresponding contrast value to each particular disc. Figure 16, right panel shows the various masks (signal and background) applied on each disc together with the pixel values measured in all ROIs. The advantage of this procedure is that for future measurements the number of visible discs will not depend on the observer anymore.
The number of detected discs over the period of observation is shown in Figure 17. The contrast is stable around a value of 13 visible discs (13.4±0.8, 13.1±0.5, 13.3±0.7 for 45, 70 and 90kV, respectively) and seldom reaches the recommendation 16 tolerance of 12 discs. There is no obvious energy dependence.

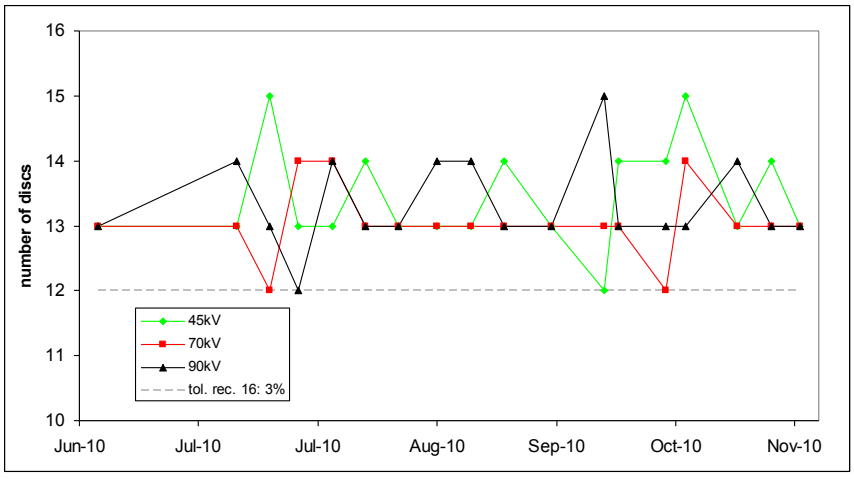

Figure 17. Number of discs observed in the image of the TOR18FG phantom as a function of time

A different measurement of the contrast is made using the lead (high density) and copper plates (low density) of the phantom (Figure 18). The objects of about 1 cm diameter are located inside a square of about 2.5 cm. The background measurement is taken in the square around the circular object. The contrast is then defined

$$contrast = \frac{\overline{I_{objectROI}} - \overline{I_{backgndROI}}}{\overline{I_{objectROI}} + \overline{I_{backgndROI}}}$$

using the average pixel intensities in the ROIs.

object

backgroundnd

The evolution of contrast with time is presented in Figure 18. For 45kV, the detector saturates for the high density object and no value of the contrast could be measured.

The contrast was constant over the period of observation, apart from a drop of about 10% of the 90kV curve for the high density object, which is under investigation.

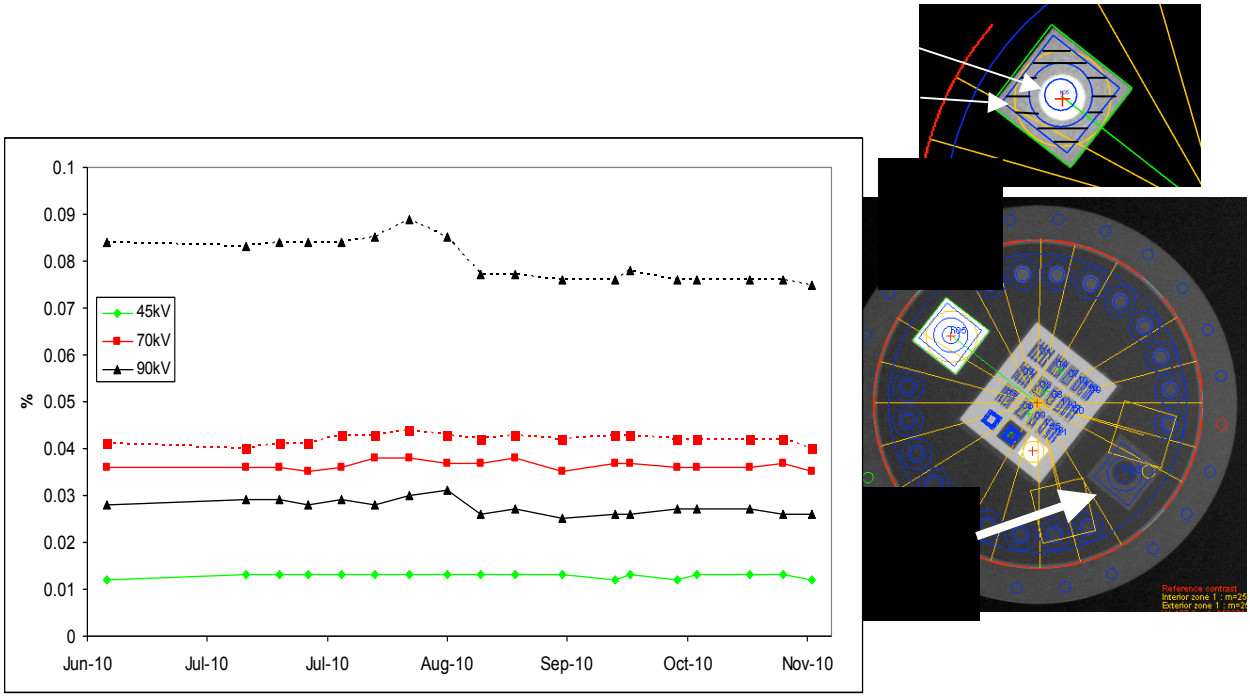

Figure 18. Contrast as a function of time (left), the lower 3 curves are for the low density object while the dotted lines are for the high density object (the 45kV curve is missing due to detector saturation). The positions of the objects are shown on the right. In the zoom on the high density object (upper panel), the window/level was adapted

c) Homogeneity

The outer rim of the TOR18FG phantom is divided in 24 ROIs, one every 15° (Figure 19, left panel). The average pixel intensities in each circular ROI is computed and plotted as a function of the ROI position on the circle (Figure 19, right panel). The sinus-like shape of the curve is explained by the Heel effect. From the curve, the maximum and minimum intensities *I* are found and the homogeneity is computed with

$$H = 2 \cdot \frac{I_{Max} - I_{Min}}{I_{Max} + I_{Min}}$$

During the observation period, the homogeneity was stable with time with fluctuations of 8.1% for 45kV, 4.8% for 70kV and 7.9% for 90kV, i.e. inside the 10% tolerance of point 4.1.5 of recommendation 16.

d) Noise

To measure the noise, four ROIs are defined at 90° intervals on the outer rim of the TOR18FG phantom and the standard deviation of the pixel intensities is measured in each of them. The noise is defined as the average value of the standard deviation in the 4 ROIs. The signal to noise ratio is found by dividing the noise by the average value of the pixel intensities in each ROI, it is of the order of 233 for 45kV, 71 for 70 kV and 67 for 90 kV. The fluctuation of the noise parameter over the period of observation is 3.5% for 45 kV, 4.1% for 70 kV and 5.6% for 90kV. This test complies with point 4.1.4 of recommendation 16 (tolerance 10% baseline).

More tests are included in the OBI QA program with QUALimagiQ and include the mechanical position tests such as the panel alignment, source-imager distance etc. They are described in II.C.3 in [2] and point 3.3 of recommendation 16 from SGSMP.

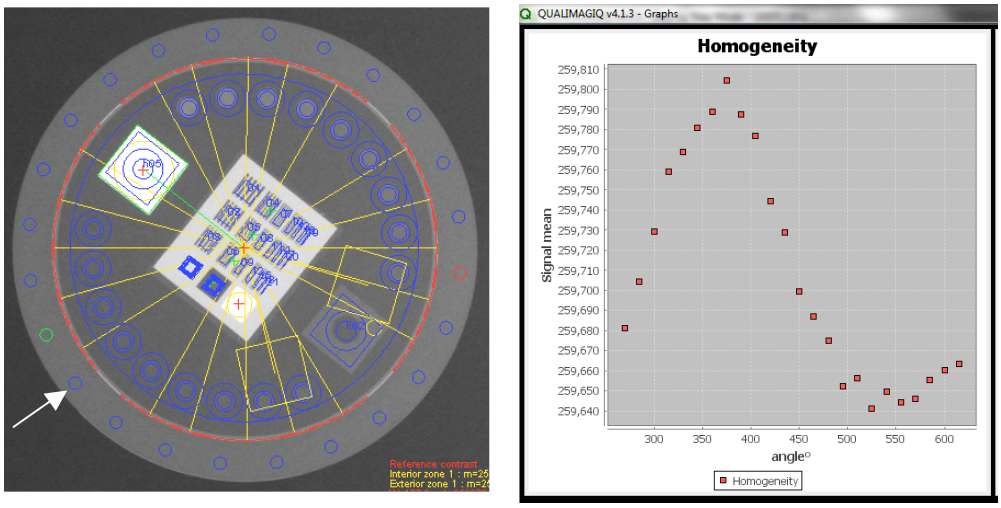

Figure 19. Positions of the ROIs (white arrow) for the homogeneity measurement on the TOR18FG phantom (left) and average pixel intensities as a function of ROI position (right)

Discussion

Thanks to the high resolution of the amorphous silicon detectors, the QA tools based on portal images allow the medical physicist to measure physical parameters with high precision (e.g. all MLC leaf positions to the tenth of mm). Out of the large amount of outputs produced by the software the relevant and meaningful information needs to be carefully selected. For a quick and easy overview, QUALimagiQ produces after each analysis a list of all parameters outside tolerance. While the configuration of such tests and tolerances requires some substantial efforts and the competences of a qualified medical physicist, data acquisition and the handling of the software proved to be quick and very easy in routine use.

During the 5 months of observation, data were acquired once per week and allowed us to quantify the amplitude and frequency of variability of the various parameters under test. For the MLC and OBI modules, the most interesting results were that

- the deviations of the MLC leaves positions to their expected positions were measured down to the tenth of mm, fluctuation are depending on the field size but were of the order of about 0.3mm;
- we studied the evolution of the distance between the crosshair rotation axis and the MLC rotation axis and found 0.4 ± 0.1mm. This value was compared to the evolution of the distance between the crosshair rotation axis and the jaw rotation axis, we found 0.3 ± 0.1mm for the latter;
- QUALimagiQ provide a very graphical way to evaluate the inter- and intra-leaf leakage, it is thus possible to localize the position of a maximum in the inter-leaf leakage for example;
- the leaf bank sagging due to gravitation was 0.6mm maximum and the individual leaf sagging was negligible;
- the high spatial resolution of the OBI measured with MTF was very stable (± 0.4 lp/mm above 20 lp/mm);
- the contrast measurement was made independent of observer and was stable (roughly 13±1disc).

To conclude, the QA software QUALimagiQ facilitates in an ideal way many of the tests required by the SSRMP recommendations 11 and 16.

This work has been funded by the Beaumont-Stiftung, Biel.

References

[1] R.T. Droege & R.L. Morin, A practical method to measure the MTF of CT scanners, Med. Phys. Vol. 9, No. 5, 1982

[2] S. Yoo et al., A quality assurance program for the on-board imager, Med. Phys. Vol. 33, No. 11, 2006

Monte Carlo characterization of a Photon MLC for Electron Radiotherapy

D. Henzen[1], N. Buchegger[2], H. Neuenschwander[3], P. Manser[1], M.K. Fix[1]
[1] Division of Medical Radiation Physics, Inselspital – University of Bern, Switzerland
[2] Institute for Biomedical Engineering, ETH and University of Zürich, Zürich, Switzerland
[3] Clinic for Radiation-Oncology, Lindenhofspital Bern, Switzerland
mail: henzen@ams.unibe.ch

Introduction

Today IMRT is used mainly for photon beams. However, for superficial tumours such as breast cancer, a photon IMRT treatment has some drawbacks due to large dose depositions in the lung and the heart. Alternatively, the application of intensity modulated electron beams using a photon MLC is proposed. A well established method for treatment planning of electrons is the Monte Carlo (MC) method. Thus, in a first step this work aims in the implementation of the photon MLC into BEAMnrc [1]. Furthermore, dose distributions for electron beams with a photon MLC calculated either with DOSXYZnrc [2] or the Swiss Monte Carlo Plan (SMCP) [3] using EGSnrc and VMC++ respectively are compared.

Material and Methods

In a first step the head of a Varian Clinac 2300C/D linear accelerator was simulated with the BEAMnrc package for different energy applicator combinations: 4, 6, 9. 12, 16, 20 MeV and 6x6, 10x10, 15x15, 20x20 and 25x25 cm^2 applicators. For each energy applicator combination two phase space (PS) files were generated: one directly above the secondary collimator jaws and one directly below the applicator. The latter PS file together with the dose calculation engine DOSXYZnrc were used to calculate dose distributions in a water phantom at a source to surface distance (SSD) of 100 cm. These dose distributions have been compared with measurements in order to determine suitable input parameters (mean energy and radius of the initial electron beam) for the MC simulations. Based on this reliable beam model, the applicators were removed and the MLC component was added to the BEAMnrc package. Simulated dose distributions for several energy applicator combinations and different MLC patterns using DOSXYZnrc at an SSD of 70 cm were compared with the corresponding measurements in a water tank. Alternatively, these dose distributions were simulated using the SMCP which has the photon MLC already available. In this case the dose distribution was calculated using VMC++ as particle transport and the PS above the secondary collimator jaws as input source. The dose distributions are compared with measurements and those calculated using BEAMnrc/DOSXYZnrc.

Results

Suitable input parameters were determined for the initial electron beams. The calculated and measured dose distributions in water at an SSD of 100 cm agree within 2% or 2 mm for all energy applicator combinations considered. Figure 1 shows the depth dose and dose profile comparisons for a 15x15cm^2 applicator for an energy of 6 MeV and 20 MeV.

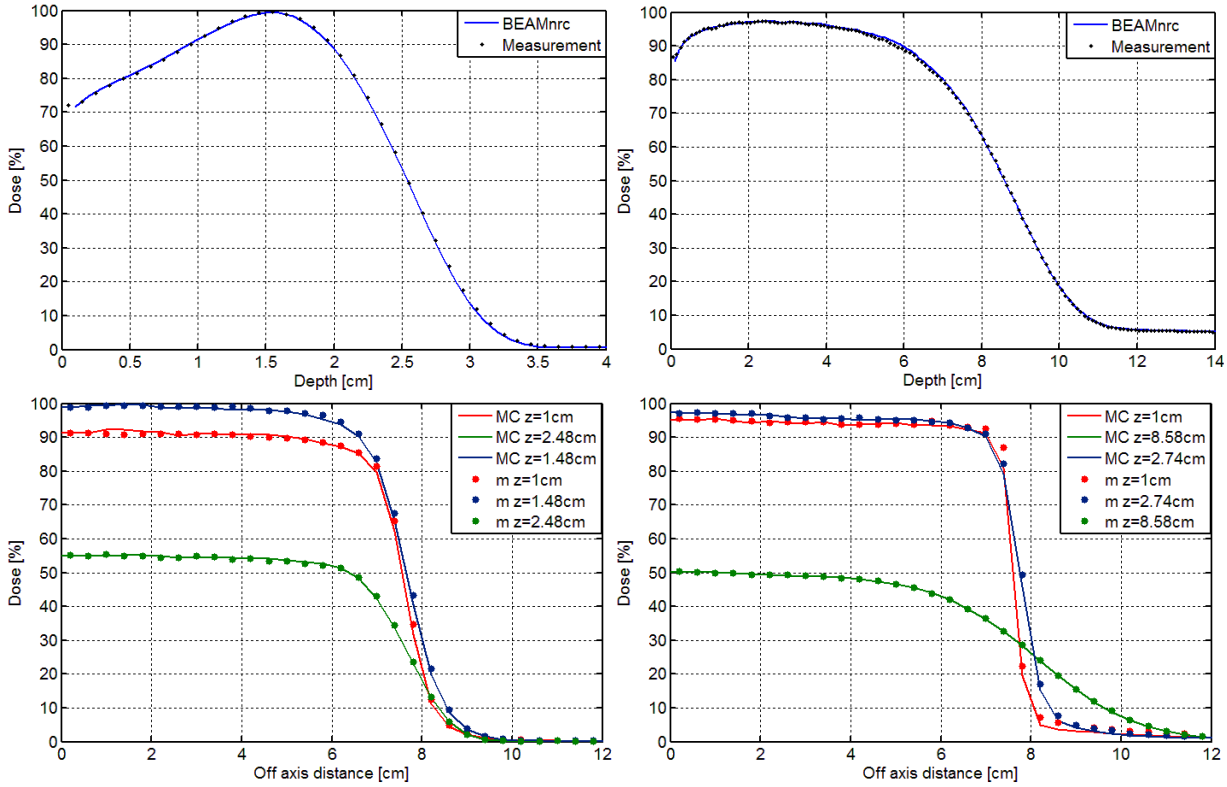

Figure1: Calculated and measured percentage depth dose curves (upper plots) and dose profiles (lower plots) for 6 MeV (left) and 20 MeV (right) for a 15x15 cm^2 applicator. The dots refer to the measurements and the solid lines to the BEAMnrc calculations, respectively.

Good agreement has been found between the calculated (DOSXYZnrc) and measured dose distribution for the MLC fields at an SSD of 70 cm. Also a good agreement was found between dose distributions calculated using DOSXYZnrc and SMCP respectively for the MLC fields. The comparison between the measurements and both MC calculations for 20 MeV and the MLC forming a 10x10cm^2 field is shown in figure 2.

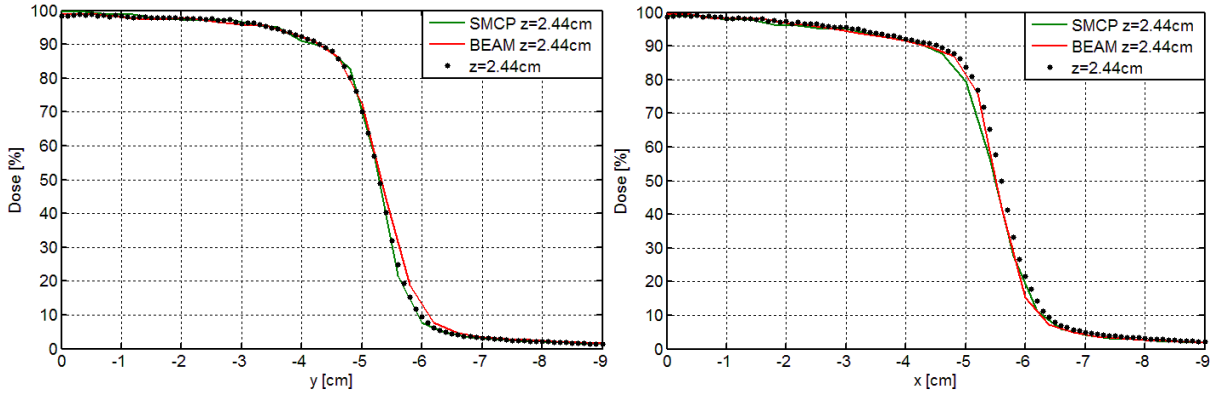

Figure2: Calculated and measured inplane (left) and crossplane (right) dose profiles for 20 MeV and the MLC forming a 10x10cm^2 field at an SSD of 70 cm. The dots refer to the measurements and the solid lines to the BEAMnrc (red) and SMCP (green) calculations, respectively.

Discussion

The linac was successfully implemented into BEAMnrc. The good agreement between the measured and calculated dose distributions for the beam model with the photon MLC demonstrates that the photon MLC can also be simulated for electron beams. Furthermore, the results suggest that using SMCP together with VMC++ allow treatment planning for electron radiotherapy using a photon MLC. This work was supported by Varian Medical Systems.

References

[1] I. Kawrakow, E. Mainegra-Hing, D.W.O. Rogers, F. Tessier and B.R.B. Walters, The EGSnrc Code System: Monte Carlo Simulation of Electron and Photon Transport, NRC Report PIRS-701, Ottawa, Canada 2009

[2] B. Walters, I. Kawrakow and D.W.O. Rogers, DOSXYZnrc Users Manual, NRC Report PIRS-794revB, Ottawa, Canada

[3] Michael K Fix, Peter Manser, Daniel Frei, Werner Volken, Roberto Mini and Ernst J Born, An efficient framework for photon Monte Carlo treatment planning, Phys. Med. Biol. 52 (2007) N425-N437, 2009

Monte Carlo implementation and characterization of the High Definition MLC

M.K. Fix, W. Volken, D. Frei, D. Frauchiger, E.J. Born, P. Manser
Division of Medical Radiation Physics, Inselspital – University of Berne, Switzerland
mail: michael.fix@ams.unibe.ch

Introduction

Radiation therapy is constantly improved by new technical developments. Recently a new MLC, the High Definition (HD) MLC (Varian Medical Systems), was commercialized providing high resolution in the center section of the treatment field. Since the HD-MLC changes the radiation field, it is important to accurately characterize the new HD-MLC for treatment planning purposes.
Monte Carlo techniques are regarded as a highly accurate method to compute dose distributions in radiation therapy. Furthermore, this technique is suitable to characterize the HD-MLC with respect to quantities which cannot be directly measured as e.g. energy distributions.
Thus, the aim of this work is to investigate the characteristics of the HD-MLC using Monte Carlo (MC) methods.

Material and Methods

Based on the information of the MC package for the HD-MLC from Varian, the HD-MLC was implemented into an already existing MC environment, the Swiss MC Plan (SMCP) [1]. The HD-MLC consists of 2x32 inner leaves with a leaf width of 2.5 mm and 2x28 outer leaves with a leaf width of 5.0 mm. The implementation has been configured by adjusting the physical density and the air gap between adjacent leaves in order to match transmission measurements for the 6 and 15 MV photon beams of a Novalis TX. The transmission measurements have been performed with gafchromic films in a sold water phantom at a source to surface distance (SSD) of 95 cm at a depth of 5 cm. Additionally, the transmission has been measured with an ionization chamber. The implementation was validated by comparing penumbra measurements (80%-20%) for different field sizes each at several depths in water with those resulting from MC simulations for 6 and 15 MV. The penumbra measurements have been performed at an SSD of 100 cm using a diamond detector in a water tank. The validated implementation of the HD-MLC has been used for its physical characterization. For this purpose, phase space (PS) files have been generated below the fully closed MLC of a 40x22 cm^2 field size for 6 and 15 MV, respectively. The phase space files have been analyzed in terms of energy spectra, mean energy, fluence and energy fluence in the direction perpendicular to the MLC leaves and have been compared with the corresponding data using the well established Varian 80 leaf MLC.

Results

Figure 1 shows the boundaries of the implemented HD-MLC geometry.

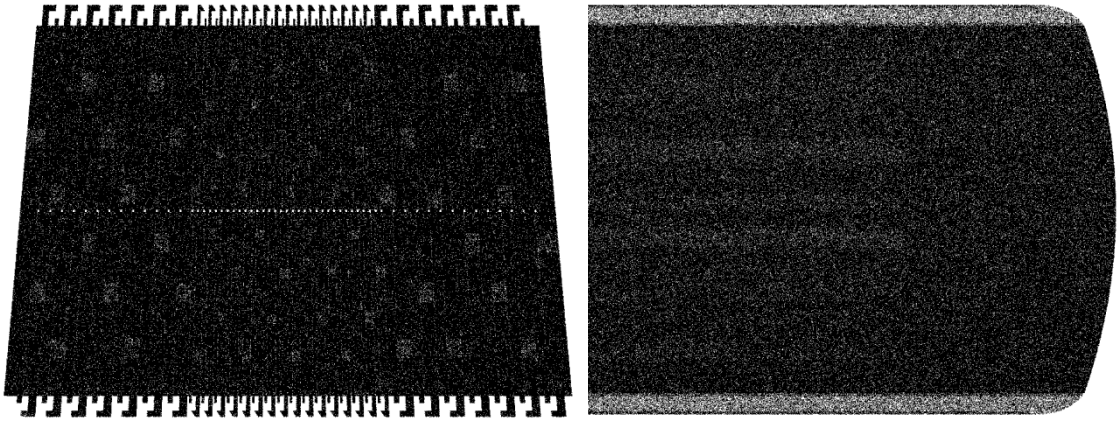

Figure 1: On the left: a view of the boundaries of the HDMLC for the very detailed implementation. On the right: a view showing the shape of the leaf end. The implementation of the screw holes is shown for all leaves.

The MC simulation of the configured HD-MLC lead to transmission values of 1.25% and 1.34% for the 6 and 15 MV beam, respectively. The corresponding ionization chamber measurements result in a transmission of 1.20% and 1.35%. Good agreement has also been found for the comparison between transmissions profiles resulting from MC simulations and film measurements for both beam energies as can be seen in Figure 2.

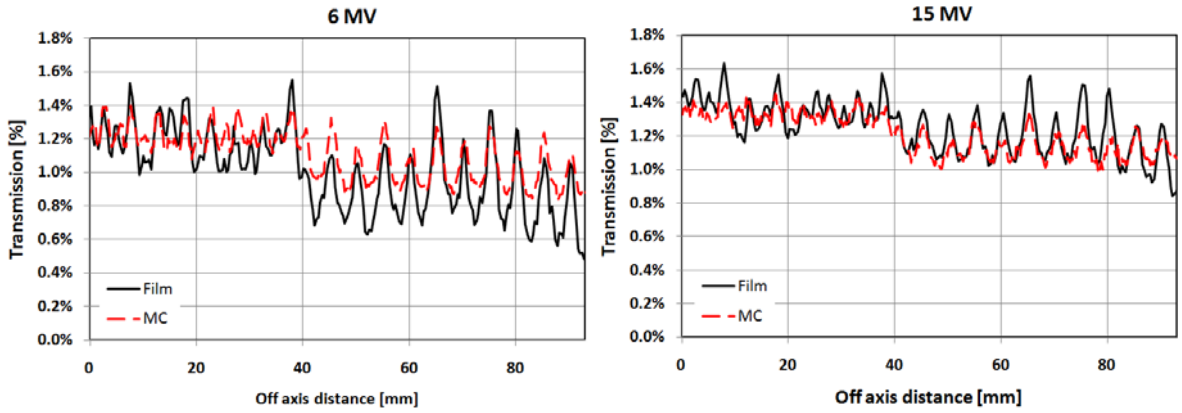

Figure 2: Comparison between measured and calculated transmission profiles using the configured HD-MLC within SMCP.

The simulated and measured values for the penumbra agreed within <0.5 mm for all field sizes, depths and beam energies. The energy spectrum and the mean energy are almost identical for the two MLCs. However, the fluence and energy fluence are significantly different. As an example the fluence distributions are depicted in Figure 3 for both beam energies.

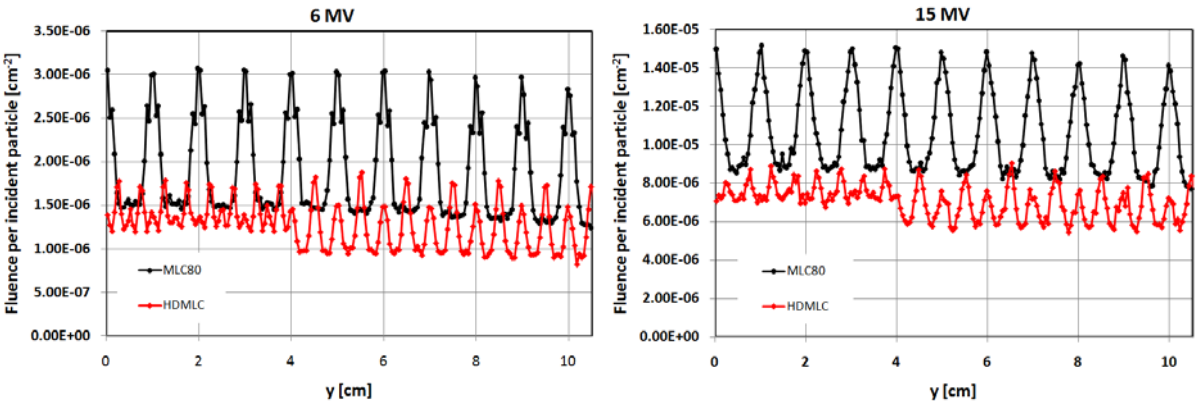

Figure 3: Particle fluence distributions of the two MLCs perpendicular to the leaves. Left: 6 MV and right: 15 MV.

Due to the different leaf widths of the two MLCs, the shape of these distributions is different; each representing its leave structure. Due to the increase in width from the inner to the outer HD-MLC leaves, the fluence and energy fluence distributions clearly decreases below the outer leaves. The 80 leaf MLC leads to an increase of the fluence and energy fluence by a factor of about 1.5 compared with those resulted for the HD-MLC.

Discussion

The HD-MLC has been successfully implemented into the SMCP. Comparisons between MC calculations and measurements show very good agreement. The PS analysis demonstrates that the lower transmission compared with the 80 leaf MLC is due to the reduction of the transmission fluence. The SMCP is now able to calculate accurate dose distributions for treatment plans using the HD-MLC.
This work was supported by Varian Medical Systems.

References

[1] M. K. Fix, P. Manser, D. Frei, W. Volken, R. Mini, and E. J. Born. An efficient framework for photon Monte Carlo treatment planning. Phys. Med. Biol., Vol. 52, 2007, pp. N425-37.

HDR dose calculation within the SMCP environment

D. Terribilini, B. Isaak, P. Manser, D. Frei, W. Volken, R. Mini, M.K. Fix
Division of Medical Radiation Physics, Inselspital and University of Bern, Switzerland
mail: dario.terribilini@insel.ch

Introduction

For HDR treatment plans the TG43 formalism is commonly used for dose calculation [1]. However, the accuracy might be limited in certain conditions such as near the body contours. Alternatively, Monte Carlo (MC) methods can be used to calculate the dose distributions very accurately. In this work, the Swiss Monte Carlo Plan (SMCP) [2] environment has been extended to calculate dose distributions of HDR treatment plans.

Material and Methods

In a previous work, the implementation of the HDR source microSelectron V2 into the SMCP has been validated [3]. In the current study this implementation has been extended in order to allow dose calculations on patient CT data. For this purpose, patient data (DICOM CT) as well as plan data (DICOM RP) are exported from the treatment planning system Oncentra Masterplan (Brachy, V 3.3 SP 1) via DICOM export. With the exported CT slices and a customized conversion curve (physical density vs. HU), a voxel phantom is generated, where coordinates, composition and density of each voxel are stored. Source positions, treatment times as well as the total reference air kerma (TRAK) are extracted from the exported DICOM patient plan. The TRAK is used for the normalization of the MC calculated dose distributions. This procedure has been validated by comparing dose distributions calculated in a large water phantom (Figure 1) using SMCP with dose distributions in the same phantom predicted by the TG43-based HDR treatment planning system.

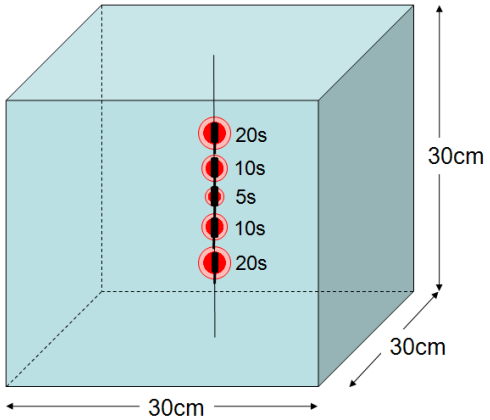

Figure 1: Design of the validation plan consisting of five dwell positions with different dwell times. This plan has been calculated in a 30x30x30cm^3 homogeneous water phantom.

Furthermore, HDR patient plans have been recalculated within the SMCP environment and results have been compared with results from the treatment planning system.

Results

For the HDR brachytherapy source microSelectron V2 of Nucletron, a normalization factor N = (8.780 ± 0.070)*10^{10} *TRAK [# particles] has been determined. This factor converts the simulated doses per emitted photon in absolute dose values.

Dose distributions calculated in the water phantom with both SMCP and the TG43-based HDR treatment planning system agree within 0.5% relative to D_{ref} (= 10Gy) for r ≥ 5mm (Figure 2).

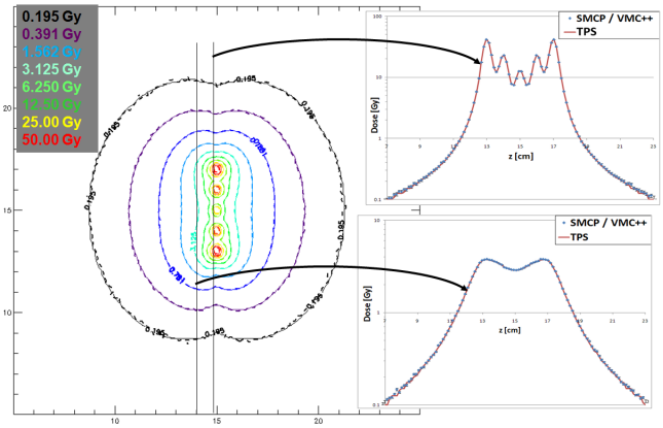

Figure 2: Results of the comparison of the dose distribution calculated in the validation phantom using SMCP with the dose distribution in the same phantom predicted by the TG43-based HDR treatment planning system.

Dose distributions calculated according to the TG43 formalism report absorbed dose to water, while MC dose distributions are expressed in dose to medium. For dose calculation comparisons, dose distributions calculated with MC have been converted to dose to water according to [4]. Simulations in patients using SMCP highlight limitations of dose calculations using the TG43 formalism, particularly at the patient surface and in inhomogeneous regions (Figure 3). In the case of breast treatments, deviations of up to 3% (relative to D_{ref} = 4Gy) have been observed

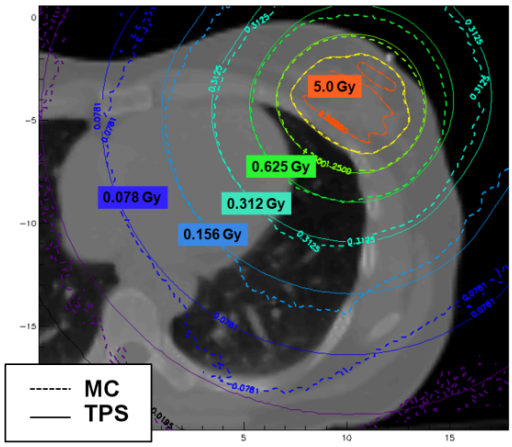

Figure 3: Comparison between the dose distribution calculated according to the TG43 formalism and the dose distributions calculated in the SMCP environment. Dose distribution calculated in the SMCP environment has been converted to dose to water according to [4].

Discussion

The MC based dose calculation for brachytherapy within the SMCP is a powerful tool to highlight limitations in the dose prediction of today's treatment planning systems, based on the TG43 formalism, which do not take inhomogeneities and body outline into account.

References

[1] Rivard M. J., Coursey B. M., DeWerd L. A., Huq M. S., Ibbott G. S., Mitch M. G., Nath R., and Williamson J. F., "Update of AAPM Task Group No. 43 Report: A revised AAPM protocol for brachytherapy dose calculations", Med. Phys. 31, 633 – 674, 2004.

[2] Fix M. K., Manser P., Frei D., Volken W., Mini R., and Born E. J., "An efficient framework for photon Monte Carlo treatment planning", Phys. Med. Biol. 52, N425-37, 2007.

[3] Terribilini D, Manser P, Frei D, Volken W, Mini R and Fix M K, „Implementation of a brachytherapy Ir source in an in-house system and comparison of simulation results with EGSnrc, VMC++ and PIN", Journal of Physics: Conference Series 74, 2007.

[4] Siebers J V, Keall P J, Nahum A E and Mohan R, "Converting absorbed dose to medium to absorbed dose to water for Monte Carlo based photon beam dose calculations", Phys. Med. Biol. 45, 983–995, 2000.

Impact of setup errors on RapidArc dose distributions using SMCP

E. Henrich, P. Manser, D. Frauchiger, E.J. Born, M.K. Fix
Division of Medical Radiation Physics, Inselspital and University of Berne, Switzerland
Mail: lisa.henrich@insel.ch

Introduction

Knowledge of geometrical uncertainties in radiotherapy is steadily increasing. Numerous publications have presented data on the accuracy of target volume delineation, organ motion, and setup uncertainty for IMRT radiotherapy. Recently RapidArc (Varian Medical Systems) has been introduced as a new treatment technique for radiotherapy. RapidArc treatment delivery is very efficient and could improve current limitations which are associated with patient and organ motion. However, RapidArc might be sensitive to setup errors due to the highly modulated delivery. Furthermore, for all radiotherapies including RapidArc therapies, the goal is to adequately treat the clinical target volume (CTV) respectively the cross tumor volume (GTV) in order to reach the aim of the therapy. The definition of the PTV is: "The PTV is a geometrical concept, and it is defined to select appropriate beam size and beam arrangements, taking into consideration the net effect of oll the possible geometrical variations and inaccuracies in order to ensure that the prescribed dose is actually absorbed in the CTV."[3]
The aim of this work was to investigate setup errors and to describe their influence on dose distributions.

Material and Methods

In this work three different setup error types have been investigated:

- Head rotation in direction of the gantry angle (3° and 4°): This error stays for all treatment fractions equal. They were generated by changing the Gantry rotation in the Dicom file.
- Random setup errors (3D isotropic Gaussian distribution with σ of 3 and 5 mm): This error occurs in all treatment fractions and is stochastically distributed.
- Systematic setup errors (∑ of 3 and 5 mm): This error is determined once and stays equal for all fractions.

It is expected that the systematic errors and the head rotation lead to a displacement of the dose distribution with respect to the CTV respectively GTV, while the random setup errors leads to a blurring of the dose distribution (Fig. 1).

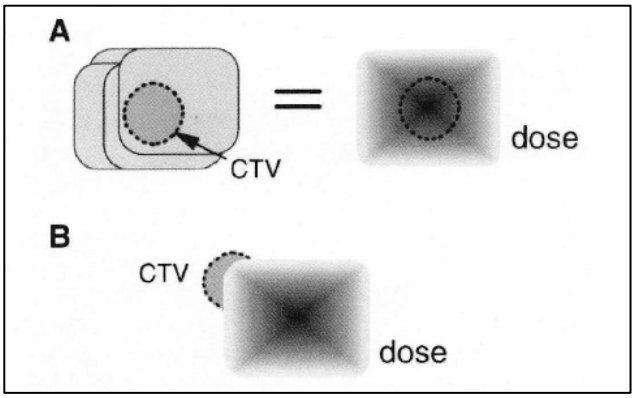

Fig. 1. Schematic drawing of the impacts [2]

These error types have been investigated for two head and neck RapidArc plans each using 2 arcs (Fig. 2).
The dose distributions for the original plans as well as for the plans with the introduced errors have been calculated using the Swiss Monte Carlo Plan (SMCP) [1].

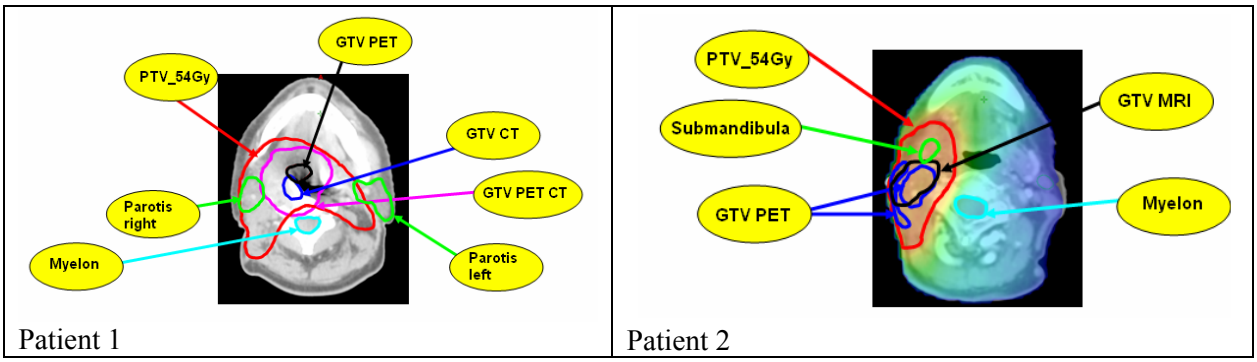

Fig. 2. The two RapidArc plans including some structures. On the left without on the right with the dose distribution included

For this purpose a graphical user interface (GUI)-based photon Monte Carlo environment was used within SMCP. Important for this work is that it is possible to generate random and systematic setup errors within SMCP. Furthermore, the SMCP is interfaced with the treatment planning System Eclipse and this gives the possibility to compare the calculated dose distributions in Eclipse.
To provide a flexible MC environment, the MC particle transport has been split into three different parts: the source, beam modifiers and the patient. Figure 3 shows the flow of the SMCP framework.

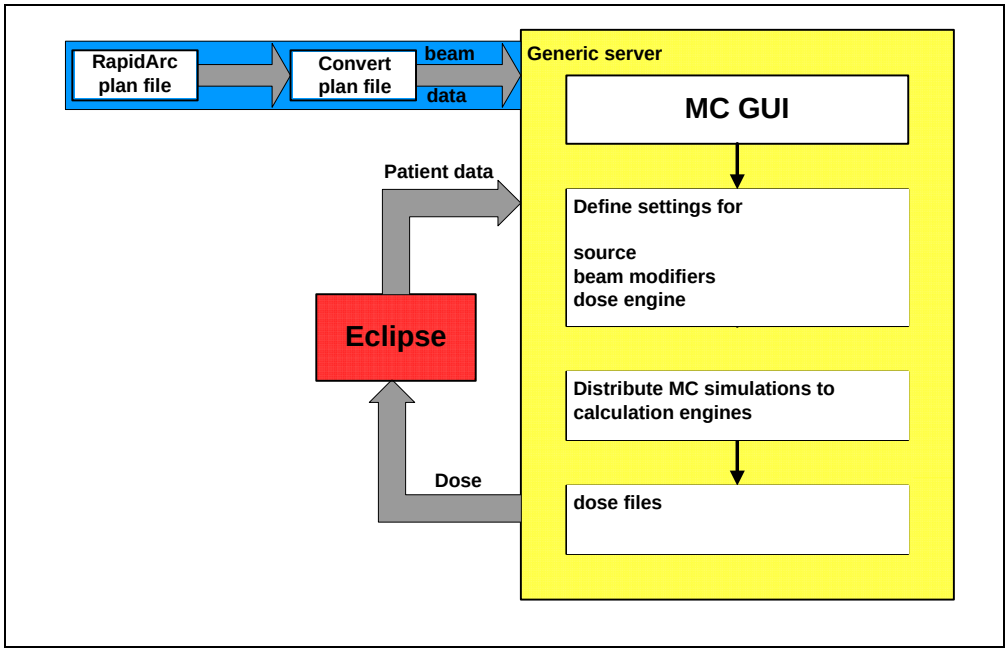

Fig. 3. Schematic flow of the SMCP framework for RapidArc

For generating the described errors the research tab of the GUI user interface has been used (Fig. 4).
In this tab the patient specific parameters can be defined. For example, to generate an isotropic random setup error of σ = 3mm 0.3 is written in the Sigma-fields (Fig. 4 (2)). Therefore, it is very simple with SMCP to generate a random setup error (for example for 27 fractions), because only one simulation is necessary, since each particle is shifted according to the specified normal distribution.

To investigate the impact of the three error types on the dose distributions, different criterions for the target volumes and the organ at risks have been analysed: isodose distributions, D_{max} respectively $D_{2\%}$, D_{min} respectively $D_{98\%}$, D_{mean}, $D_{30\%}$, $D_{60\%}$, homogeneity (HI), and a 3D gamma analysis.

Figure 5 shows a summary of the procedure used.

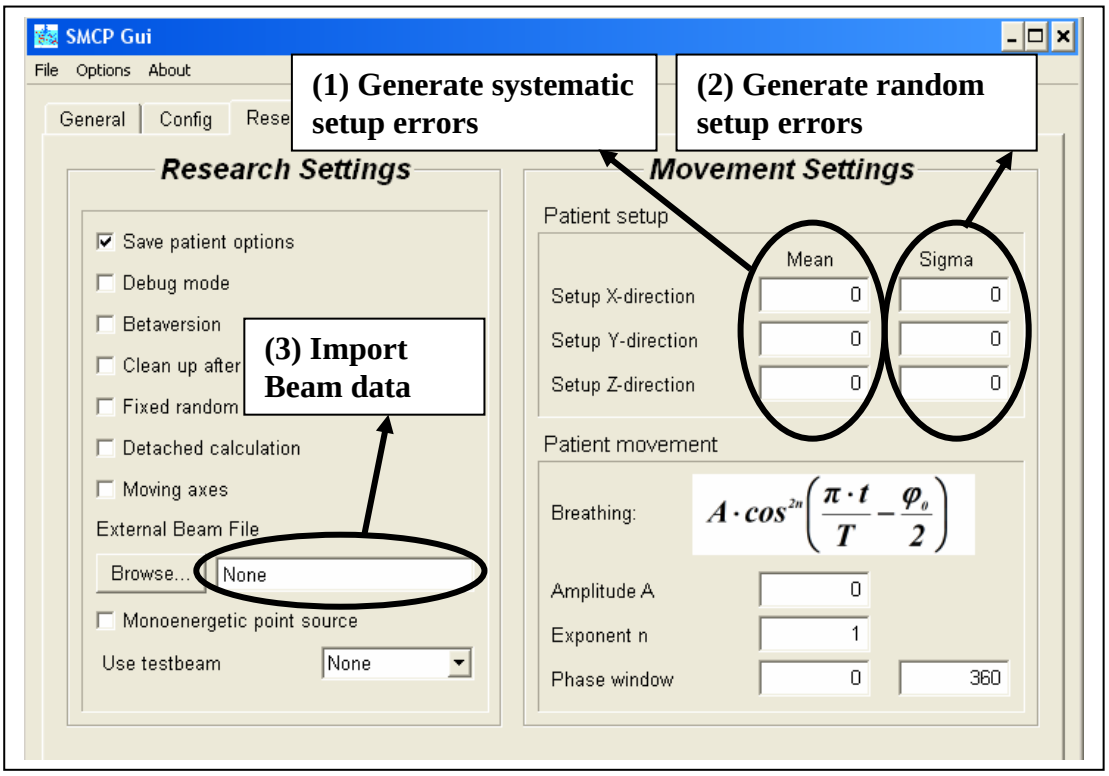

Fig. 4. The research tab of the MC GUI includes two main parts: the research settings (left) and the movement settings (right)

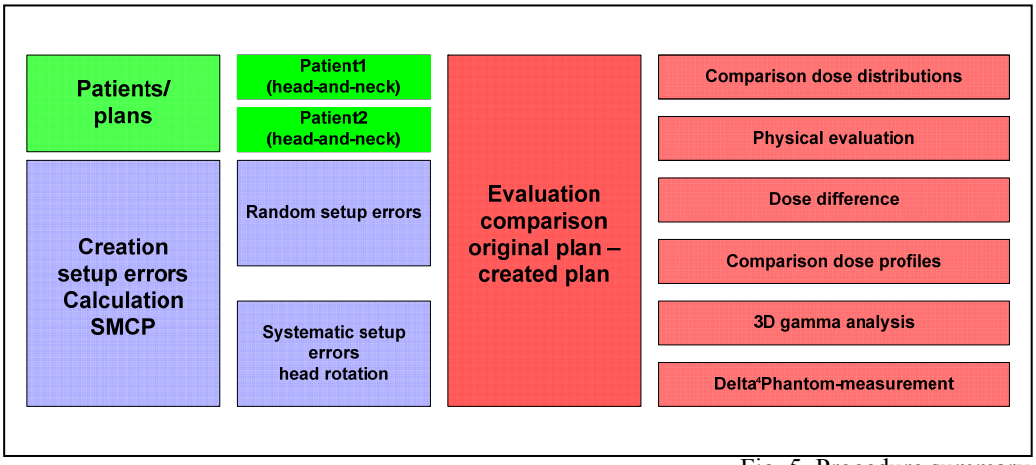

Fig. 5. Procedure summary

Results

The random setup errors produce a blurring of the dose distributions, while the two systematic errors (head rotation and systematic setup error) cause a shift of the dose distributions (Fig. 6). In addition, it is noticeable that the errors cause a decreasing of the dose in the PTV region except for the head rotations. However, the dose reduction is not observable in the GTV region (Fig. 6).

All introduced errors lead to dose differences: for the random setup errors between -14% and +8% and -24% and +8%, for the systematic random errors between -37% and +11% and -53% and 12% and for the head rotation between -18.5% and +7.4% and -25% and +22% of the prescribed dose (Fig. 7). Random setup errors cause a reduction of the dose and homogeneity in the PTV region, but not in the GTV region. This effect is also observed for the systematic setup error, while it has not been noticed for the rotation errors (Fig. 7). For the organs at risk increased dose values have been found for those structures close to the PTV (Fig. 8).

Random setup errors

original | 3 mm random setup | 5 mm random setup

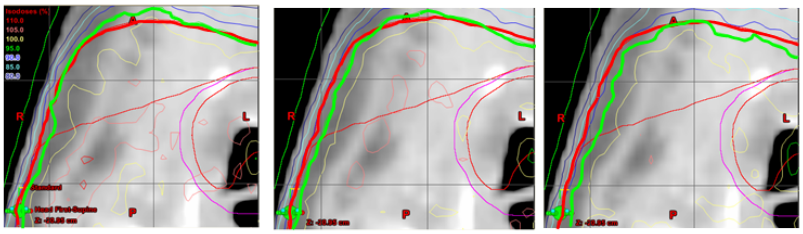

$D_{95\%}$ (PTV) = 52 Gy (96%)
$D_{95\%}$ (GTV PET) = 52.9 Gy (98%)

$D_{95\%}$ (PTV) = 51.1 Gy (94%)
$D_{95\%}$ (GTV PET) = 53.2 Gy (99%)

$D_{95\%}$ (PTV) = 49.1 Gy (91%)
$D_{95\%}$ (GTV PET) = 53.4 Gy (99%)

Systematic setup errors

original | 3 mm isotropic | 5 mm isotropic

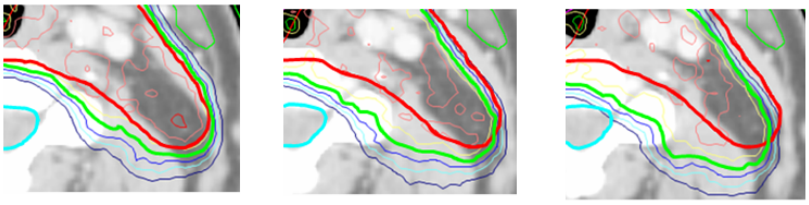

$D_{95\%}$ (PTV) = 52 Gy (96%)
$D_{95\%}$ (GTV PET) = 52.9 Gy (98%)

$D_{95\%}$ (PTV) = 49.7 Gy (92%)
$D_{95\%}$ (GTV PET) = 52.8 Gy (98%)

$D_{95\%}$ (PTV) = 44.8 Gy (83%)
$D_{95\%}$ (GTV PET) = 52.8 Gy (98%)

Head rotation errors

original | 3° head rotation | 4° head rotation

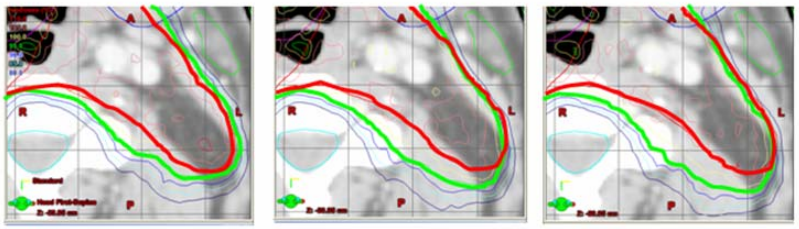

$D_{95\%}$ (PTV) = 52 Gy (96%)
$D_{95\%}$ (GTV PET) = 53 Gy (98%)

$D_{95\%}$ (PTV) = 51.8 Gy (96%)
$D_{95\%}$ (GTV PET) = 53 Gy (98%)

$D_{95\%}$ (PTV) = 51.6 Gy (95%)
$D_{95\%}$ (GTV PET) = 53 Gy (98%)

Fig. 6. Dose distributions for the investigated errors (PTV region red, 95% Isodose green) The values in parentheses are related to the prescribed dose (54 Gy)

Random setup errors

3 mm random setup

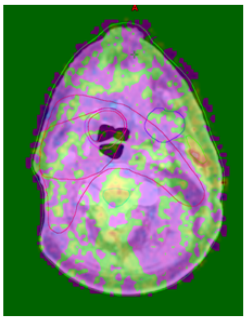

HI (PTV original) = 87%
HI (PTV 3 mm) = 85%
HI (PTV 5 mm) = 83%

HI (GTV P original) = 92%
HI (GTV P 3 mm) = 94%
HI (GTV P 5 mm) = 94%

5 mm random setup

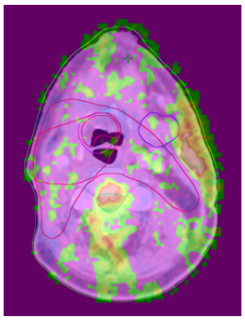

D(random 3 mm) – D(original) ∈ [-7;4.4] Gy
D(random 5 mm) – D(original) ∈ [-13;4.5] Gy

Systematic setup errors

3 mm systematic setup

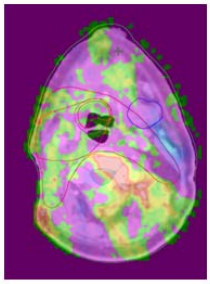

HI (PTV original) = 87%
HI (PTV 3 mm) = 81%
HI (PTV 5 mm) = 67%

HI (GTV P original) = 91%
HI (GTV P 3 mm) = 91%
HI (GTV P 5 mm) = 90%

5 mm systematic setup

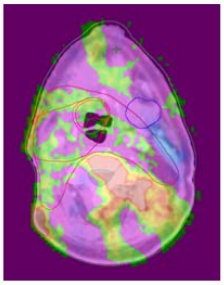

D(systematic 3 mm) – D(original) ∈ [-20.5;6] Gy
D(systematic 5 mm) – D(original) ∈ [-30;6] Gy

Head rotation errors

3° head rotation

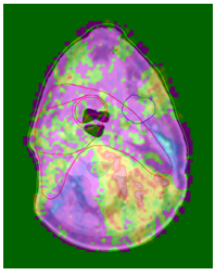

HI (PTV original) = 87%
HI (PTV 3 mm) = 87%
HI (PTV 5 mm) = 87%

HI (GTV P original) = 99%
HI (GTV P 3 mm) = 99%
HI (GTV P 5 mm) = 99%

4° head rotation

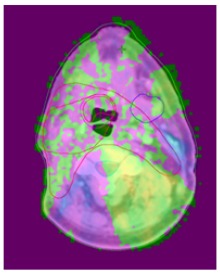

D(systematic 3°) – D(original) ∈ [-10;4] Gy
D(systematic 4°) – D(original) ∈ [-13.7;11.7] Gy

Fig. 7. Dose difference range and homogeneity for the investigated errors

$$\left(HI = \left(1 - \frac{D_{2\%} - D_{98\%}}{D_{50\%}} \right) \cdot 100 \right)$$

Random setup errors

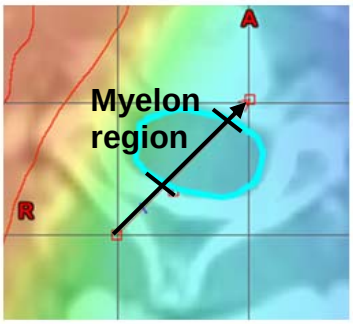

$D_{2\%}$ (Myelon original) = 25.2 Gy
$D_{2\%}$ (Myelon 3 mm) = 25.9 Gy
$D_{2\%}$ (Myelon 5 mm) = 27 Gy

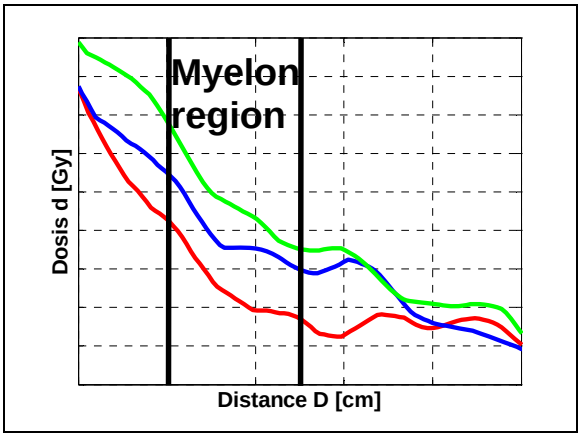

$D \in [-1;1.5]$ cm; $\Delta D = 0.5$ cm

$d \in [18;27]$ Gy; $\Delta d = 1$ Gy

Systematic setup errors

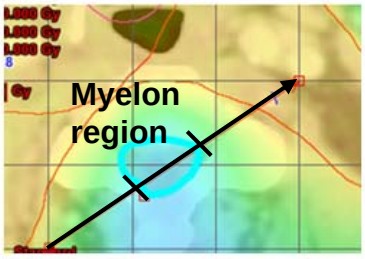

$D_{2\%}$ (Myelon original) = 29.7 Gy
$D_{2\%}$ (Myelon 3 mm) = 34.6 Gy
$D_{2\%}$ (Myelon 5 mm) = 40 Gy

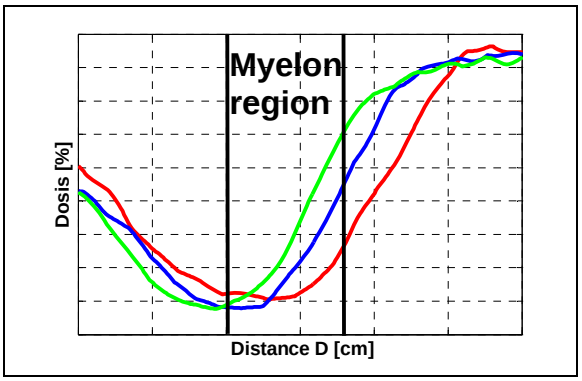

$D \in [-2;4]$ cm; $\Delta D = 1$ cm

Dosis $d \in [15;60]$ %; $\Delta d = 5$ %

Head rotation errors

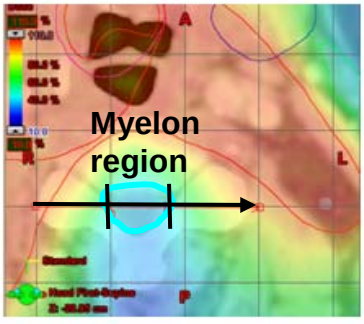

$D_{2\%}$ (Myelon original) = 29.7 Gy
$D_{2\%}$ (Myelon 3 mm) = 30.5 Gy
$D_{2\%}$ (Myelon 5 mm) = 31.3 Gy

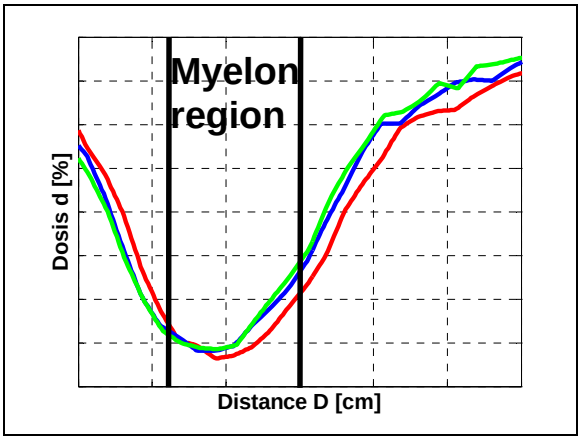

$D \in [-2;4]$ cm; $\Delta D = 1$ cm

$d \in [30;110]$ %; $\Delta d = 10$ %

Fig. 8. Dose profile comparisons of the investigated errors for the myelon region (original red, the largest error green)

Discussion

With SMCP it is possible to generate the three types of setup errors and to study the impact of these errors on the dose distributions. The effect of setup errors cannot be neglected in RapidArc treatment, although so far only two plans have been investigated. The impact of systematic errors (head rotation, systematic setup errors) is much larger than the impact of random setup errors. The results of this study might depend on the geometry of the considered patients, the uncertainty of the dose calculation in the SMCP or the selected margins for the RapidArc plans. Furthermore the same study should be performed for IMRT cases in order to put the results of the current study into perspective.

Van Herk et al. [2] suggest changing the definition of the PTV:
„In our opinion, the definition of PTV should therefore be modified and be: The PTV is the volume, defined in treatment room coordinates, to which the prescribed dose must be delivered in order to obtain a clinically acceptable and specified probability that the prescribed dose is actually received by the CTV, which has an uncertain location.
To compute this probability, accurate statistics of all errors in the treatment chain should be known. Because the margin for treatment preparation (systematic) errors is much larger than the margins for treatment execution (random) variations, particularly all preparation errors must be studied in details.“

References

[1] M. K. Fix, P. Manser, D. Frei, W. Volken, R. Mini, and E. J. Born. An efficient framework for photon Monte Carlo treatment planning. Phys. Med. Biol., Vol. 52, 2007, pp. N425-37.

[2] M. van Herk, P. Remeijer, C. Rasch, and J. V. Lebesque, “The probability of correct target dosage: Dose-population histograms for deriving treatment margins in radiotherapy, “ Int. J. Radiat. Oncol. Biol. Phys. 47, 1121-1135 (2000).

[3] ICRU (International Commission on Radiation Units and Measurements) Report 50: Prescribing, recording and reporting photon beam therapy, Bethesda, Md, USA, (1993).

A fast and independent 2D dose calculation model for IMRT fields

D. Frauchiger, P. Manser and M. K.Fix
Division of Medical Radiation Physics, Inselspital – University of Berne, Switzerland
mail: daniel.frauchiger@insel.ch

Introduction

Introducing IMRT in clinics lead to more time consuming quality assurance (QA), especially before IMRT treatment starts. One part of the pretreatment QA is the independent monitor units (MU) check for the IMRT fields. Different solutions exist to perform such a check, either a measurement can be done (EPID, film, ionization chamber, diode array) or the MUs can be calculated independently. The goal of this work was to implement a fast, independent and flexible 2D dose calculation in water to reduce machine time for patient specific QA and to be independent of a commercially available product.

Material and Methods

A convolution model has been implemented in IDL™ [1] which needs only the information of the leaf positions at the applied MU fraction (segments) for the IMRT field - sliding window or step and shoot technique - to calculate a 2D dose distribution in water at a depth perpendicular to the beam direction. The model consists of a leaf kernel, transmission, calibration depth factor and a tongue and groove parameter as shown in the following equation:

$$p(x,y,d) = c(d) \cdot \left[\left(\frac{\sum_s \left[D_S(x,y) + T_S(x,y) + G_S(x,y) + tf \cdot Tm_S(x,y) \right]}{N} \otimes k(x) \right) \otimes g(x,y) \right] \cdot MU$$

$p(x,y,d)$	dose at coordinates (x,y) in the dose plane
$k(x) = \frac{1}{1 - slope \cdot \lvert x \rvert}$	refers to a leaf kernel [2] (see Figure 1)
$D_s(x,y)$	open beam per MLC segment s
$T_s(x,y)$, $G_s(x,y)$	tongue and groove values per MLC segment s
$Tm_s(x,y)$	transmission per MLC segment s
tf	beam quality depending transmission factor
g(x,y)	scatter occurring in the water
N	number of segments used for the calculation
c(d)	PDD value of a 10x10cm^2 field at depth d

Hereby D(x,y), Tm(x,y) and N are all taken out of the MLC file for the IMRT field. c(d) is obtained from an absolute dose measurement at depth d and at the SSD used for IMRT QA. The factor tf corresponds to the mean leaf transmission for the beam quality used and is measured during commissioning. The values for T(x,y) and G(x,y) can be derived from a picket fence measurement. To determine the parameters slope and the size of the Gaussian function, a dynamically applied slit (5mm) measurement using the IMRT QA setup has to be performed.
Using an optimized parameter set 26 patients with a total of 154 IMRT fields (6MV and 15MV) were used to calculate 2D dose distributions at the depth of 7.35 cm and at a SSD of 92.65 cm.

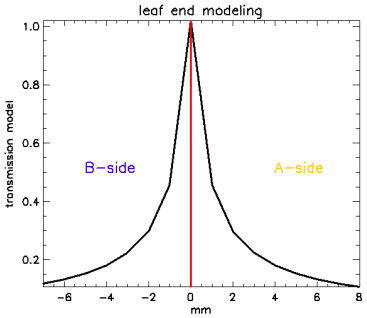

Figure 1: Visualisation of a leaf kernel function for a closed leaf pair at central axis [2].

Results

The calculation time for an IMRT field was less than one second on a standard desktop PC. All 154 resulting dose distributions were compared with TPS calculated dose distributions using the gamma analysis with criterions of 3% of the maximum field dose and 3 mm. Only points with a dose higher than 10% of the maximum dose of the field were analyzed. The gamma analyses lead to a passing rate of 98.7% of the voxel (range: 93% – 100%).
Figure 2 shows an example of the IDL implementation.

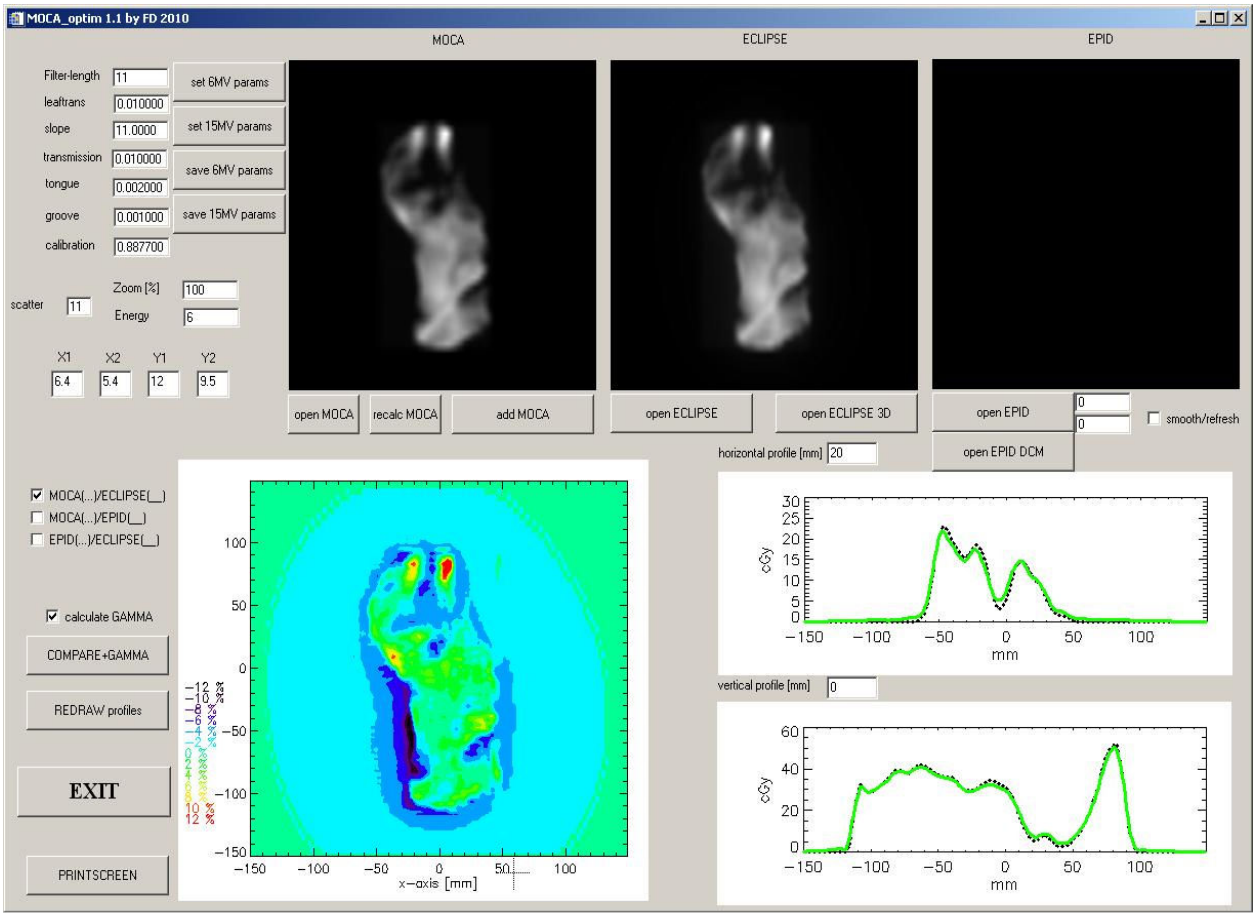

Figure 2: Comparison of model calculation (MOCA) versus TPS calculation (ECLIPSE) in IDL. A dose difference map as well as a horizontal and vertical profile are shown below the calculated 2D dose distributions. The example shows a calculation result for a Varian HD MLC IMRT field using the sliding window technique.

Discussion

A very fast and independent 2D dose calculation model is presented. Good agreement between model calculations and TPS calculations for 2D dose distributions in water was obtained.
Model calculations can be compared to TPS calculations for patient specific QA purposes. Machine QA has still to be done regularly, but not on patient specific data.

References

[1] IDL Users Guide 6.2
[2] ETH Dissertation 13124, H. Keller, p.131-133

Three-dimensional noise power spectra of MDCT systems: How to compute it and what information can be extracted?

F. Miéville[1], F. Gudinchet[2], F. Bochud[1] and F. R. Verdun[1]
[1]Institute of Radiation Physics, University Hospital Center and University of Lausanne
[2]Department of Radiology, University Hospital Center and University of Lausanne
mail: frederic.mieville@chuv.ch

Introduction

Unlike the pixel standard deviation, the noise power spectrum (NPS) takes into account both the magnitude and the spatial frequency content of the noise related to a particular computed tomography (CT) protocol. However, although the NPS is being used more and more to assess the noise properties of multidetector (MD) and cone-beam (CB) CTs, no standardized 3D NPS methods have been proposed yet [1]. The purpose of this work is to show the parameters that influence the NPS assessment and to present the potential of such a tool. Simulated and measured NPS were computed while varying the number of measured noise volumes as well as the size and the overlap of the volume of interest (VOI). Effects of the background and the stationarity of the images were also investigated. Finally, based on these considerations, the best trade-off to obtain a robust 3D NPS was discussed.

Material and Methods

Measurements were performed on a homogenous phantom (25 cm in diameter and 30 cm long) using a 64-MDCT scanner with a tube voltage of 120 kVp and a $CTDI_{vol}$ of 50 mGy. Image reconstruction was performed with the standard reconstruction filter and a matrix size of 512^2 pixels. The noise volumes were then simply formed by successive CT images stacked along the *z* direction.
Simulations were carried out using an in-house program written in MATLAB 7.7 (Mathworks, USA).

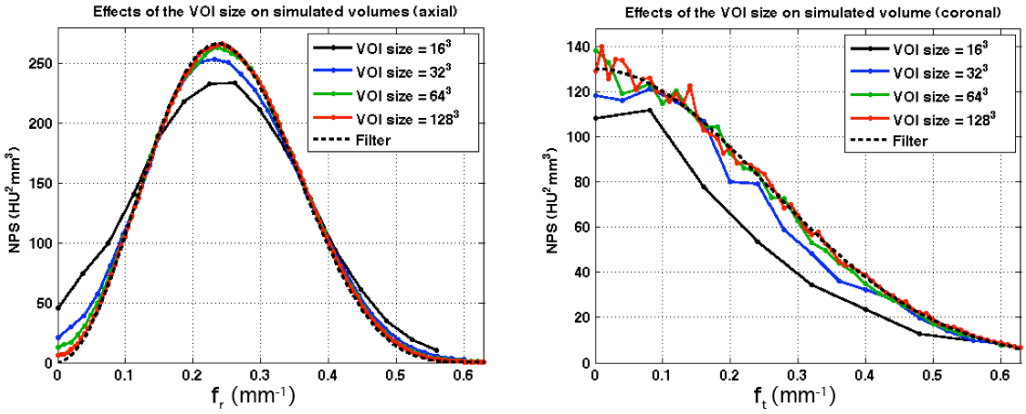

Fig. 1: Average radial profiles and coronal profiles obtained from the axial and coronal projections of a 3D NPS, respectively (see Figure 1). The 3D NPS were computed from a 256^3 pixel simulated noise volume. Small VOI sizes produce NPS curves far from the reference given by the filter whereas a VOI size between 64^3 and 128^3 pixels leads to an accurate estimation of the NPS.

Results

The size of the VOI affects the accuracy of the method. By reducing the VOI size, low frequencies are cut off leading to significant errors on the low frequency range as shown in Figure 1. While a VOI overlap of a quarter of VOI length slightly reduces the statistical fluctuations affecting the NPS curve, a NPS measurement based on repeating volume acquisitions lead to a strong reduction of the statistical fluctuations on the NPS curve. Effect of the background also plays a major role and should be removed from the VOI using an adapted linear plane instead of a constant one. Because in most cases the image noise is not spatially invariant (Fig. 2), the concept of global NPS should be replaced by the concept of a local NPS.

Discussion

While the NPS computation requires stricter conditions than the ones for the standard deviation, it provides a basis for a better objective and quantitative evaluation of image quality. To measure the NPS metric in a volume made from 512x512 pixel images, a VOI size of 64^3 or 128^3 pixels is recommended. Moreover, to significantly reduce the statistical fluctuations produced by quantum noise, more than one acquisition should be performed. Good results were obtained using three identical acquisitions leading to three noise volumes.

As shown in recent papers [2, 3], the 3D NPS metric is used to compute model observers based on 3D diagnostic task and predict the performance of CBCT scanners and tomosynthesis systems. However, an accurate and reliable detectability index could be only carried out if the 3D metrics are properly computed. This work emphasizes the importance of defining a standardization method for image quality metrics.

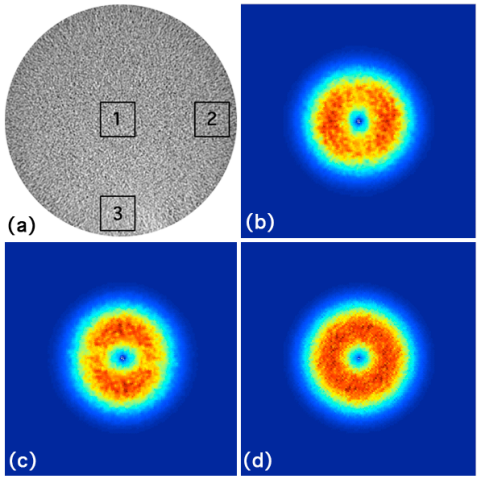

Fig. 2: Axial projection of a 3D NPS as a function of the position. The 3D NPS was produced using a commercial 64-MDCT scanner. (a) VOI positions in the CT noise volume and NPS computed from (b) position 2, (c) from position 1 and (d) from position 3.

References

[1] Boedeker K. L., Cooper V. N., and McNitt-Gray M. F., "Application of the noise power spectrum in modern diagnostic MDCT: Part I. Measurement of noise power spectra and noise equivalent quanta," Phys. Med. Biol., Vol. 52, No. 14, pp. 4027-4046, 2007.

[2] Richard S. and Samei E., "Quantitative imaging in breast tomosynthesis and CT: Comparison of detection and estimation task performance" Med. Phys., Vol. 37, No. 6, pp. 2627-2637, 2010.

[3] Gang G. J., Lee J., Stayman J. W., Tward D. J., Zbijewski W., Prince J. L. and Siewerdsen J. H., "The Generalized NEQ and Detectability Index for Tomosynthesis and Cone-Beam CT: From Cascaded Systems Analysis to Human Observers" Proc. of SPIE, Vol. 7622, pp. 76220Y-1-76220Y-11, 2010.

A Novel Phantom for Dynamic CT Imaging

D. Henzen[1,2], B. Driscoll[3], H. Keller[3]
[1]Division of Medical Radiation Physics, Inselspital – University of Berne, Switzerland
[2]Institute for Biomedical Engineering, ETH and University of Zurich, Zurich, Switzerland
[3]Princess Margaret Hospital, Toronto, ON, CA
mail: henzen@ams.unibe.ch

Introduction

Dynamic imaging aims at quantifying the change of the biodistribution of a physiological agent in the body. The shape of the time-concentration curve of a contrast agent for different tissues or organs can then be used to tell if they behave normally by comparing the shape to kinetic models. Dynamic imaging is a fairly complex technique. In order to receive quantitative analysis tool, dynamic imaging requires an validation. This is challenging as there is a lack of absolute truth of flow rates and transfer coefficients of the involved tissues. The main goal of this work therefore was to develop a phantom with well defined and reproducible flow characteristics that is able to simulate clinically relevant contrast dynamics. In addition a spatio-temporal compartment model was implemented to predict the output functions of the phantom.

Material and Methods

The flow phantom consists of cylinder made of ABS plastics with an embedded coil of tubing called the 'snake' which has ten holes drilled into it. The fluid enters the phantom through the snake, diffuses into the cylinder and exits the system through two different outputs, connected to the snake and the cylinder respectively. Depending on the positions of the valves on the two outputs, the phantom generates a certain split ratio of one input flow rate into two output flow rates which can also be measured. In this study the split ratio was measured for several positions of valves on the two outputs by which different output flow rate functions were created. For the measurement of the time-concentration curves a contrast agent (iodine) was added to the glycerol flow system and a dynamic CT scan was performed. Using AMIRA (Visage Systems, Andover, MA) and MATLAB (Mathworks, Inc., Natick, Massachusetts) the time-concentration curves for different regions in the phantom were calculated. The spatio-temporal compartment model was split into an input function model and an output function model. In order to test the performance of the output function model the measured input curves were used as an input for the model. The resulting output functions from the compartment model were then compared with the measured output functions. Finally, a clinical arterial input function was applied for which the parameters of the system (flow rate, contrast concentration, valve positions) have been tuned in order to match the clinical output function as.

Results

The measurements of the split ratio showed that the split ratio does not depend on the input flow rate. Figure 1 shows that the comparison of the measured split ratio for the different valve positions with the compartment model predictions a better agreement for high flow rates (a) than for low flow rates (b) which is due to the fact that the mixture becomes more homogeneous for high flow rates. In general the output functions could be predicted well.

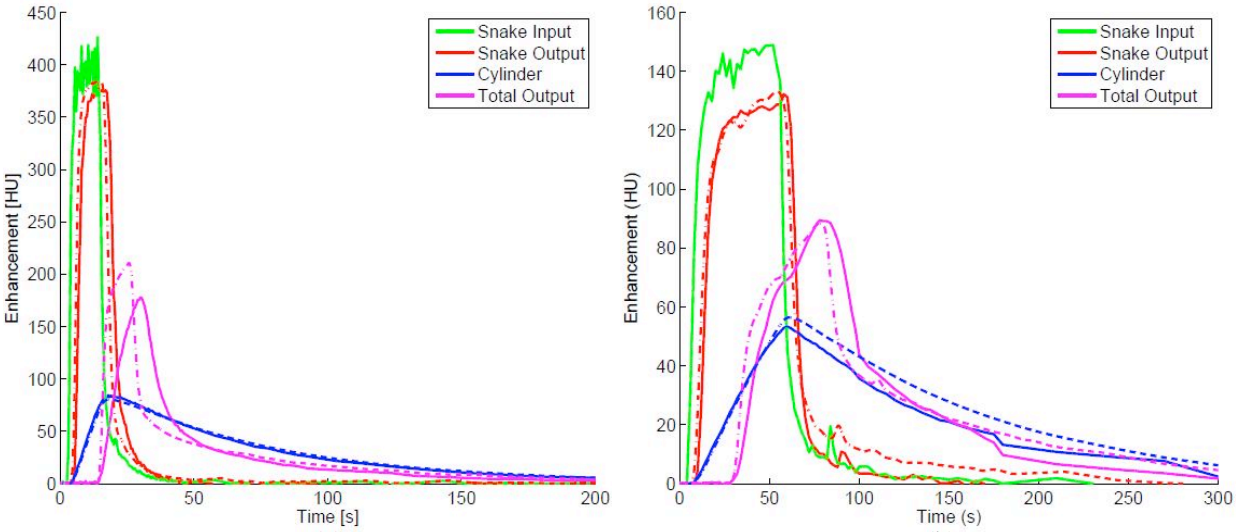

Figure 1: Predicted (solid) and measured (dash-dotted) output curves for two different setups. Since the measured input (green) curves were taken as input for the model, the input of the predicted and the measured curve are identical. The lower flow rates in the setup b) lead to worse output curves.

Comparing the clinical situation, the predicted and the measured output functions agreed very well. Although some differences exist when predicted and measured input functions are compared, the results demonstrate the feasibility of the model and that the parameters for the input function model are not yet optimal. The predicted and the measured output functions matched very well.

Discussion

The existing phantom is able to generate clinical relevant input and output functions. Combined with the spatio-temporal compartment model the different setup settings to mimick a given function can be determined. However, there exist still some differences when compared with clinical output, as the liver is a highly complex organ whereas the phantom is just a simple two-compartment model. Future projects will improve the input function model and potential applications in PET imaging.

Combination of fMRI and intraoperative MR imaging as a novel neuronavigation tool

J. Berberat[1,2], L. Boxheimer[1], J. Fandino[3], S. Lutters[1], L. Remonda[2], H. Landolt[3]
[1]Radiation Oncology, Kantonsspital Aarau, Aarau, Switzerland
[2]Neuroradiology, Kantonsspital Aarau, Aarau, Switzerland
[3]Neurosurgery, Kantonsspital Aarau, Aarau, Switzerland
mail: jatta.berberat@ksa.ch

Introduction

Intraoperative MR-imaging is used in brain tumor surgery to achieve safe and optimal tumor removal. Damage of functional eloquent brain areas should be avoided to protect the patient from any surgical-induced harm. With functional magnetic resonance imaging (fMRI) it is possible to detect functional areas of the brain, including anatomical information of an individual patient. This is crucial for e.g. localization of Broca and Wernicke areas. However, intraoperative brain shifts after craniotomy might result in an increasing inaccuracy of neuronavigation tools. The PoleStar Surgical MRI (Medtronic, Inc.) system is an intra-operative MRI image guidance system providing 3D visualization imaging for navigated surgery. We present how pre-operative fMRI (laid on top of an anatomical scan) was determining the entry point for the craniotomy and navigation was based on both, pre-operative MR examination as well as intraoperative T_2w PoleStar images.

Material and Methods

A 34-year-old patient presenting with a left parietooccipital Oligoastrocytoma (WHO II) underwent a MR examination including three fMRI tasks (linguistic and two motoric tasks) as well as anatomical scan (3D T_2 space, TR=3200ms, TE=379ms, voxel size 1x1x1, flip angle 120^o). Language function was activated using word generation task, right hand and foot functions were tested in separate motoric tasks. Block designed blood oxygenation level dependent (BOLD) [1] fMRIs were applied to the patient using the 1.5T Siemens Avanto scanner. BOLD-clusters were assessed individually for anatomical localization (Fig. 1). fMRI was performed using Echo Planar Imaging sequence (EPI, TR=3560ms, TE=50ms, flip angle=90^o, voxel size 3x3x3, matrix 64x64). The functional image analysis and overlay with anatomical serie were performed using BrainVoyager (BrainInnovationBV, Maastricht, The Netherlands).
During the operation, additional MR scans were performed with PoleStar intraoperative 0.15T MRI unit (Medtronics, USA). T_2w images were collected using following parameters: (3D FSE, TR=3000ms, TE=112ms, TI=20ms, 2 averages, 128x128) (Fig. 2).

Results

The Patient was very cooperative during the fMRI data collection, and therefore linguistic and functional areas were easy to locate (Fig. 1). Preoperative and intraoperative nonenhanced PoleStar scans showed the tumor, and its relationship to critical structures (Fig. 2).
Preoperative MRI showed a good correlation between the intraoperative MR images during the navigation. It was therefore possible for the surgeon to resect the tumor using as navigation tool the intraoperative MRI which included the activation areas acquired in the preoperative fMRI scans. This technique allowed the surgeon to avoid injury of the preoperative documented eloquent brain areas. The intraoperative images allowed for correction of the location of functional areas toward the partly collapsed and shifted resection site.

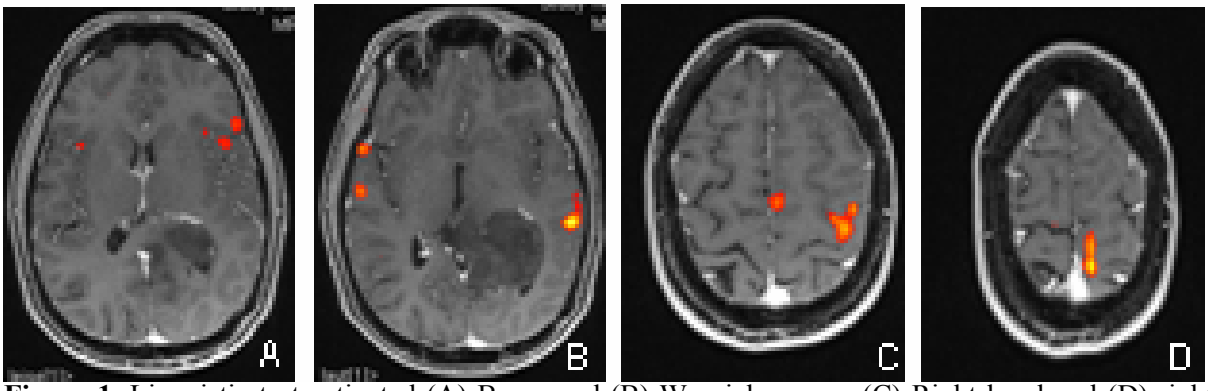

Figure 1. Linguistic test activated (A) Broca and (B) Wernicke areas. (C) Right hand and (D) right foot functional areas of the patient are also presented.

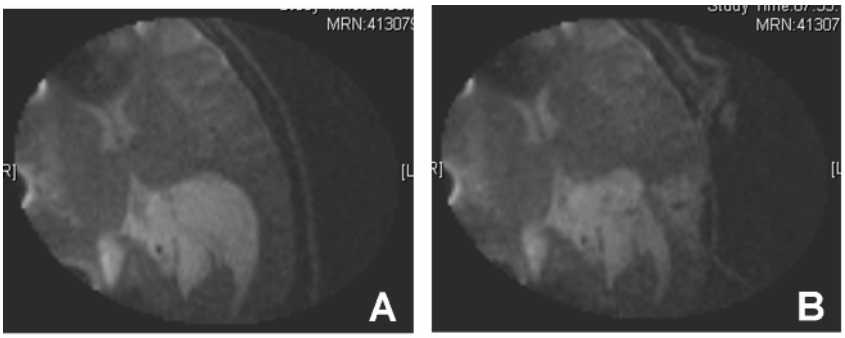

Figure 2. (A-B) Preoperative axial non-enhanced MRI showing the tumor location.

Discussion

The presented fMRI+intraoperative MR navigation protocol provides a method to localize the Broca and the Wernicke areas during the operation and at the same time to be accurate on the navigation. We have shown a method how to register a functional region and map it on the anatomical data set. This serves two purposes: first to choose a safe surgical resection strategy and second, to provide information about the eloquent points of brain activation while neuronavigation. There is a publication available on this topic [2], however, we presented the first report using the PoleStar system. Further studies are needed to investigate the fusion possibility of intraoperative MRs and preoperative fMRI, as well their accuracy and shape distortion possibilities.

References

1] Ogawa et al., Biophys. J. 64:803–812; 1993.
[2] Trantakis et al., Computer Assisted Radiology and Surgery 1230:287-291; 2001

A theoretical framework to explore low dose hypersensitivity

S. Scheidegger[1,2]
[1] Zentrum für Angewandte Mathematik und Physik, ZHAW
[2] Institut für Radio-Onkologie, Kantonsspital Aarau
mail: scst@zhaw.ch

Introduction

Some solid tumours exhibit enhanced radio-sensitivity at very low doses [1,2]. These observations may have limited importance for clinical radio-oncology, however, could provide interesting cases for exploring the dynamics of cellular repair mechanism. The low dose hypersensitivity indicates a dose dependent activation of some repair pathways. In the following, a mathematical framework to model low dose hypersensitivity is presented.

Materials and Methods

The model formulation (Γ- Model) is based on two differential equations describing the radiation induced reduction of normal tumour cells N_1 and the recovery of lethally damaged cells N_2 (with the dose rate R and the coefficients for radio-sensitivity α):

$$\frac{dN_1}{dt} = -\alpha R N_1 + \Theta(\Gamma, N_2) \tag{1}$$

$$\frac{dN_2}{dt} = \alpha R \cdot (N_1 - N_2) - \Theta(\Gamma, N_2) \tag{2}$$

Γ is a dose equivalent, which is described by the following kinetic model [3]: $d\Gamma / dt = R - \gamma\Gamma^2$. The term $\Theta(\Gamma, N_2)$ describes an additional, dose dependent repair mechanism with a characteristic dose equivalent Γ_c:

$$\Theta(\Gamma, N_2) = \vartheta \cdot e^{-\kappa(\Gamma-\Gamma_c)^2} \cdot N_2 \tag{3}$$

This approach can be justified by an activation of the additional repair process, which occurs for each cell at a different threshold dose [4]. It is assumed, that these thresholds can be characterized by a probability distribution with the maximum value Γ_c. The parameters α and Γ_c can be determined directly from the logarithmic diagram (log$S$) of the surviving fraction $S = N_1 / N_1(0)$: α by the initial slope:

$$\left[\frac{d \log S}{dD}\right]_{D\to 0} = -\alpha \tag{4}$$

The dose threshold Γ_c can be estimated from the local maximum (shoulder) of $\log S$, if low dose hypersensitivity appears. The parameters ϑ and κ can be used for fitting experimental data. The final slope of the log$S$ – curve is determined by the equilibrium of the dose equivalent $\Gamma_{eq} = \sqrt{R/\gamma}$. For this equilibrium condition, the following system of first order ODL results:

$$\begin{pmatrix} dN_1/dt \\ dN_2/dt \end{pmatrix} = \begin{pmatrix} -\alpha R & \vartheta e^{-\kappa(\Gamma_{eq}-\Gamma_C)^2} \\ \alpha R & -\left(\alpha R + \vartheta e^{-\kappa(\Gamma_{eq}-\Gamma_C)^2}\right) \end{pmatrix} \begin{pmatrix} N_1 \\ N_2 \end{pmatrix} \tag{5}$$

The final slope of the log$S$ – curve is linear and dose rate dependent since the Eigenvalues of the system Eq. (5) are:

$$\lambda_{1,2} = -\alpha R - \frac{\vartheta}{2} \cdot e^{-\kappa(\sqrt{R/\gamma}-\Gamma_C)^2} \pm \frac{1}{2}\sqrt{4\alpha R \cdot \vartheta e^{-\kappa(\sqrt{R/\gamma}-\Gamma_C)^2} + \vartheta^2 e^{-2\kappa(\sqrt{R/\gamma}-\Gamma_C)^2}}$$

Results

The differential equations are solved numerically by using a Runge-Kutta-algorithm. The results reveal a good agreement with experimental data (Fig.1). The log$S$ – curve shows the typical pattern for low dose hypersensitivity.

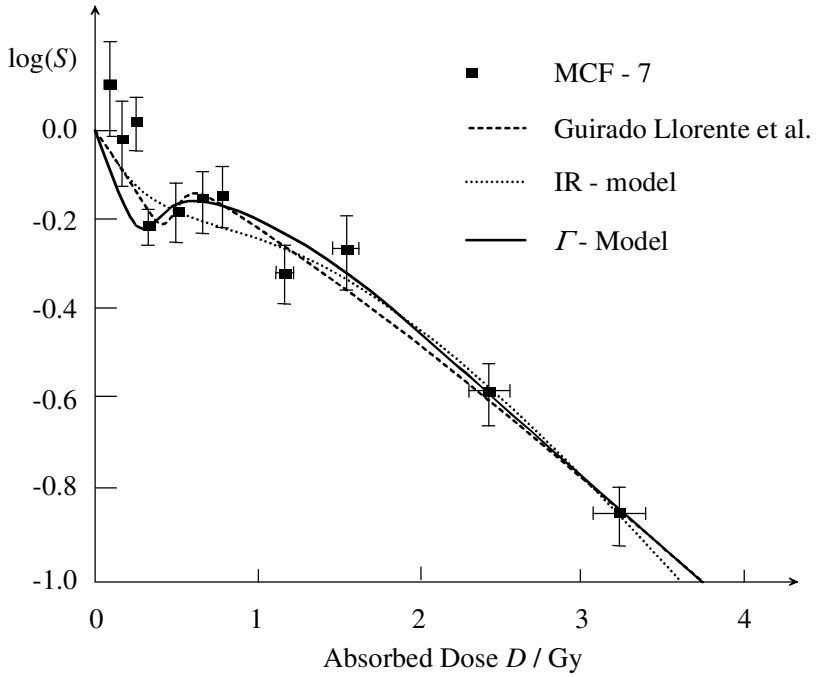

Fig.1. Comparison of the proposed Γ- Model with the model of Guirado Lllorente et al., the IR-Model and experimental data (irradiated multi cellular spheroids of breast cancer MCF-7 cell line) [4]; Parameters: $\alpha = 2.5$ Gy^{-1}, $\gamma = 0.729$ Gy^{-1} min^{-1}, $\Gamma_C = 0.6$ Gy, $\kappa = 14$ Gy^{-2}, $\vartheta = 20.833$ min^{-1}.

Discussion and Conclusions

In contrast to mathematical fitting-functions without mechanistic background, the proposed model formulation using differential equations allows different scenarios for dose dependent enhancement of cellular repair to be distinguished. The model implies that tumour cells are eliminated in two steps. Tumour cells (population size N_1) are converted by radiation into cells with sub-lethal damage (population size N_2). Further irradiation can convert these sub-lethal damages into lethal damages. With increasing values of the dose equivalent Γ, sub-lethal damaged cells also can be recovered by a dose dependent repair mechanism represented by the function $\Theta(\Gamma, N_2)$. The use of the kinetic model for Γ implies, that there are two different repair mechanisms: First, the dose equivalent is fading away during and after irradiation. This mechanism is not directly responsible for cell survival. Secondly, the dose equivalent is responsible for the activation of the additional repair mechanism which reduces the cell killing effect of the αR- dependent term in Eq. (1). The dose rate dependency is mediated by the dose equivalent Γ. The proposed Γ- Model exhibits for the parameters selected in Fig.1 a similar dose rate dependency between R = 10 Gy/d and 2000 Gy/d as observed for the LPL- model of Curtis [5], especially when using second order kinetics for Γ. Dose rate effects should be investigated in more detail for cell lines exhibiting low dose sensitivity.

In contrast to the IR- (induced repair)- Model [6], both the model of Guirado Llorente [4] and the Γ- Model are dealing with a statistically distributed dose threshold. The use of the dose equivalent Γ in combination with the probability distribution Eq. (3) is a simplistic approach to the repair mechanism, which can be influenced not only by an isolated intracellular repair pathway but also by the intercellular response of surrounding cells.

References

[1] Lambin P, Malaise EP, Joiner MC: Might intrinsic radioresistance of tumour cells be induced by radiation? *Int. J. Radiat. Oncol. Biol.* **69** (1996), 279-90.

[2] Mothersill C, Seymor CB, Joiner MC: Relationship between radiation – induced low dose hypersensitivity and the bystander effect. *Radiat. Res.* **157** (2002), 526-32.

[3] Scheidegger S, Lutters G, Bodis S: A novel approach for biomathematical modelling to predict treatment response for combined radiotherapy modalities in patients. *Molecular Radiation Biology / Oncology*, **8** (2009), 72.

[4] Guirado Llorente D, Aranda M, Ortiz Seidel M, Mesa Pérez JA, Vega Fernandez JMDL, Martinez Luna RJ, Zamora Ardoy LI, Villalobos Torres M, Lallena AM: Low dose hypersensitivity in mulicellular tumour spheroids. *Radiother. Oncol.* **96** (2010), Supl. 1, 607-8.

[5] Curtis SB. Lethal and potentially lethal lesions induced by radiation – A Unified Repair Model. *Radiat. Res.* **106** (1986), 252-70.

[6] Joiner MC, Johns H: Renal damage in the mouse: The response to very small doses per fraction. Radiat. Res. **114** (1988), 385-98.

Respiratory Liver Motion Extraction for Proton Therapy from 4DCT by Deformable Registration

Y. Zhang[1,2], D. Boye[1,2], A. Knopf[1], C. Tanner[2], A. J. Lomax[1]
[1] Center for Proton Therapy, Paul Scherrer Institut, Switzerland
[2] Computer Vision Laboratory, ETH Zürich, Switzerland
mail: ye.zhang@psi.ch

Introduction

Proton therapy with active scanning beam delivery system has significant advantages compared to conventional radiotherapy technique.[1,2] By using protons, the delivered dose can be more confined in the target and thus the dose to the surrounding tissue can be greatly reduced.[3,4] By using active scanning, patient specific collimators and compensators are not absolutely necessary, and more flexibility is available to the treatment planning for obtaining highly conformal dose distributions to the target volume. However, so far only static targets have been treated in this way, since moving targets potentially lead to interplay effects[5,6], which could deteriorate the prescribed homogeneous dose distribution more significantly than conventional radiotherapy. Such interplay effects are due to the non-synchronization between two dynamic systems, the active scanning beam delivery and the target motion. As such, motion does not only generate dose blurring, but can also result in hot or cold spots inside of dose distribution. These dose inhomogeneities can generally not be solved by the conventional safety margin approach.
Possible solutions of motion management for particle therapy can be broadly classified into four major categories: motion control (including breath hold, forced shallow breathing etc.), beam gating, beam tracking and rescanning. All of the above techniques require the motion information from both dynamic systems. For the active beam, the beam sequence is usually determined by the Treatment Control System, and is therefore well known and deterministic. On the other hand, for the moving target, motions can vary quite a lot from case to case and even for the same individual. Consequently, in order to calculate the expected time resolved 4D dose distribution in the target volume, exact information about the target motion is necessary for 4D treatment planning and for the further optimization of dose distributions in the presence of motion.

Material and Methods

I. Motion extraction by using deformable registration
In this study, respiratory liver motion has been extracted from 4DCT data sets by using intensity based deformable registration. Firstly, the B-Splines and Demons algorithms [7], have been implemented using the ITK toolkit with different combinations of parameters. An Affine transformation can be applied as an initial alignment before the main registration. In addition, a liver mask option can be taken into account for registration using segmentation. A leave-one-landmark-out test has been used to assess registration performance as a function the presence of pre-implanted landmarks.

II. Evaluation of Registration Performance
In order to evaluate the accuracy of each registration approach or combined approaches, the methods of contour-based propagation and landmark-based error tracking have been employed from both qualitative and quantitative aspects. The former method is used to visually compare the warped contours after registration to the liver shape in the real image, in order to evaluate the registration accuracy at the liver boundary. The latter method is used to quantitatively analyze the registration error by calculating Euclid distances between the estimated landmark positions and the real landmark positions in each of the ten time phases. In this way, the performance of each approach could be assessed.

III. 4D dose calculation base on the estimated motion
The obtained deformation fields from the above registrations have been used to estimate liver motion, and have been incorporated into our Treatment Planning System for calculating time resolved 4D dose distributions. Both single scanning and eight times volumetric rescanning have been considered. The results of the dose distribution from these two kinds of motion estimates have then been evaluated and compared by using percent dose difference analysis and DVH curves.

Based on these techniques, the following have been investigated:

- Does the use of a target mask help the registration process?
- Does the use of an initial Affine alignment help the registration process?
- To what extent is the accuracy of the registration process dependent on the use of implanted markers?
- Which of the deformation algorithms (B-splines or demon) is most suitable for the registration of liver data from CT images?
- How sensitive are 4D dose calculations on the type registration used?

Results

I. Respiratory liver motion extraction from 4DCT

The best relative registration result for the non-contrast liver CT images has been achieved by using a non-masked Demons algorithm with affine transformation as the initial alignment (ADW). Based on the landmark error tracking method, the largest registration errors, reaching 8mm, are found at the two end-inhalation phases (with initial displacement 13mm). For the other eight time phases, the registration errors can be nicely controlled below 4.5mm, which is within the dose grid size (5mm) for the dose calculation. See *Fig.1a*.

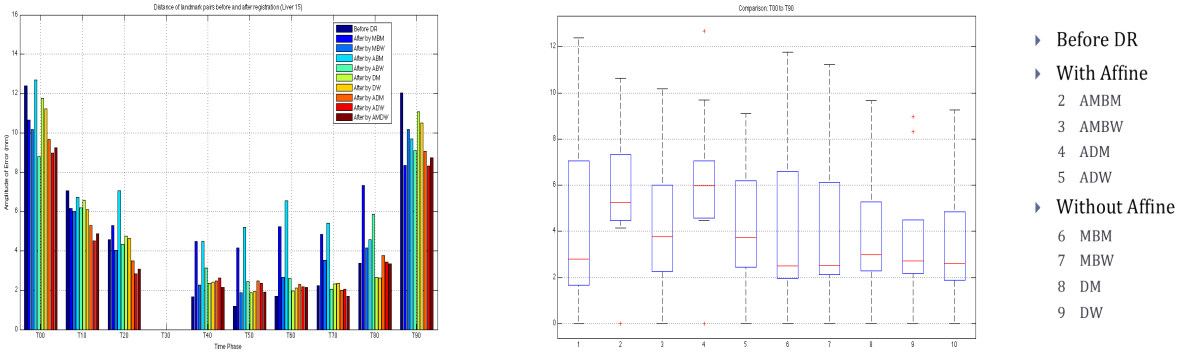

Fig.1 Registration Error amplitude for different registration methods
(a. Mean error amplitude in time phase;
b. Box plots<x-axis: algorithm; y-axis:error amplitude in mm>)

In *Fig.1-b* the results are presented as function of algorithm in the form a box-plots. Each box-plot in the figure represents a set of time resolved errors in ten time phases from one registration approach. Moreover, as the result of leave-landmark-out test shown in *Fig.2*, B-splines is quite depended on the the presence of landmarks, especially when not using the segmentation option, while Demons are rarely affected. The main challenge for registration algorithm in this application was the generally low contrast in the liver CT images, which provides less information and therefore makes registration difficult.

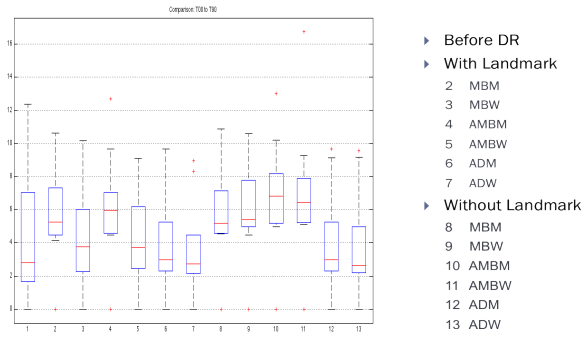

Fig.2 Leave-landmark-out test:
Box plots of error amplitude for difference registration methods

II. Influence of motion to 4D dose calculation

Fig. 3 shows one example of a 4D dose calculation taking into account real non-rigid motion, which is obtained using the deformable registration algorithms described above. The motion files used in this experiment have been generated by ADW, the best relative registration method, and for another reference technique, the B-splines without mask. For brevity, we present the results here for only two of the deformation algorithms to illustrate the potential differences.[8]

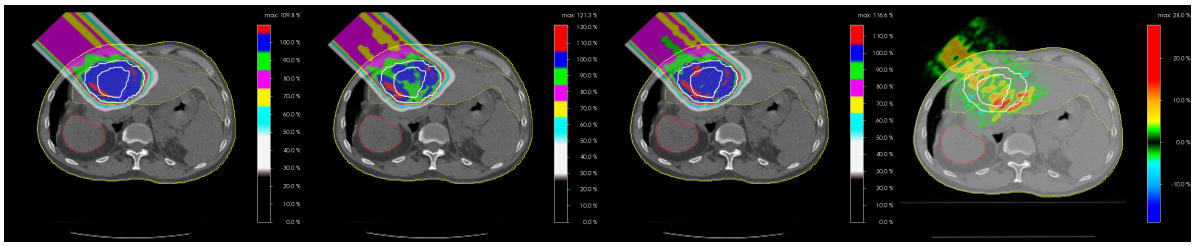

a. nominal *b-1. single scanning (ADW)* *b-2. single scanning (BW)* *b-3. difference for single scanning*

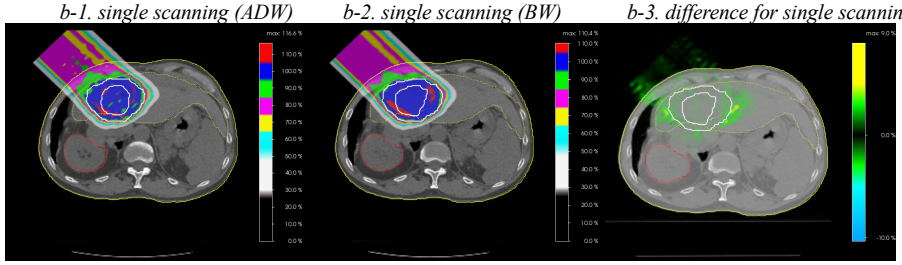

c-1. x8 rescanning (ADW) *c-2.x8 rescanning (BW)* *c-3.difference for x8 rescanning*

Fig. 3 Influence of different motion estimations to 4D dose calculation

Finally, the DVH curves in *Fig. 4*, show that the influences from different motion estimations are quite significant, if a single scanning approach is used. In this scenario, the local dose differences between two estimated motions could be as high as 28% with the majority of points showing differences of 10% or more. However, when the rescanning technique is applied, the local dose difference is reduced to a maximum of 10%, with most differences reducing to 2%.

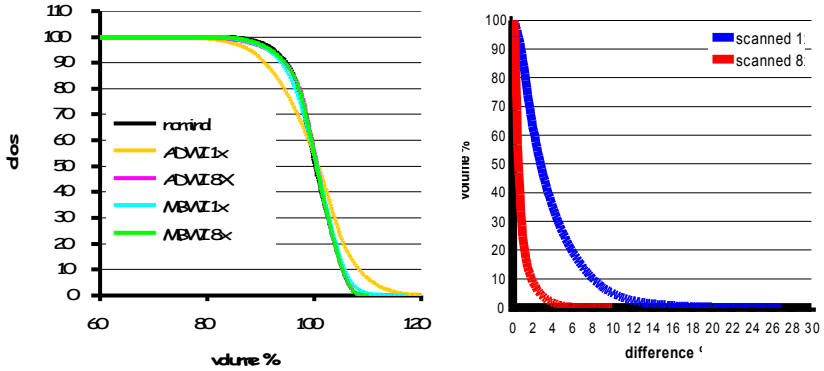

Fig. 4 Dose-Volume Histogram and Difference of DVH for different motion scenarios

Discussion

I. For the liver motion estimation.

Firstly, the results indicate that for CT images of liver, registration accuracy can not be further improved by using the target mask option. Since the images generally have small gradients, the information from outside of the target region probably favors the registration performance. Secondly, the Demons model is best combined with an Affine transformation as initial alignment. In addition, the standard deviation in the Gaussian Filter used for regularization has a great influence on the final motion estimation, therefore the value should be chosen properly, especially for 4D dose calculation. Thirdly, the performance of the B-Splines model is seriously dependent on the presence of the landmarks, so this algorithm also should be used carefully, especially when the images are acquired without pre-implanted markers.

II. For the influences to 4D dose calculation.

We have shown that different registration methods can provide quite different motion estimations. Even for the methods which shared a similar error level, the deformation fields are still distinct from each other. How seriously the registration method influences the 4D dose calculation and how much the registration accuracy contributes to the correct dose calculation are still open questions and should be analyzed further.

Our preliminary results show however that the influence from the different motion estimations on our 4D dose calculation is quite significant if single scanning approach is used, but become relatively small when rescanning is applied. Based on our calculations, the rescanning technique seems to be insensitive to motion estimations, but more cases should be studied further before addressing this conclusion.

III. Limitation and future work

For the low contrast CT images in the abdominal region, more information from the original images need to be obtained to improve deformable registration performance and to decrease registration error. The images from 4DCT with a contrast agent could be one of the best solutions, but potential problem might be raised from non-synchronized contrast injection during the long image acquisition process. The spectrum or dual energy CT could provide better soft tissue resolution, and more detailed structure could be distinguished directly from the image, but the feasibility still needs to be further evaluated. Additionally, the image pre-processing by using contrast enhancement technique might be also worthy of looking into.

References

[1] Pedroni et. al. The 200 MeV proton therapy project at the PSI: Conceptual design and practical realization. *Med Phys,* **1995***, 22(1)*, 37-53

[2] Pedroni et. al. The PSI Gantry 2: a second generation proton scanning gantry. *Z Med Phys.,* **2004***, 14(1)*, 25-34

[3] Lomax et. al. Treatment planning and verification of proton therapy using spot scanning: Initial experiences. *Med Phys,* **2004***, 31(11)*, 3150-7

[4] Lomax et. al. Intensity modulated proton therapy: A clinical example. *Med Phys,* **2001***, 28 (3)*, 317-324

[5] Phillips et. al. Effects of respiratory motion on dose uniformity with a charged particle scanning method. *Phys Med Biol.,* **1992***, 37*, 223-234

[6] Lambert et. al. Intrafractional motion during proton beam scanning. *Phys Med Biol,* **2005***, 50(20)*, 4832-62

[7] Thirion. Image matching as a diffusion process: an analogy with Maxwell's demons. *Med Image Anal.,* **1998***, 2(3)*, 243-60

[8] Zhang, Y. Respiratory liver motion extraction for proton therapy - deformable registration from 4DCT. Master Thesis 2010:66, *Kungliga Tekniska Högskolan, Stockholm,* **2010**

4D dose calculation on a deforming dose grid for scanned proton beams and target volume definition taking into account motion and proton range variations

D. Boye[1,2], A. J. Lomax[1,2], A. Knopf[1]
[1]Center for Proton Therapy, Paul Scherrer Institut, 5232 Villigen-PSI, Switzerland
[2]ETH, Zürich, Switzerland

Abstract

Purpose: The Center for Proton Therapy at Paul Scherrer Institut (PSI) is treating cancer patients with an active spot scanning technique. So far only static targets are treated, since moving target sites lead to interplay effects causing inhomogeneous dose distributions. However, a second generation proton scanning Gantry, which is optimized to treat moving targets, is currently under construction at PSI. Thus, the treatment of moving target sites is an ongoing project at PSI. We propose a new method for time resolved (4D) dose calculations using a deforming dose grid. In addition we investigate a way to generate target volumes that optimally preserve dose coverage in moving and deforming geometries.

Methods and Materials: The analytical dose calculation at PSI is capable of simulating each spot individually. Depending on gantry properties proton beam spots are delivered in a specific order and timeline. Dose calculation is done per spot on a grid of points (dose grid). According to the timestamp of each proton beam a displacement and a change in radiological depth is applied to the dose grid points in order to take into account movements and deformations of the patient geometry. A tool was developed that automatically generates appropriate target volumes in the incident of motion.

Results: Our advanced 4D dose calculation could reproduce the expected interplay pattern due to motion. Furthermore anticipated target dose misses due to density changes in the beam path were reflected in the calculated dose distributions.

Conclusion: It was shown that the use of a deforming dose grid is a feasible alternative to the common approach of warping time resolved dose distributions to a reference phase. Advanced 4D proton dose calculations emphasize the necessity to use appropriate target volumes. We showed that the employment of the proposed range adapted volumes assured target dose coverage in the incident of motion and deformation.

1 Introduction

1.1 Organ motion and 4D treatment planning

Up to date only stationary targets have been treated with scanned proton beams at PSI. With an active spot scanning technique the motion of the beam will interfere with the motion inside the patient leading to so called interplay effects resulting in hot and cold spots in the dose distribution [Philips_1992], [Lambert_2005], [Bert_2008], [Seco_2009]. Furthermore deforming geometries can lead to target dose misses due to density changes in the beam path [Engelsman_2006]. To overcome interplay effects it is planned to implement a rescanning approach at the new gantry at PSI [Pedroni_2004], [Zenklusen_2010]. Techniques proposed by other groups include gating [Lu_2007] and tracking [Groezinger_2008]. Target dose misses due to changing proton ranges can be compensated by defining internal target volumes (ITVs). Margin definition in geometrical units as well as approaches incorporating the dependence of the dose on the density variations have been discussed [Engelsmann_2006], [Bert_2007], [Rietzel_2010].
A treatment planning system which is capable of incorporating target motion is essential to all approaches. Current treatment planning systems calculate dose on individual phases of a 4D-CT and warp each sub-dose distribution back to the reference image by image registration [Rietzel_2005], [Bert_2007].

1.2 Current 3D dose calculation at PSI

The dose calculation in the treatment planning system of PSI is based on a ray casting pencil beam model [Schaffner_1999]. First a dose grid is created covering a volume where all deposited dose is included. The planning system then calculates the dose for each applied proton beam in all dose grid points. Dose deposited at (s,t,u) in gantry coordinate system by a pencil beam with central-axis in s-direction and positioned at (t0,u0) is given by

$$D(s,t,u) = N_{p+}\mathrm{ID}(\mathrm{wer})\frac{1}{2\pi\sigma_t\sigma_u}\exp\left[-\frac{(t_0-t)^2}{2\sigma_t^2}\right]\exp\left[-\frac{(u_0-u)^2}{2\sigma_u^2}\right] \quad (1)$$

Np+: number of protons in the beam spot
ID: integral dose, interpolated from depth-dose lookup table
wer: total water equivalent range including range shifter plates at grid point (s,t,u)
sigma_i: standard deviations of the Gaussians of the pencil beam in t and u directions at a water equivalent range equal to that of the grid point at (s,t,u), including all contributions to beam width (inital phase space, multiple coloumb scattering in the patient and range shifter and its propagation in the air gap between range shifter and patient.

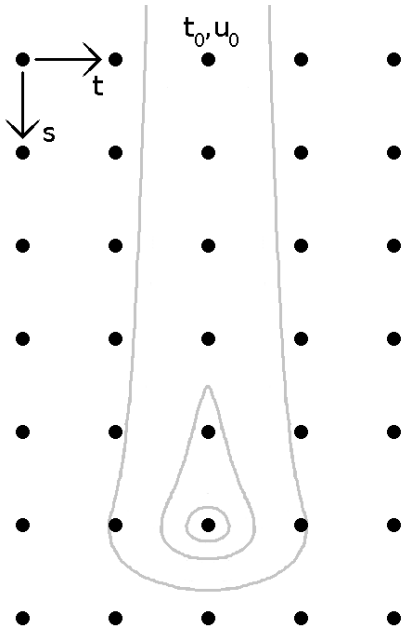

Figure 1 - Dose grid in (s,t) plane

Overall dose in one grid point is given by the sum over all spots. To create a continuous dose distribution the dose in between the dose grid points is interpolated.

2 Methods and Materials

2.1 Dose calculation on a deforming dose grid

The starting point for the 4D dose calculations is a standard static 3D treatment plan of our in house developed treatment planning system. From the 3D dose calculation results a proton spot list. In a second step an individual timestamp is calculated for each pencil beam of the proton spot list. This timestamp depends on the dose delivered at each position and a set of hardware parameters one has to choose. The timestamps will for example change depending on the scanning path and velocity (required dead times to adjust the beam position) and, if applied, the kind of rescanning (2D/3D, scaled/iso-layered, number of rescans). Motion and deformations resulting in density changes can be taken into account by displacement- and density-variation-maps at each time instance during the treatment delivery. The spotlist from the 3D calculation together with the list of timestamps, the displacement-maps and the density-variation-maps are then the input for the 4D dose calculation.
Each dose grid point is associated with a position in (s,t,u) and a water equivalent range (wer). Equation (1) shows that the dose calculation in a point depends only on the distance to the central axis of the beam (t0-t),(u0-u) and the water equivalent range. The 4D code calculates each spot individually and changes the position and the water equivalent range of the dose grid points according to the timestamp of the spot and the corresponding displacement- and the density-variation-map. This results in an accumulation of the dose throughout all motion phases. Dose of a single spot in (s,t,u) at timestamp TS is given by

$$D_{TS}(s,t,u) = N_{p^+}\mathrm{ID}(\mathrm{wer}_{TS})\frac{1}{2\pi\sigma_t\sigma_u}\exp\left[-\frac{(t_0-(t+\Delta t_{TS}))^2}{2\sigma_t^2}\right]\exp\left[-\frac{(u_0-(u+\Delta u_{TS}))^2}{2\sigma_u^2}\right] \qquad (2)$$

wer_TS: timestamp-dependent water equivalent range
Delta i_TS: displacement of dose grid point in i=t,u at timestamp TS

2.2 Simulations with simple CT phantoms

Two simple virtual CT phantoms were created for simulations.

CT phantom I, shown in figure 2, contained only a box of water with a spherical target volume definition inside the box. Displacement-maps to move the target were created. With a period of 5s the target was moved from the left to the right and back, imitating a breathing cycle.

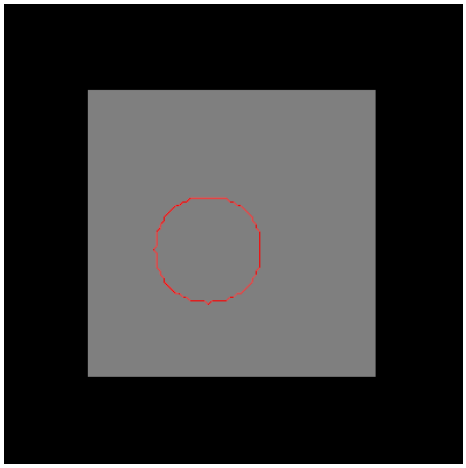

Figure 2 - CT phantom I (red contour: target volume)

CT phantom II, shown in Figure 3, contained a spherical target volume (HU=1200) in water. The beam direction was chosen from the top and upstream of the target an obstacle (HU=1100) with a cylindrical high density area (HU=2500) was placed.

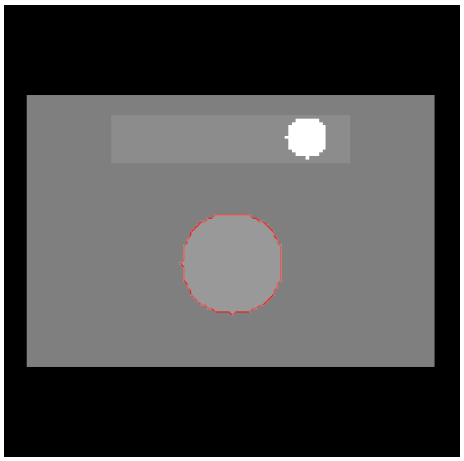

Figure 3 - CT phantom II (red contour: target volume)

To move the obstacle in front of the target, displacement-maps for the upstream area were created. The obstacle was moved from the right to the left and back with a period of 5s.
Deformed CT images corresponding to the displacement-maps of each time step were simulated using image warping classes from the Insight Segmentation and Registration Toolkit (ITK) [Yoo_2002]. On the basis of these deformed CT images the radiological path (here water equivalent range) of each dose grid point for each time instance was derived with Siddon's algorithm [Siddon_1985]. The displacement –maps together with the resulting density-variation maps for each dose grid point at each time instance were then used in the 4D dose calculation.

2.3 Target contour adaption due to proton range variations

Advanced 4D dose calculations show that in the incidence of motion it is not sufficient to use simple target contours defined on one reference 3D CT image. The target contours have to be adapted accounting for proton range variations during the course of treatment.
A tool was programmed using the Visualization Toolkit (VTK) (http://www.vtk.org) and ITK [Yoo_2002] to automatically create adapted margins. Inputs are a 3D reference CT image, the original target contour on the reference image and a set of displacement-maps.
For each time step a deformed CT image based on the corresponding displacement-map is calculated. Deformed CT images for our CT phantom II are shown in Figure 3. While the target remains static in these time resolved CT images, the upstream area with the obstacle moves from the right to the left and back. For each time step the water equivalent range of each contour point C_i for a chosen beam direction is calculated based on the time resolved deformed CT images. Back on the reference image the calculated water equivalent ranges won't be necessarily at the same positions C_i. On a ray in beam direction through C_i it is then searched for the point with the same water equivalent range on the reference image. The original contour points are then moved to these calculated positions resulting in an adapted margin for each time step. The overall adjusted margin (red contours in Figure 4) is generated by adding up the adapted margins of each time step (blue contours in Figure 4).

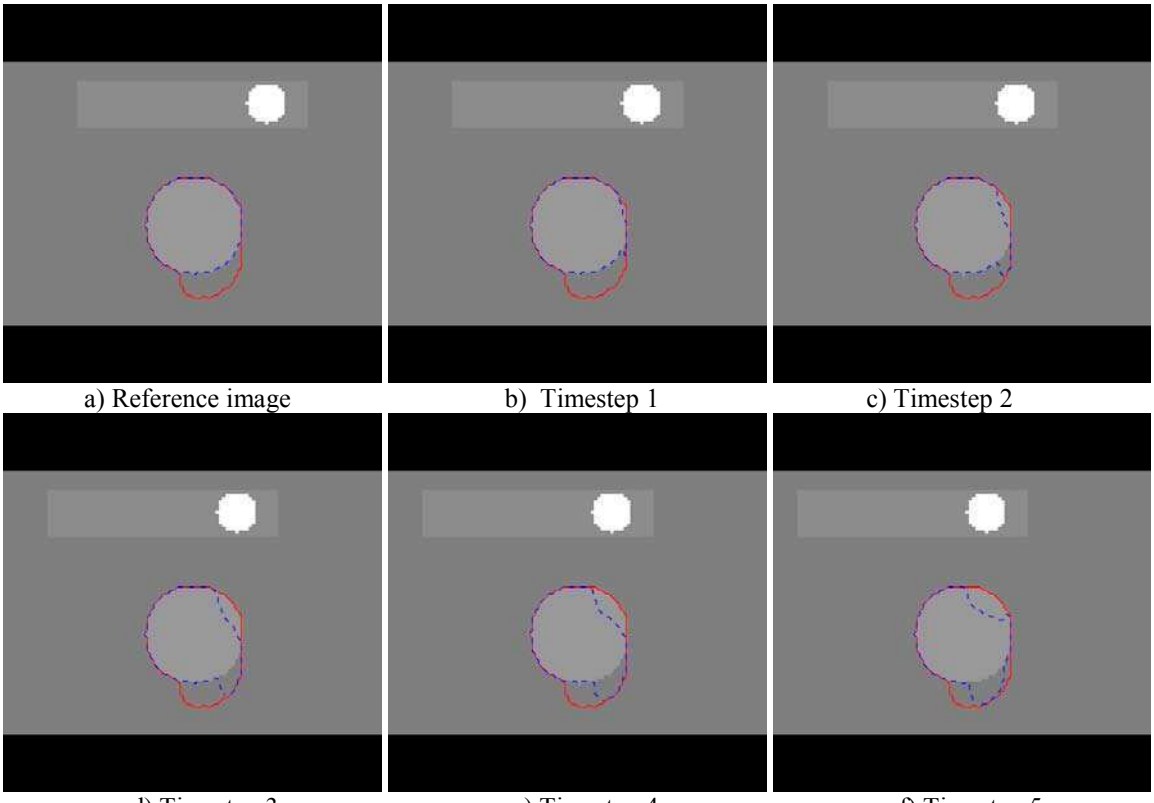

a) Reference image b) Timestep 1 c) Timestep 2

d) Timestep 3 e) Timestep 4 f) Timestep 5

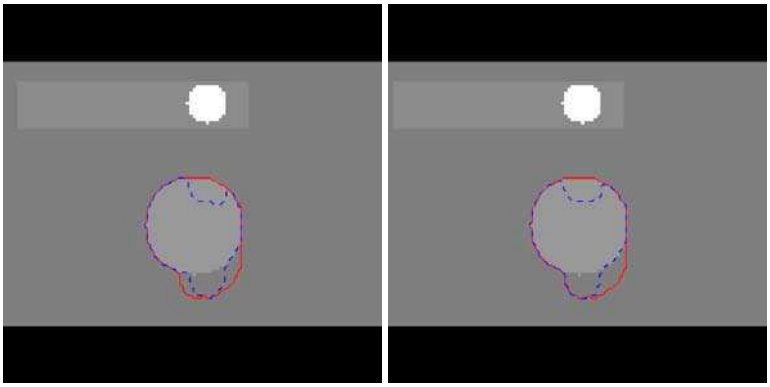

g) Timestep 6 h) Timestep 7

Figure 4 a) - h) - Adapted margin for each time step (dashed blue line) and the successive resulting overall adjusted margin (solid red line)

3 Results

3.1 Interplay effects and target misses

As a first test of the new 4D dose calculation it was checked if interplay effects due to target motion and target misses due to density changes could be produced. In Figure 5 the expected interplay patterns within the target volume are clearly visible. Those patterns depend on correlation of beam and target motion.

In the second simulation with CT phantom II the target itself did not move but the density in front of it was changed. Figure 6 shows that there were, as expected, not only interplay effects but also target misses in the lower right corner of the target.

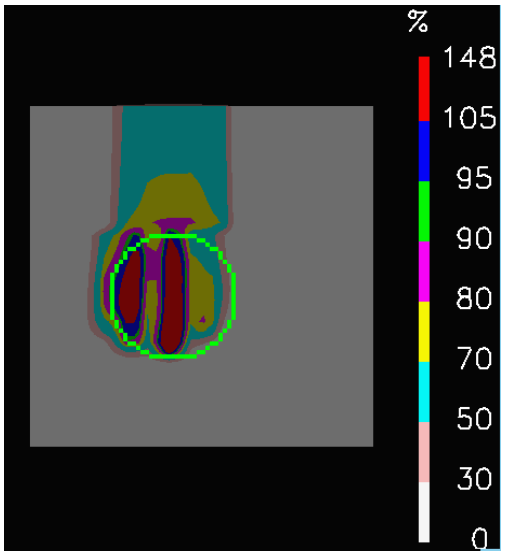

Figure 5 - Interplay effects due to motion of target volume

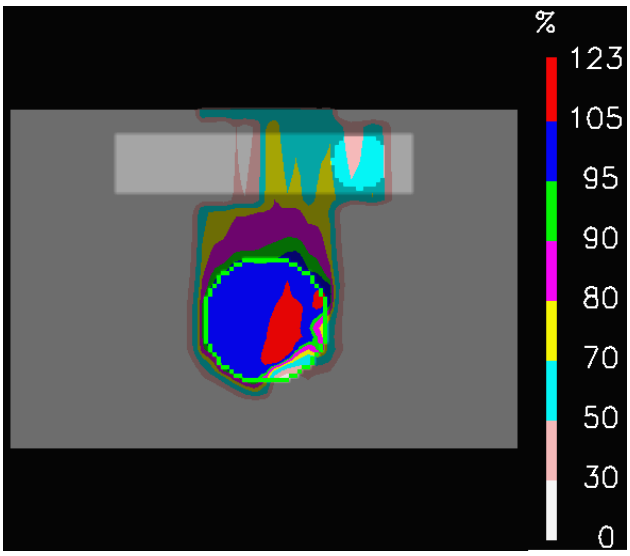

Figure 6 - Interplay effects and target misses due to density changes in front of target volume

3.2 Rescanning approach

To simulate rescanning the plan was applied multiple times. Following the scaled rescanning approach, the dose per rescan was divided by the number of rescans. New timestamp files incorporating a rescanning of eight times were generated for our previous simulations.
First, rescanning was applied to the non-adapted margins (figures 7+8). Interplay effects resulting in large dose inhomogeneities are no longer visible.

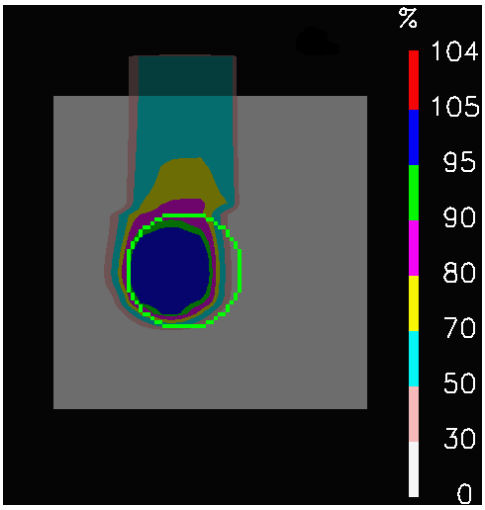

Figure 7 - rescanning non-adapted target 8x times in CT phantom I

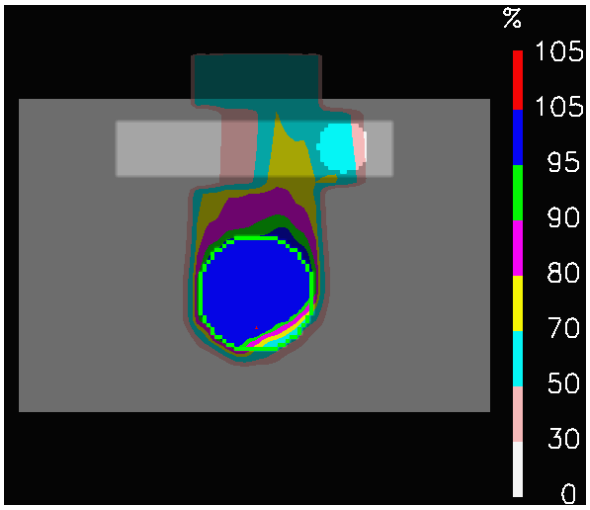

Figure 8 - rescanning on non-adapted target 8x times in CT phantom II

As a next step rescanning on the adapted target margins was performed. Results are shown in figures 9 and 10. In both cases the rescanning of the adapted margins achieved target dose coverage.

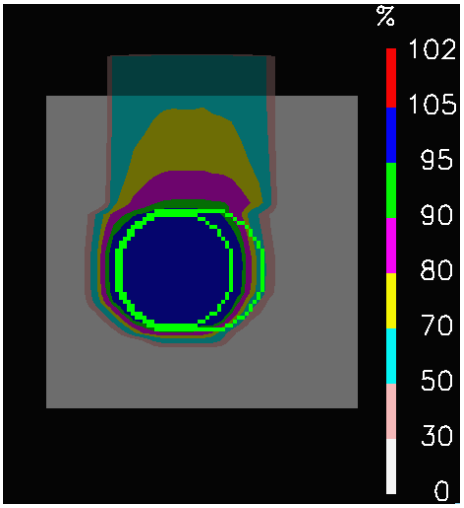

Figure 9 - rescanning adapted target 8x times in CT phantom I

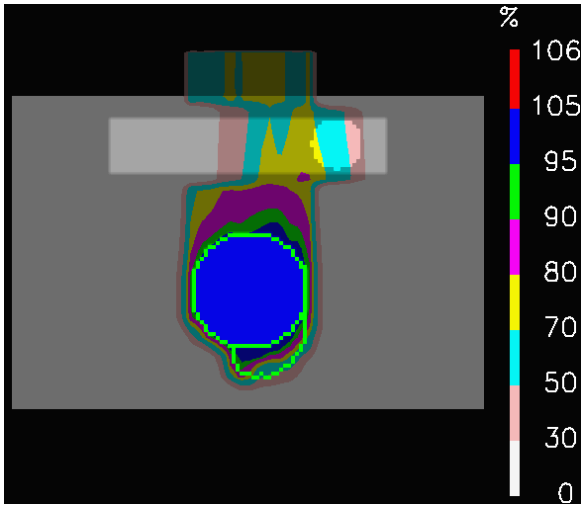

Figure 10 - rescanning adapted target 8x times in CT phantom II

4 Discussion

4.1 Uncertainties in dose calculation

One has to be aware that discontinuities in the displacement-maps (e.g. sliding organ boundaries) will lead to dosimetric errors for positions in between dose grid points. This is because the dose at these positions is interpolated on the reference dose grid. Decreasing the dose grid spacing will minimize this uncertainty. Sliding organ boundaries resulting in discontinuous displacement-maps are subject of current research in image registration [Ruan_2009]. Typical smooth image registration methods (e.g. B-spline or Demons) will not generate correct displacement fields in the presence of sliding boundaries.
An other uncertainty in our 4D dose calculation is the change of total integral dose if a high density area moves in or out of the area where dose is delivered. This is due to the fact that the dose in each dose grid point is calculated as dose to water. Other 4D dose calculations will have the same problems if they use an algorithm which calculates dose to water.

4.2 Dose optimization with adapted target margins

As seen in figure 10 there is dose of 95 - 105% delivered to the surrounding area of the target. In our approach of creating the motion and density adapted margin there is no weighting of time steps included in the dose optimization. Areas in the extension of the target volume are not occupied equally throughout the breathing cycles. To reduce the dose to the surrounding area it is necessary to incorporate the motion and density changes also into the dose optimization in a way similar to the motion-weighted DVHs proposed by Zhang et al. [Zhang_2009].

4.3 Real patient geometries

In this study the effect of motion and deformation has only been studied in simplified phantom geometries. In realistic patient geometries dose inhomogeneities will most likely blur out during the treatment course of several fractions, if the motion amplitude is smaller then 5 mm, a random motion phase is assured at each fraction and sufficient rescans are applied. However, to correctly estimate target dose misses due to density changes advanced 4D calculations like performed in this study are essential. These target dose misses can not be compensated by motion management techniques like gating or rescanning. Target dose coverage for these techniques can only be assured by specific margin recepies, like the one proposed in this study, that are adequate for the high sensitivity of the dose distribution towards density variations in the entrance channel.

5 Conclusion

We have demonstrated the feasibility of 4D dose calculations using a deforming dose grid. It was shown that it is necessary to adapt the target volume to incorporate density changes and motion if target dose coverage is to be achieved.

References:

[Bert_2007]
Bert, C and Rietzel, E
4D treatment planning for scanned ion beams
Radiation Oncology, 2007, 2
doi: 10.1186/1748-717X-2-24

[Bert_2008]
Bert, C and Groezinger, S O and Rietzel, E
Quantification of interplay effects of scanned particle beams and moving targets
Physics in Medicine and Biology, 2008, 53, 2253-2265
doi: 10.1088/0031-9155/53/9/003

[Engelsman_2006]
Engelsman, M and Rietzel, E and Kooy, H M
Four-dimensional proton treatment planning for lung tumors
International Journal of Radiation Oncology*Biology*Physics, 2006, 64, 1589-1595
doi: 10.1016/j.ijrobp.2005.12.026

[Groezinger_2008]
Grözinger, S O and Bert, C and Haberer, T and Kraft, G and Rietzel, E
Motion compensation with a scanned ion beam: a technical feasibility study
Radiation Oncology, 2008, 3
doi: 10.1186/1748-717X-3-34

[Lambert_2005]
Lambert, J and Suchowerska, N and McKenzie, D R and Jackson, M
Intrafractional motion during proton beam scanning
Physics in Medicine and Biology, 2005, 50, 4853-4862
doi: 10.1088/0031-9155/50/20/008

[Lu_2007]
Lu, H-M and Brett, R and Sharp, G and Safai, S and Jiang, S and Flanz, J and Kooy, H
A respiratory-gated treatment system for proton therapy
Medical Physics, 2007, 34, 3273 - 3278
doi: 10.1118/1.2756602

[Phillips_1992]
Phillips, M H and Pedroni, E and Blattmann, H and Boehringer, T and Coray, A and Scheib, S
Effects of respiratory motion on dose uniformity with a charged particle scanning method
Physics in Medicine and Biology, 1992, 37, 223 - 234
doi: 10.1088/0031-9155/37/1/016

[Rietzel_2005]
Rietzel, Eike and Chen, George T Y and Choi, Noah C and Willet, Christopher G
Four-dimensional image-based treatment planning: Target volume segmentation and dose calculation in the presence of respiratory motion
International Journal of Radiation OncologyBiologyPhysics, 2005, 61, 1535 - 1550
doi: 10.1016/j.ijrobp.2004.11.037

[Rietzel_2010]
Rietzel, E and Bert, C
Respiratory motion management in particle therapy
Medical Physics, 37, 2010, 449 - 460
doi: 10.1118/1.3250856

[Ruan_2009]
Ruan, D and Selim Esedoglu, S and Fessler, J A
Discriminative sliding preserving regularization in medical image registration
ISBI'09 Proceedings of the Sixth IEEE international conference on Symposium on Biomedical Imaging: From Nano to Macro, p. 430 - 433, IEEE Press Piscataway, NJ, USA, 2009, ISBN: 978-1-4244-3931-7

[Schaffner_1999]
Schaffner, B and Pedroni, E and Lomax, A
Dose calculation models for proton treatment planning using a dynamic beam delivery system: an attempt to include density heterogeneity effects in the analytical dose calculation
Physics in Medicine and Biology, 1999, 44, 27 - 41
doi: 10.1088/0031-9155/44/1/004

[Seco_2009]
Seco, J and Robertson, D and Trofimov, A and Paganetti, H
Breathing interplay effects during proton beam scanning: simulation and statistical analysis
Physics in Medicine and Biology, 2009, 54, N283 - N294
doi: 10.1088/0031-9155/54/14/N01

[Siddon_1985]
Siddon, R L
Fast calculation of the exact radiological path for a three-dimensional CT array
Medical Physics, 1985, 12, 252 - 255
doi: 10.1118/1.595715

[vonSiebenthal_2007a]
Von Siebenthal, M and Székely, G and Gamper, U and Boesiger, P and Lomax, A and Cattin, Ph
4D MR imaging of respiratory organ motion and its variability.
Physics in medicine and biology, {2007}, {52}, 1547 - 1564
doi: 10.1088/0031-9155/52/6/001

[Yoo_2002]
Yoo, T S and Ackerman, M J and Lorensen, W E and Schroeder, W and Chalana, V and Aylward, S and Metaxas, D and Whitaker, R
Engineering and algorithm design for an image processing Api: a technical report on ITK - the Insight Toolkit
Stud Health Technol Inform, 2002, 85, 586 - 592
url: http://www.itk.org

[Zenklusen_2010]
Zenklusen, S
A study on repainting strategies for treating moderately moving targets with proton pencil beam scanning at the new Gantry 2 at PSI
submitted to Physics in Medicine and Biology, July 2010

[Zhang_2009]
Zhang, G G and Feygelman, V and Stevens, C. and Li, W and Dilling, T
Motion-Weighted Dose-Volume Histograms – A Novel Approach to 4D Treatment Planning
IFMBE Proceedings, 2009, 25, 904 - 907
doi: 10.1007/978-3-642-03474-9_254

[Zhang_2010]
Zhang, Y
Respiratory liver motion extraction for Proton Therapy from 4D CT by deformable registration
Master thesis done at Paul Scherrer Insitut for the Royal Institute of Technology (KTH), School of Technology and Health, Stockholm

Advances in multimodality molecular imaging

H. Zaidi[1,2]
[1] Geneva University Hospital, Division of Nuclear Medicine, CH-1211 Geneva, Switzerland
[2] Geneva University, Geneva Neuroscience Center, CH-1211 Geneva, Switzerland
mail: habib.zaidi@hcuge.ch

Introduction

Advances in genomics, proteomics and technology are changing the practice of medicine in a profound way. Molecular imaging allows for the study of molecular and cellular events in the living intact organism [1]. Positron emission tomography (PET) is a highly sensitive non-invasive technology that is ideally suited for pre-clinical and clinical imaging of cancer biology, in contrast to anatomical approaches (CT and MRI). The historical development of PET is marked by numerous significant technological accomplishments driven by an unprecedented collaboration between multi-disciplinary groups of investigators with backgrounds in medical sciences, physics, chemistry, mathematics, bioengineering, and computer science [2]. Multimodality image registration and fusion plays a key role in clinical management of patients in routine diagnosis, staging, restaging and assessment of response to treatment, surgery and radiation therapy planning of malignant diseases. The complementarity between anatomical (CT and MRI) and molecular (SPECT and PET) imaging modalities is now well established and the role of fusion imaging widely recognized as a central piece of the general tree of clinical decision making [3].

Moreover, dual-modality imaging technologies including SPECT-CT, PET-CT and in the near future PET-MR now represent the leading component of any modern healthcare institution [4]. This paper also reflects the tremendous increase in interest in quantitative molecular imaging using PET as both clinical and research imaging modality in the past decade [5]. It offers a brief overview of the entire range of PET imaging from basic principles to various steps required for obtaining quantitatively accurate data from dedicated standalone PET and combined PET-CT (and PET-MR) systems. Impact of physical degrading factors including attenuation of photons and contribution from photons scattered in the patient and partial volume effect on the diagnostic quality and quantitative accuracy of PET data is outside the scope of this paper and will not be discussed here. The development of new probes and challenges to target tumour hypoxia in clinical oncology will also be addressed.

Novel tracers and tumour hypoxia

Recent advances in the development of novel tracers targeted to other aspects of tumour biology, including cell growth, cell death, oncogene expression, drug delivery, and tumour hypoxia will significantly enhance the capability of clinical scientists to differentiate tumours and are likely to be used to guide treatment decisions. Several new tracers are expected to be approved and routinely used in the coming years. Obviously, the list of new tracers having the potential for routine use in the near future is very long and will not be reviewed here. Interested readers may consult recently published reviews addressing this topic [6-8]. In certain cancers, ^{18}F-labeled fluorothymidine (FLT) may prove to be of value in monitoring response to therapy instead of FDG [9]. This tracer, however, does not appear optimal for diagnostic purposes since it is insensitive for detecting slow growing tumours. ^{18}F-labeled DOPA [10] along with ^{68}Ga-labeled DOTA octreotide [11] and ^{124}I-labeled MIBG [12] appear to have the promise of improving the management of patients with neuro-endocrine tumours. Peptides containing amino acid sequence arginine-glycine-aspartate (RGD) appear to have an affinity toward integrins that are present on activated endothelial cells in tumours with angiogenesis [13]. ^{18}F-Galacto-RGD is a tracer developed for specific imaging of {alpha}v{beta}3 expression, a receptor involved in angiogenesis and metastasis that proved to be particularly useful in patients with squamous cell carcinoma of the head and neck [14]. Estrogen receptor (ER) targeting agents may be used to assess non-invasively, the ER section of tumours *in vivo* by ^{18}F-labeled estrogen analogues such as Fluoestradiol (FES) [15]. Angiogenesis, the formation of new vessels is the target of a multitude of novel therapies and drugs. Therefore, direct visualization of this biologic response to tumour hypoxia and cell proliferation will be of great importance in developing these drugs. Peptides containing amino acid sequence arginine-glycine-aspartate (RGD) appear to have an affinity toward integrins that are

present on activated endothelial cells in tumours with angiogenesis [13] Apoptosis or programmed cell death can be imaged with radiolabeled Annex V to monitor response to therapy in cancer [16].

Agents that measure regional hypoxia in malignant tumours (e.g. FMISO, EF5, ^{64}Cu-ATSM) and possibly in some benign disorders will be frequently employed [17] especially in the context of radiation therapy treatment planning [18]. Tissue hypoxia is a pathological condition in which a region of the body is deprived of adequate oxygen supply, and is a major constraint for tumour treatment by radiotherapy. The efficacy of ionizing radiation directly relies on adequate supply of oxygen to the targeted tumour. As a tumour grows, it needs oxygen in order to survive. Although the tumour develops new blood vessels by a process of angiogenesis, these new vessels are typically less extensive than in normal tissues. As a result, the tumour cells do not receive adequate oxygen from the blood, leading to hypoxia and leaving portions of the tumour with regions where the oxygen concentration is significantly lower than in healthy tissues. Hypoxic tumour cells are usually resistant to radiotherapy and chemotherapy, but they can be made more susceptible to treatment by increasing the amount of oxygen in them. Furthermore, hypoxia is related to malignant progression, increased invasion, angiogenesis and an increased risk of metastases formation [19]. There are three distinct types of tumour hypoxia: [20] (i) perfusion related (acute) hypoxia which results from inadequate blood flow in tumours; it is generally the consequence of recognized structural and functional abnormalities of the tumour neovasculature; (ii) diffusion related (chronic) hypoxia caused by increased oxygen diffusion distances due to tumour expansion; and (iii) anaemic hypoxia related to the reduced O_2-carrying capacity of the blood.

Two different strategies can be used to overcome the problem of hypoxia-mediated radioresistance. The first strategy is to improve the tumour oxygenation during radiotherapy. The second strategy is to target hypoxia as a relatively unique feature of tumour tissue by means of drugs, which are activated under hypoxic conditions and act as hypoxic radiosensitizers or hypoxic cytotoxins [19].

^{18}F-MISO and Cu-ATSM are the most widely used tracers in PET for their ability to demonstrate heterogeneity and general availability [21]. ^{18}F-MISO has relatively slow blood clearance and high lipophilicity contributing to significant background activity and relatively low contrast between hypoxic and normal tissues [22]. One remedy to this was to acquire a venous blood sample during the course of the imaging procedure for a tumour/blood ratio image to improve the contrast. ^{18}F-MISO is able to monitor the changing hypoxia status of lung tumours during radiotherapy [23]. Studies in sarcoma [24] and head and neck cancer [24,25] have demonstrated a correlation of ^{18}F-MISO uptake with poor outcome to radiation and chemotherapy.

Cu-ATSM is another promising agent for delineating the extent of hypoxia within tumours. Most Cu-ATSM studies have used the short-lived ^{60}Cu (half-life of 0.395 h), which requires an on-site cyclotron. One advantage of using shorter-lived ^{60}Cu is the ability to perform multiple imaging sessions in a short time frame. To enable the transport of Cu-ATSM to the PET facilities without a cyclotron, longer-lived ^{61}Cu (half-life of 3.408 h) and ^{64}Cu (half-life of 12.7 h) are alternatives. Numerous pre-clinical studies have validated its use for imaging of hypoxia in tumours and other tissues. One concern with using Cu-ATSM to delineate hypoxia was that it may be tumour-dependent, and cell-line dependent. It was demonstrated that there was variation in the ^{64}Cu-ATSM cellular accumulation, with uptake in normoxic cells being anywhere from two to nice times lower than that in hypoxic cells, depending upon the cell line. Nonetheless, ^{64}Cu-ATSM has been shown to be highly correlated with ^{18}F-FMISO in an animal model [26]. In human studies of lung [27] and cervical cancers [28,29], that ^{60}Cu-ATSM can act as a prognostic indicator for response to therapy. In a prospective study of 14 patients with non-small cell lung cancer, a semi-quantitative analysis of the ^{60}Cu-ATSM tumour-to-muscle ratio was able to discriminate those likely to respond to therapy from non-responders [30]. A similar study in 14 women with cervical cancer demonstrated a similar predictive value in the tumour response to therapy. In the same study, tumour ^{18}F-FDG uptake did not correlate with ^{60}Cu-ATSM and there was no significant difference in tumour ^{18}F-FDG uptake between patients with hypoxic tumours and those with normoxic tumours [30] ^{18}F-EF5 is another promising agent [31,32] which proved to be useful for non-invasive clinical assessment of hypoxia in brain tumours [33].

Advances in hybrid PET-CT instrumentation

The historical development of multimodality imaging is marked by various significant technical and scientific accomplishments driven by an unprecedented collaboration between multi-disciplinary groups of investigators. Even though the introduction of commercial PET-CT units in a clinical setting is a recent feature, the prospective benefits of correlative multimodality imaging are well established since the early years of medical imaging. Many pioneering radiological scientists and physicians recognized that the capabilities of a radionuclide imaging system could be improved by adding an external source to allow acquisition of transmission data for anatomical correlation of the emission image [3]. Interestingly, the derived theoretical concepts that were occasionally patented [34,35] never materialized in practice until late Dr. Bruce Hasegawa and colleagues (University of California, San Francisco) pioneered in the 1990s the development of dedicated SPECT-CT [36,37]. Thus, Dr. Hasegawa is the person to credit for the conception and design of the first combined SPECT-CT unit and this stands for a wonderful tribute to his memory [38]. Later, Dr. Townsend and co-workers (University of Pittsburgh) pioneered in 1998 the development of combined PET-CT imaging systems, which have the capability to record both PET emission and x-ray transmission data for correlated functional/structural imaging [39,40]. More compact and cost-effective designs of dual-modality systems have been explored more recently. One such approach uses a rail-with-sliding-bed design where a sliding CT bed is placed on a track in the floor and linked to a flexible SPECT camera [41]. A variety of rail-based, docking and click-over concepts for correlating functional and anatomical images are also being considered with the aim to offer a more economic approach to multimodality imaging for institutions with limited resources [42].

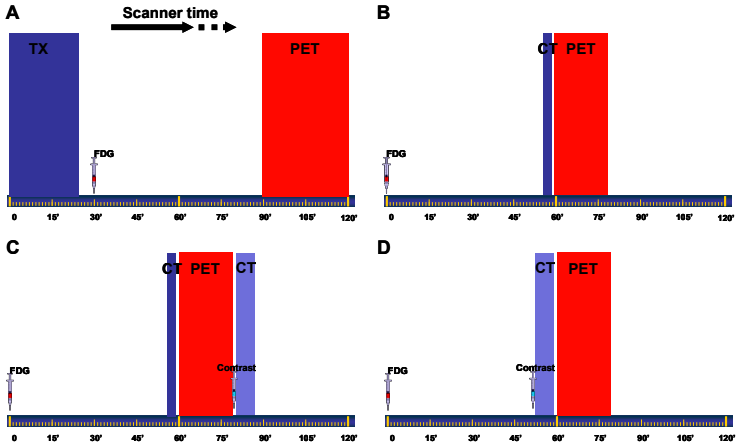

Figure 1. Timeline for various stand-alone PET and PET-CT scanning protocols following tracer injection and typical 1 hour waiting time for ^{18}F-FDG. The pre-injection transmission scan required on conventional standalone PET scanners (~ 3 min per bed position on full-ring systems) is usually acquired prior to tracer injection (**A**). On modern combined PET-CT scanners equipped with fast detectors, the acquisition time is practically half the time required on conventional detectors. Either only a low dose CT for attenuation correction (**B**) or combined with a diagnostic quality contrast enhanced CT study is usually performed depending on the clinical indication (**C**). The latter can also be used for attenuation correction but might result in artifacts in some cases by overcorrecting for attenuation in regions containing contrast medium (**D**). It should be noted that PET-CT allows to reduce the overall scanning time, thus increasing patient throughput.

Among the many advantages offered by PET-CT is the reduction in the overall scanning time, thus allowing to increase patient throughput by ~30% [43] owing to the use of fast CT-based attenuation correction compared to lengthy procedures involving the use of external transmission rod sources. Figure 1 illustrates the timeline for various stand-alone PET and combined PET-CT scanning protocols following tracer injection and typical 1 hour waiting time for ^{18}F-flurodeoxyglucose (FDG). The patient is prepared for imaging which includes administration with the radiopharmaceutical, typically 370 to 555 MBq (10 to 15 mCi) of ^{18}F-FDG in adults. A pre-injection transmission scan is usually performed on stand-alone PET scanners prior to tracer injection to reduce spillover of emission data into the transmission energy window although post-injection transmission scanning protocols were successfully used in the clinic on modern PET scanners [44]. On combined PET-CT units, the

patient is asked to remove all metal objects that could introduce artefacts in the CT scan and then is positioned on the patient table of the dual/modality imaging system. The patient then undergoes an "overview" or "scout" scan during which x-ray projection data are obtained from the patient to identify the axial extent of the CT and PET study. The patient then undergoes a low-dose spiral CT acquisition followed by the PET study starting approximately 1 hour after FDG administration. The CT and PET data then are reconstructed and registered, with the CT data used for attenuation correction of the reconstructed PET images. Depending on institutions and agreements between clinical department and clinical requirements [45-47], the images might be interpreted in tandem by a radiologist and nuclear medicine physician who can view the CT scan, the PET images, and the fused PET-CT data, followed by preparation of the associated clinical report. Some clinical indications commonly require administration with contrast media to acquire a relatively high-dose diagnostic quality CT scan [48]. The latter can be performed either prior or following the PET study. In the former case, the contrast-enhanced CT is also used to correct the PET data for photon attenuation and the low-dose CT scan is no longer needed. However, care should be taken to avoid hot-spot artefacts in the attenuation corrected PET images that might be caused by overcorrection of radiodense oral and intravenous contrast agents. As a rule of thumb, examination of the uncorrected images is recommended to distinguish technical artefacts from physiologic/pathologic hypermetabolism. Alternatively, post-processing correction methods have been proposed in the literature [49,50].

The promise of PET-MR technology

The interest in PET scanning within strong magnetic fields was first motivated by the need to reduce the distance positrons travel before annihilation (positron range) through magnetic confinement of the emitted positrons [51-53]. Indeed Monte Carlo simulation studies predicted improvements in spatial resolution for high energy positron emitters ranging between 18.5% (2.73 mm instead of 3.35 mm) for ^{68}Ga and 26.8% (2.68 mm instead of 3.66 mm) for ^{82}Rb for a magnetic field strength of 7 Tesla [53]. This is in agreement with results obtained using another Monte Carlo code where a 27% improvement in spatial resolution for a PET scanner incorporating a 10 Tesla magnetic field was reported [54].

It is amazing to point out that the history of combined PET-MR dates back to the mid 1990s even before the advent of PET-CT [52,54,55]. Early attempts to design MR-compatible PET units relied on slight modification of PET detector blocks of a preclinical PET scanner to keep the photomultiplier tubes (PMTs) at a reasonable distance from the strong magnetic field of a clinical MRI unit [56-60]. The detectors were coupled to long optical fibers (4-5 meters), leading the weak scintillation light outside the fringe magnetic field to position-sensitive PMTs. Despite the limitations of this design, similar approaches were adopted by other investigators [61-64]. Other related design concepts based on conventional PMT-based PET detectors rely on more complex magnet designs, including a split magnet [65] or a field-cycled MRI [66].

Other investigators have developed PET-MRI systems configured with suitable solid-state detectors that can be operated within a magnetic field for PET imaging. This includes avalanche photodiodes (APDs) [67] and Geiger-mode avalanche photodiodes (G-APDs) [68,69]. APD-based readout is already implemented on a commercial preclinical PET system, the LabPET™ scanner [70] after about 10 years of the development of the first prototype based on this technology [71]. Various MR-compatible preclinical PET prototypes were designed using both APD-based [72-77] and G-APD based [78-80] technologies. Other promising technologies that might be used for the design of future generation PET-MR systems include amorphous selenium (a-Se) avalanche photodetectors which proved to have an excellent quantum efficiency, a large avalanche gain and a rapid response time [81,82].

Most of the above referenced systems have been tested within a high-field (up to 9.7 T) and proved to produce PET and MR images that appear to be free of distortion, consolidating the hypothesis that there is no significant interference between the two systems and that each modality is virtually invisible to the other [83]. The promising results obtained on preclinical systems encouraged one of the major industrial leading players (Siemens Medical Solutions. Knoxville, TN) to develop the first clinical PET-MR prototype (BrainPET) dedicated for simultaneous brain imaging in collaboration with the University of Tuebingen, Germany [84]. The conceptual design of the integrated PET-MR scanner consists of an isocentric layering of MR head coil, PET detector ring, and MR magnet tunnel. The system is being assessed in a clinical setting by exploiting the full potential of anatomical MRI in

terms of high soft-tissue contrast sensitivity in addition to the many other possibilities offered by this modality including BOLD imaging, functional MRI (fMRI), diffusion-weighted imaging (DWI), perfusion-weighted imaging (PWI), and diffusion tensor imaging (DTI) [85].

On the other hand, the prospective applications of a hypothetical whole-body PET-MR system are being explored in the literature [86-89]. Such a system would allow to exploit, in addition to the above discussed applications, the power of MR spectroscopy (MRS) to measure the regional biochemical content and to assess the metabolic status or the presence of neoplasia and other diseases in specific tissue areas [90].

Until concurrent PET-MR technologies become available for whole body imaging, other approaches for so-called sequential PET-MR imaging have been researched [91]. The Philips GEMINI TF PET-MRI is a hybrid imaging system with Philips time-of-flight GEMINI TF PET and Achieva 3T X-series MRI system, as shown in Figure 2 [92,93]. While this design does not allow simultaneous PET and MRI acquisition, it allows acquisition of automatically co-registered PET and MR images acquired sequentially, similar to the workflow in PET-CT systems. Following initial development, two PET-MRI systems were installed in Mount Sinai Medical Center, NY and Geneva University Hospital, Geneva. Figure 3 shows representative PET-MR and PET-CT images of the same patient acquired sequentially (~60 min time difference) on the two combined systems.

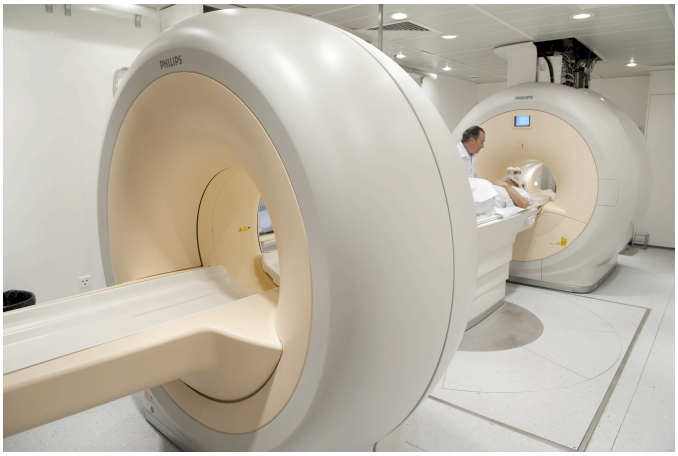

Figure 2. Photograph of the Philips sequential whole-body PET-MRI system design installed at Geneva University Hospital. A turntable patient handling system facilitates patient motion between the 3T MRI system on the left and the time-of-flight PET system on the right.

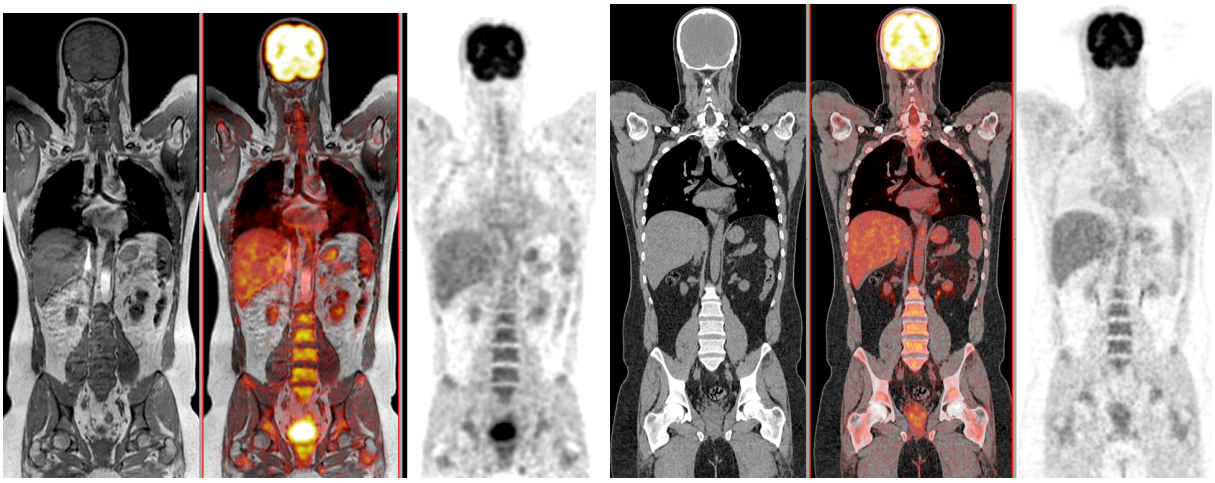

Figure 3. Representative PET-MR and PET-CT images of the same patient acquired sequentially (~60 min time difference) on the two combined systems following injection of 370 MBq of FDG.

Summary

The present paper has attempted to summarize important themes of ongoing advancements by providing an overview of current state-of-the art developments in multimodality molecular imaging combining PET with other structural imaging modalities (PET-CT and PET-MR). There is no doubt that multimodality imaging had changed drastically over the last two decades. The pace of change has accelerated rapidly in the last decade driven by the introduction and widespread acceptance of combined PET-CT units in the clinic and the likely deployment of compact PET-MR systems in the near future. Navigating beyond the 6^{th} dimension is now becoming possible with recent progress in multidimensional and multi-parametric multimodality imaging combining the latest advances in sophisticated software to make use of existing advanced hardware [94]. A controversy arose recently regarding the future role of SPECT in the era of PET [95-98]. Time will determine if these predictions are wrong or will come true. In any case, given that the role of any molecular imaging technology is established with respect to benefits conveyed to patients, dual-modality imaging systems using PET as the key component are here to stay and will definitely maintain an exclusive standing in clinical diagnosis, assessment of response to treatment and delivery of personalized treatments and targeted therapies.

References

[1] S. R. Cherry: Multimodality in vivo imaging systems: twice the power or double the trouble? Annu Rev Biomed Eng **8** (2006) 35-62

[2] M. E. Phelps: PET: the merging of biology and imaging into molecular imaging. J Nucl Med **41** (2000) 661-681

[3] B. Hasegawa, H. Zaidi: Dual-modality imaging: more than the sum of its components. In Quantitative analysis in nuclear medicine imaging. H. Zaidi, Ed. Springer, New York, 2006. 35-81

[4] B. J. Pichler, A. Kolb, T. Nagele, H. P. Schlemmer: PET/MRI: paving the way for the next generation of clinical multimodality imaging applications. J Nucl Med **51** (2010) 333-336

[5] H. Zaidi, M. L. Montandon, A. Alavi: The clinical role of fusion imaging using PET, CT, and MR imaging Magn Reson Imaging Clin N Am **18** (2010) 133-149

[6] R. H. Mach, S. W. Schwarz: Challenges for developing PET tracers: Isotopes, chemistry, and regulatory aspects. PET Clinics **5** (2010) 131-153

[7] J. F. Valliant: A bridge not too far: Linking disciplines through molecular imaging probes. J Nucl Med **51** (2010) 1258-1268

[8] C. J. Anderson, J. W. M. Bulte, K. Chen, et al.: Design of targeted cardiovascular molecular imaging probes. J Nucl Med **51** (2010) 3S-17

[9] D. Mankoff, A. Shields, K. Krohn: PET imaging of cellular proliferation. Radiol Clin North Am **43** (2005) 153-167

[10] P. L. Jager, R. Chirakal, C. J. Marriott, et al.: 6-L-18F-Fluorodihydroxyphenylalanine PET in neuroendocrine tumors: Basic aspects and emerging clinical applications. J Nucl Med **49** (2008) 573-586

[11] S. Milker-Zabel, A. Zabel-du Bois, M. Henze, et al.: Improved target volume definition for fractionated stereotactic radiotherapy in patients with intracranial meningiomas by correlation of CT, MRI, and [68Ga]-DOTATOC-PET. Int J Radiat Oncol Biol Phys **65** (2006) 222-227

[12] B. Shapiro: Ten years of experience with MIBG applications and the potential of new radiolabeled peptides: a personal overview and concluding remarks. Q J Nucl Med **39** (1995) 150-155

[13] L. Belvisi, A. Bernardi, M. Colombo, et al: Targeting integrins: insights into structure and activity of cyclic RGD pentapeptide mimics containing azabicycloalkane amino acids. Bioorg Med Chem **14** (2006) 169-180

[14] A. J. Beer, A. L. Grosu, J. Carlsen, et al.: [18F]Galacto-RGD positron emission tomography for imaging of {alpha}v{beta}3 expression on the neovasculature in patients with squamous cell carcinoma of the head and neck. Clin Cancer Res **13** (2007) 6610-6616

[15] O. Couturier, A. Luxen, J. F. Chatal, et al.: Fluorinated tracers for imaging cancer with positron emission tomography. Eur J Nucl Med Mol Imaging **31** (2004) 1182-1206

[16] F. Blankenberg, P. Katsikis, J. Tait, et al: In vivo detection and imaging of phosphatidylserine expression during programmed cell death. Proc Natl Acad Sci USA **95** (1998) 6349-6354

[17] J. Rajendran, K. Krohn: Imaging hypoxia and angiogenesis in tumors. Radiol Clin North Am **43** (2005) 169-187

[18] D. Thorwarth, M. Alber: Implementation of hypoxia imaging into treatment planning and delivery. Radiother Oncol (2010) *in press*
[19] M. Weinmann, S. Welz, M. Bamberg: Hypoxic radiosensitizers and hypoxic cytotoxins in radiation oncology. Curr Med Chem Anticancer Agents **3** (2003) 364-374
[20] P. Vaupel, L. Harrison: Tumor hypoxia: causative factors, compensatory mechanisms, and cellular response Oncologist **9 Suppl 5** (2004) 4-9
[21] A. Padhani: PET imaging of tumour hypoxia. Cancer Imaging **6** (2006) S117-121
[22] A. Nunn, K. Linder, H. W. Strauss: Nitroimidazoles and imaging hypoxia. Eur J Nucl Med **22** (1995) 265-280
[23] W. J. Koh, K. S. Bergman, J. S. Rasey, et al.: Evaluation of oxygenation status during fractionated radiotherapy in human nonsmall cell lung cancers using [F-18]fluoromisonidazole positron emission tomography. Int J Radiat Oncol Biol Phys **33** (1995) 391-398
[24] J. G. Rajendran, D. C. Wilson, E. U. Conrad, et al.: [(18)F]FMISO and [(18)F]FDG PET imaging in soft tissue sarcomas: correlation of hypoxia, metabolism and VEGF expression. Eur J Nucl Med Mol Imaging **30** (2003) 695-704
[25] R. J. Hicks, G. C. Toner, P. F. Choong: Clinical applications of molecular imaging in sarcoma evaluation Cancer Imaging **5** (2005) 66-72
[26] C. S. Dence, D. E. Ponde, M. J. Welch, J. S. Lewis: Autoradiographic and small-animal PET comparisons between (18)F-FMISO, (18)F-FDG, (18)F-FLT and the hypoxic selective (64)Cu-ATSM in a rodent model of cancer. Nucl Med Biol **35** (2008) 713-720
[27] F. Dehdashti, M. A. Mintun, J. S. Lewis, et al.: In vivo assessment of tumor hypoxia in lung cancer with 60Cu-ATSM. Eur J Nucl Med Mol Imaging **30** (2003) 844-850
[28] P. W. Grigsby, R. S. Malyapa, R. Higashikubo, et al.: Comparison of molecular markers of hypoxia and imaging with (60)Cu-ATSM in cancer of the uterine cervix. Mol Imaging Biol **9** (2007) 278-283
[29] F. Dehdashti, P. W. Grigsby, J. S. Lewis, et al.: Assessing tumor hypoxia in cervical cancer by PET with 60Cu-labeled diacetyl-bis(N4-methylthiosemicarbazone). J Nucl Med **49** (2008) 201-205
[30] F. Dehdashti, P. W. Grigsby, M. A. Mintun, et al.: Assessing tumor hypoxia in cervical cancer by positron emission tomography with 60Cu-ATSM: relationship to therapeutic response-a preliminary report. Int J Radiat Oncol Biol Phys **55** (2003) 1233-1238
[31] W. R. Dolbier, Jr., A. R. Li, C. J. Koch, C. Y. Shiue, A. V. Kachur: [18F]-EF5, a marker for PET detection of hypoxia: synthesis of precursor and a new fluorination procedure. Appl Radiat Isot **54** (2001) 73-80
[32] G. Komar, M. Seppanen, O. Eskola, et al.: 18F-EF5: a new PET tracer for imaging hypoxia in head and neck cancer. J Nucl Med **49** (2008) 1944-1951
[33] S. M. Evans, D. Fraker, S. M. Hahn, et al.: EF5 binding and clinical outcome in human soft tissue sarcomas. Int J Radiat Oncol Biol Phys **64** (2006) 922-927
[34] D. M. Mirshanov. (Tashkent Branch, All-Union Research Surgery Center, USSR Academy of Medical Science, USSR, 1987).
[35] C. H. Kaplan. (International patent application, 1989).
[36] B. H. Hasegawa, E. L. Gingold, S. M. Reilly, S. C. Liew, C. E. Cann: Description of a simultaneous emission-transmission CT system. Proc SPIE **1231** (1990) 50-60
[37] B. H. Hasegawa, K. Iwata, K. H. Wong, et al.: Dual-modality imaging of function and physiology. Acad Radiol **9** (2002) 1305-1321
[38] E. F. Jones, R. G. Gould, H. F. VanBrocklin: Bruce H. Hasegawa, PhD, 1951-2008. J Nucl Med **49** (2008) 37N-38
[39] T. Beyer, D. Townsend, T. Brun, et al.: A combined PET/CT scanner for clinical oncology. J Nucl Med **41** (2000) 1369-1290
[40] D. W. Townsend: Multimodality imaging of structure and function. Phys Med Biol **53** (2008) R1-R39
[41] D. Bailey, P. Roach, E. Bailey, J. Hewlett, R. Keijzers: Development of a cost-effective modular SPECT/CT scanner. Eur J Nuc Med Mol Imaging **34** (2007) 1415-1426
[42] F. Beekman, B. Hutton: Multi-modality imaging on track. Eur J Nuc Med Mol Imaging **34** (2007) 1410-1414
[43] H. C. Steinert, G. K. von Schulthess: Initial clinical experience using a new integrated in-line PET/CT system. Br J Radiol **73** (2002) S36-S38
[44] W. R. Luk, W. D. Digby, W. F. Jones, M. E. Casey: An analysis of correction methods for emission contamination in PET postinjection transmission measurement. IEEE Trans Nucl Sci **42** (1995) 2303-2308
[45] R. E. Coleman, D. Delbeke, M. J. Guiberteau, et al.: Concurrent PET/CT with an integrated imaging system: intersociety dialogue from the joint working group of the American College of Radiology, the Society of Nuclear Medicine, and the Society of Computed Body Tomography and Magnetic Resonance J Nucl Med **46** (2005) 1225-1239

[46] A. Bischof Delaloye, I. Carrio, A. Cuocolo, et al.: White paper of the European Association of Nuclear Medicine (EANM) and the European Society of Radiology (ESR) on multimodality imaging. Eur J Nuc Med Mol Imaging **34** (2007) 1147-1151
[47] L. Stegger, M. Schäfers, M. Weckesser, O. Schober: EANM-ESR white paper on multimodality imaging. Eur J Nuc Med Mol Imaging **35** (2008) 677-680
[48] G. Antoch, L. S. Freudenberg, T. Beyer, A. Bockisch, J. F. Debatin: To enhance or not to enhance? 18F-FDG and CT contrast agents in dual-modality 18F-FDG PET/CT. J Nucl Med **45 Suppl 1** (2004) 56S-65S
[49] O. Mawlawi, J. J. Erasmus, R. F. Munden, et al.: Quantifying the effect of IV contrast media on integrated PET/CT: clinical evaluation. AJR Am J Roentgenol **186** (2006) 308-319
[50] A. Ahmadian, M. R. Ay, J. H. Bidgoli, S. Sarkar, H. Zaidi: Correction of oral contrast artifacts in CT-based attenuation correction of PET images using an automated segmentation algorithm Eur J Nucl Med Mol Imaging **35** (2008) 1812-1823
[51] D. Rickey, R. Gordon, W. Huda: On lifting the inherent limitations of positron emission tomography by using magnetic fields (MagPET). Automedica **14** (1992) 355-369
[52] B. E. Hammer, N. L. Christensen, B. G. Heil: Use of a magnetic field to increase the spatial resolution of positron emission tomography. Med Phys **21** (1994) 1917-1920
[53] A. Wirrwar, H. Vosberg, H. Herzog, et al.: 4.5 tesla magnetic field reduces range of high-energy positrons-potential implications for positron emission tomography. IEEE Trans Nucl Sci **44** (1997) 184-189
[54] R. R. Raylman, B. E. Hammer, N. L. Christensen: Combined MRI-PET scanner: a Monte-Carlo evaluation of the improvements in PET resolution due to the effects of a static homogeneous magnetic field. IEEE Trans Nucl Sci **43** (1996) 2406-2412
[55] N. L. Christensen, B. E. Hammer, B. G. Heil, K. Fetterly: Positron emission tomography within a magnetic field using photomultiplier tubes and light-guides. Phys Med Biol **40** (1995) 691-697
[56] Y. Shao, S. R. Cherry, K. Farahani, K. Meadors: Simultaneous PET and MR imaging. Phys Med Biol **42** (1997) 1965-1970
[57] Y. Shao, S. R. Cherry, K. Farahani, et al.: Development of a PET detector system compatible with MRI/NMR systems. IEEE Trans Nuc Sci **44** (1997) 1167-1171
[58] R. Slates, S. R. Cherry, A. Boutefnouchet, et al.: Design of a small animal MR compatible PET scanner. IEEE Trans Nucl Sci **46** (1999) 565-570
[59] R. Slates, K. Farahani, Y. Shao, et al.: A study of artefacts in simultaneous PET and MR imaging using a prototype MR comptatible PET scanner. Phys Med Biol **44** (1999) 2015-2027
[60] P. K. Marsden, D. Strul, S. F. Keevil, S. C. Williams, D. Cash: Simultaneous PET and NMR. Br J Radiol **75** (2002) S53-59
[61] J. E. Mackewn, D. Strul, W. A. Hallett, et al.: Design and development of an MR-compatible PET scanner for imaging small animals. IEEE Trans Nucl Sci **52** (2005) 1376-1380
[62] S. Yamamoto, S. Takamatsu, H. Murayama, K. Minato: A block detector for a multislice, depth-of-interaction MR-compatible PET. EEE Trans Nucl Sci **52** (2005) 33-37
[63] R. R. Raylman, S. Majewski, S. K. Lemieux, et al.: Simultaneous MRI and PET imaging of a rat brain. Phys Med Biol **51** (2006) 6371-6379
[64] R. R. Raylman, S. Majewski, S. S. Velan, et al.: Simultaneous acquisition of magnetic resonance spectroscopy (MRS) data and positron emission tomography (PET) images with a prototype MR-compatible, small animal PET imager. J Magn Reson **186** (2007) 305-310
[65] A. J. Lucas, R. C. Hawkes, R. E. Ansorge, et al.: Development of a combined microPET-MR system. Technol Cancer Res Treat **5** (2006) 337-341
[66] W. B. Handler, K. M. Gilbert, H. Peng, B. A. Chronik: Simulation of scattering and attenuation of 511 keV photons in a combined PET/field-cycled MRI system. Phys Med Biol **51** (2006) 2479-2491
[67] D. Renker: Properties of avalanche photodiodes for applications in high energy physics, astrophysics and medical imaging. Nucl Instr Meth A **486** (2002) 164-169
[68] D. Renker: Geiger-mode avalanche photodiodes, history, properties and problems Nucl Instr Meth A **567** (2006) 48-56
[69] G. Llosa, R. Battiston, N. Belcari, et al.: Novel silicon photomultipliers for PET applications. IEEE Trans Nucl Sci **55** (2008) 877-881
[70] M. Bergeron, J. Cadorette, J. F. Beaudoin, et al.: Performance evaluation of the LabPET APD-based digital PET scanner. IEEE Trans Nucl Sci **56** (2009) 10-16
[71] R. Lecomte, J. Cadorette, S. Rodrigue, et al.: Initial results from the Sherbrooke avalanche photodiode positron tomograph. IEEE Trans Nucl Sci **43** (1996) 1952-1957
[72] B. J. Pichler, M. S. Judenhofer, C. Catana, et al.: Performance test of an LSO-APD detector in a 7-T MRI scanner for simultaneous PET/MRI. J Nucl Med **47** (2006) 639-647
[73] C. Catana, Y. Wu, M. S. Judenhofer, et al.: Simultaneous acquisition of multislice PET and MR images: Initial results with a MR-compatible PET scanner. J Nucl Med **47** (2006) 1968-1976

[74] C. Catana, D. Procissi, Y. Wu, et al.: Simultaneous in vivo positron emission tomography and magnetic resonance imaging. Proc Natl Acad Sci U S A **105** (2008) 3705-3710
[75] C. Woody, D. Schlyer, P. Vaska, et al.: Preliminary studies of a simultaneous PET/MRI scanner based on the RatCAP small animal tomograph Nucl Instr Meth A **571** (2007) 102-105
[76] M. S. Judenhofer, C. Catana, B. K. Swann, et al.: Simultaneous PET/MR images, acquired with a compact MRI compatible PET detector in a 7 Tesla magnet. Radiology **244** (2007) 807-814
[77] M. S. Judenhofer, H. F. Wehrl, D. F. Newport, et al.: Simultaneous PET-MRI: a new approach for functional and morphological imaging. Nat Med **14** (2008) 459-465
[78] S. Moehrs, A. Del Guerra, D. J. Herbert, M. A. Mandelkern: A detector head design for small-animal PET with silicon photomultipliers (SiPM). Phys Med Biol **51** (2006) 1113-1127
[79] S. J. Hong, I. C. Song, M. Ito, et al.: An investigation into the use of Geiger-Mode solid-state photomultipliers for simultaneous PET and MRI acquisition. IEEE Trans Nucl Sci **55** (2008) 882-888
[80] A. Kolb, E. Lorenz, M. S. Judenhofer, et al.: Evaluation of Geiger-mode APDs for PET block detector designs. Phys Med Biol **55** (2010) 1815-1832
[81] A. Reznik, B. J. Lui, J. A. Rowlands: An amorphous selenium based positron emission mammography camera with avalanche gain. Technol Cancer Res Treat **4** (2005) 61-67
[82] A. Reznik, S. D. Baranovskii, O. Rubel, et al.: Avalanche multiplication in amorphous selenium and its utilization in imaging. Journal of Non-Crystalline Solids **354** (2008) 2691-2696
[83] A. W. Sauter, H. F. Wehrl, A. Kolb, M. S. Judenhofer, B. J. Pichler: Combined PET/MRI: one step further in multimodality imaging. Trends Mol Med **16** (2010) 508-515
[84] H. P. Schlemmer, B. J. Pichler, M. Schmand, et al.: Simultaneous MR/PET imaging of the human brain: feasibility study. Radiology **248** (2008) 1028-1035
[85] S. J. Holdsworth, R. Bammer: Magnetic resonance imaging techniques: fMRI, DWI, and PWI. Semin Neurol **28** (2008) 395-406
[86] J. Gaa, E. J. Rummeny, M. D. Seemann: Whole-body imaging with PET/MRI. Eur J Med Res **30** (2004) 309-312
[87] M. D. Seemann: Whole-body PET/MRI: the future in oncological imaging. Technol Cancer Res Treat **4** (2005) 577-582
[88] H. P. Schlemmer, B. J. Pichler, R. Krieg, W. D. Heiss: An integrated MR/PET system: prospective applications. Abdom Imaging **34** (2009) 668-674
[89] R. J. Hicks, E. W. Lau: PET/MRI: a different spin from under the rim. Eur J Nucl Med Mol Imaging **36** (2009) 10-14
[90] G. S. Payne, M. O. Leach: Applications of magnetic resonance spectroscopy in radiotherapy treatment planning. Br J Radiol **79 Spec No 1** (2006) S16-26
[91] G. Delso, S. Ziegler: PET/MRI system design. Eur J Nuc Med Mol Imaging **36** (2009) 86-92
[92] D. Gagnon, M. Morich, D. Blakely, K. Nieman, P. Healthcare, Ed. (USA, 2008).
[93] M. Abdoli, M. Ay, A. Ahmadian, R. Dierckx, H. Zaidi: Reduction of dental filling metallic artefacts in CT-based attenuation correction of PET data using weighted virtual sinograms optimized by a genetic algorithm. Med Phys (2010) *in press*
[94] H. Zaidi: Navigating beyond the 6th dimension: a challenge in the era of multi-parametric molecular imaging. Eur J Nucl Med Mol Imaging **36** (2009) 1025-1028
[95] A. Rahmim, H. Zaidi: PET versus SPECT: strengths, limitations and challenges. Nucl Med Commun **29** (2008) 193-207
[96] A. Alavi, S. Basu: Planar and SPECT imaging in the era of PET and PET–CT: can it survive the test of time? Eur J Nucl Med Mol Imaging **35** (2008) 1554-1559
[97] G. Mariani, L. Bruselli, A. Duatti: Is PET always an advantage versus planar and SPECT imaging? Eur J Nucl Med Mol Imaging **35** (2008) 1560-1565
[98] A. Seret: Will high-resolution/high-sensitivity SPECT ensure that PET is not the only survivor in nuclear medicine during the next decade? Eur J Nucl Med Mol Imaging **36** (2009) 533-535

Skin overdosage using Small Field Electron Applicators

P.Egli[1], G.Lutters[1]
Institut für Radio-Onkologie, Kantonsspital Aarau AG
mail: peter.egli@ksa.ch

Introduction

Electrons with the characteristic steep depth dose curves are used to treat tumors in superficial regions. The Siemens standard electron applicator set contains different applicators with field sizes from 5 cm round up to 25 cm by 25 cm square (i.e. EA205, EA210, EA215, EA220, EA225 from Siemens Medical Systems). In order to treat conformal small target volumes in the order of 2-4 cm diameter you have to use self made inserts to block normal tissue (Fig.1 left) or alternatively the small field applicators (Siemens Medical Systems) (Fig.1 right).

Material and Methods

The small field applicator set contains 4 round cones with diameters of 2, 3, 4 and 5 cm with an acrylic extension and 3 round cones with diameters of 6, 7 and 8 cm full metal. For light-irradiation field testing, we irradiated a Gafchromic film (RTQA2, Advanced Materials, USA) with 200 monitor units of 12 MeV electrons. Realizing the ring had a higher dose we measured depth ionization curves, inplane and crossplane profiles in different depths with a source-surface-distance of 100 cm for different electron energies from 6 to 21 MeV using a water phantom (MP3, PTW Freiburg, Germany), the Mephysto mcc software (v1.7.2, PTW Freiburg, Germany) and a semiflex chamber (type 31002, 0.125 ccm, PTW Freiburg, Germany). To avoid collision between the semiflex chamber and the small field applicator touching the water surface we could not measure profiles closer than 5 mm to the water surface. For comparison we also used the electron applicator EA205 (5 cm round) with a self made insert with diameter 4 cm round (Fig.1 left). The measurements were done at Mevatron Primus and Oncor Avant Gard linear accelerator (both Siemens Medical Systems).

Results

The shape of the 15 MeV electron depth ionisation curves for the applicator EA205 with insert 4 round and the small field applicator 4 round differ in the first 5 cm. The inplane and crossplane profiles for depths bigger than 30 mm have similar shapes (Fig.2+3). The profiles at a depth of 5 and 15 mm have different shapes. The profile at 5 mm depth for the applicator EA205 with insert has 94.5% of the maximum dose at 14 mm from the central axis and 86.9% at 16 mm. The profile for the small field applicator has 104% of the maximum dose on the central axis at 14 mm from the central axis and 105% at 16 mm.

Discussion

The small field electron applicators are easy to place on superficial tumors, as the cones are in contact with the skin/surface. But as seen in Fig.3 they can give a higher dose to the skin depending on the electron energy and the small field applicator size. This effect is increasing with higher electron energies and different small field applicators resulting in a 20% overdose at the horns for 21 MeV in depth of 5 mm. This can lead to unwanted skin reactions. In order to avoid skin reactions and improve the dose coverage in volumes near the surface, you can use a combination of both electron applicators.

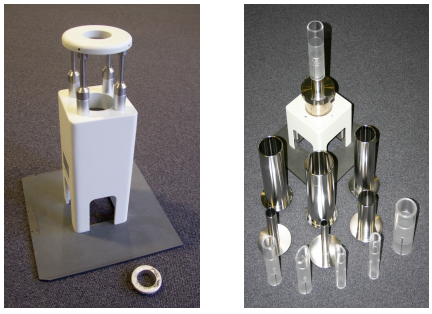

Fig.1: left: Siemens EA205 electron applicator with a selfmade lead insert with a diameter of 4 cm; right: Siemens Small Field electron applicators with different inserts and additional acrylic extensions

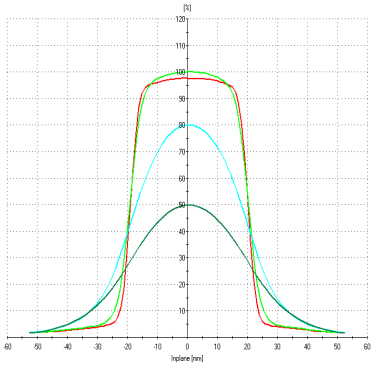

Fig.2: Inplane profiles of a 15 MeV electron beam collimated with the EA205 applicator with selfmade lead insert of diameter 4 cm measured in a water phantom in depth of 5.0, 16.0, 41.0 and 54.0 mm with a PTW semiflex chamber.

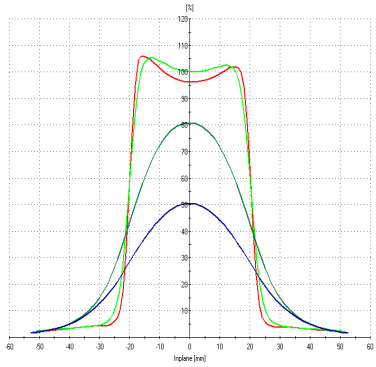

Fig.3: Inplane profiles of a 15 MeV electron beam collimated with a small field applicator with diameter 4 cm with acrylic extension measured in a water phantom in depth of 5.0, 16.0, 41.0 and 54.0 mm with a PTW semiflex chamber.

Parameter study for the characterization of the scatter radiation for a micro CT using Monte Carlo methods

S. Peter[1], M.K. Fix[1], W. Volken[1], M.A. Zulliger[2], P. Manser[1]
[1] Division of Medical Radiation Physics, Inselspital - University of Berne
[2] SCANCO Medical AG, Brüttisellen
mail: werner.volken@vsw.ch

Introduction

Micro cone beam computed tomography (CBCT) has a wide area of applications, for instance in medicine and material science. However, quantitative analysis of micro CBCT images can be problematic due to scatter radiation. To perform a scatter correction it is desirable to have detailed knowledge of the scatter radiation. Since the scatter radiation cannot be measured directly a convenient way of its investigation is to perform Monte Carlo (MC) simulations.

Material and Methods

The micro CBCT system used for this study was the XtremeCT from SCANCO Medical AG, which is designed for imaging and quantitative measurement of the bone structure and density in the human distal radius and tibia. The MC model of the micro CBCT was implemented using EGS++ [1]. The implemented source for modelling the output of the x-ray tube was validated by comparing transmission measurements with simulations for different filters and absorbers. Additionally, several phantoms were implemented and validated by comparing simulated transmission profiles to the corresponding measurements. The validated MC model was used to perform a parameter study of the scatter radiation for different phantoms. The simulated scatter signal in the detector was divided into several components according to the region the scatter occurred in, as well as the scattering process the particle underwent before reaching the detector. The scatter signal was further split into a portion coming from particles scattered once and a portion coming from multiple scattered particles. The Scatter to Primary Ratio (SPR) was determined to quantify the amount of scatter. The impact of density, composition and volume changes on the characteristics of the scatter radiation in the detector was investigated by simulating cylindrical phantoms of different compositions, densities and radii. In addition, a tibia phantom was simulated in order to obtain a realistic conception of the scatter radiation in human applications.

Results

The validation of the source showed that all simulated transmission profile values agree within 3% with the measurements for all filters and within 8% in case when no filter is present. For all phantoms 97% of the simulated transmission profile values agree within 3% with the measurements. The scatter analysis showed that the main contributions to the scatter signal come from scatter in the phantom and in the filter which can be seen in figure 1.
The relative amount of the total signal coming from scatter in the filter is below 0.5% for all simulated phantoms. The total signal and the scatter signal, especially the phantom scatter, show a strong dependence on the phantom size. Furthermore, it was shown that the signals depend stronger on the composition of the material than on the density. The relative amount of scatter signal coming from multiple scattered particles depends foremost on the size of the phantom. It was also shown that the main scatter processes are Rayleigh and Compton scattering, most of the scatter radiation originates from Rayleigh scattering which can be seen in figure 2, the relative amount of signal coming from Compton scattering increases with the phantom size. The scatter analysis showed a SPR of up to 15% for the tibia phantom.

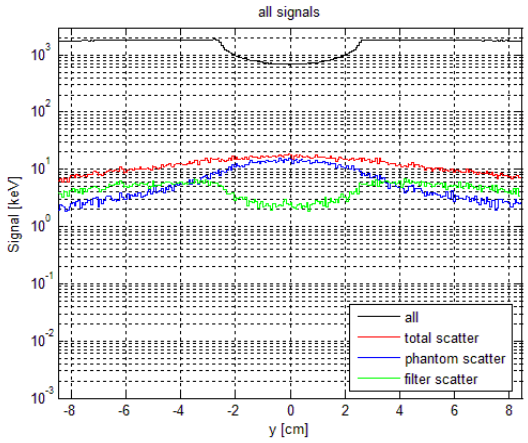

Figure 1: Total signal, total scatter signal, phantom scatter signal and filter scatter signal for a water cylinder with radius 2 cm.

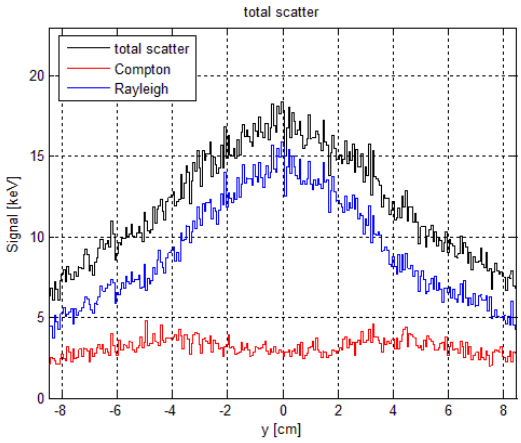

Figure 2: Total scatter signal split up into signal coming from Compton scattering and signal coming from Rayleigh scattering for a water cylinder with radius 2 cm.

Discussion

The validation showed that the implemented MC model is accurate enough for a reliable scatter analysis. It was shown that the scatter radiation depends on the shape and properties of the phantom. The results of this parameter study can now be used to develop a MC based scatter correction algorithm for the XtremeCT. This work was supported by CTI grant 10629.1.

References

[1] Kawrakow, I; Mainegra-Hing, E; Tessier, F; Walters, B.R.B.: The EGSnrc C++ class library, NRC Report PIRS-898 (revA), Ottawa, Canada, 2009